

# High Energy Engineering X-ray Scattering (HEX) Facility

## CONTENTS

	Acronyms .....	3
	Abstract .....	4
	Introduction .....	6
1	Benefits to New York State .....	8
2	Scientific Programs and Technical Scope .....	11
	2.1 Advanced Energy Storage .....	12
	2.2 Engineering and Grid Materials .....	16
	2.3 Development and Advisory Team.....	19
	2.4 Scope of HEX Project .....	20
	2.5 What's Next.....	20
3	HEX beamline .....	22
	3.1 Super-conducting Wiggler Source .....	24
	3.2 Front End .....	33
	3.3 White Beam Management .....	38
	3.4 Radiation Shielding .....	44
4.	Optics .....	48
	4.1 Center Branch Imaging Monochromator.....	50
	4.2 Center Branch Focusing Monochromator (Mature Scope) .....	60
	4.3 Side Branch Monochromator (Out of Base Scope) .....	71
5.	Experimental systems .....	73
	5.1 Experimental Station E Center Branch (Not In Scope).....	73
	5.2 Experimental Station F in Satellite Building (In Scope) .....	73
	5.3 Multi-detector EDXD system (not in scope).....	92
	5.4 White Beam Branch (Not in Scope) .....	97
	5.5 Experimental Station B side Branch (Not in Scope) .....	97

5.6 Beamline Utilities..... 98

5.7 Equipment Protection System..... 101

5.8 Personnel Protection System..... 102

6 Major Technical Risk Items ..... 104

7. Safety ..... 106

8. References..... 107

9. Reference Documents ..... 109

## Acronyms

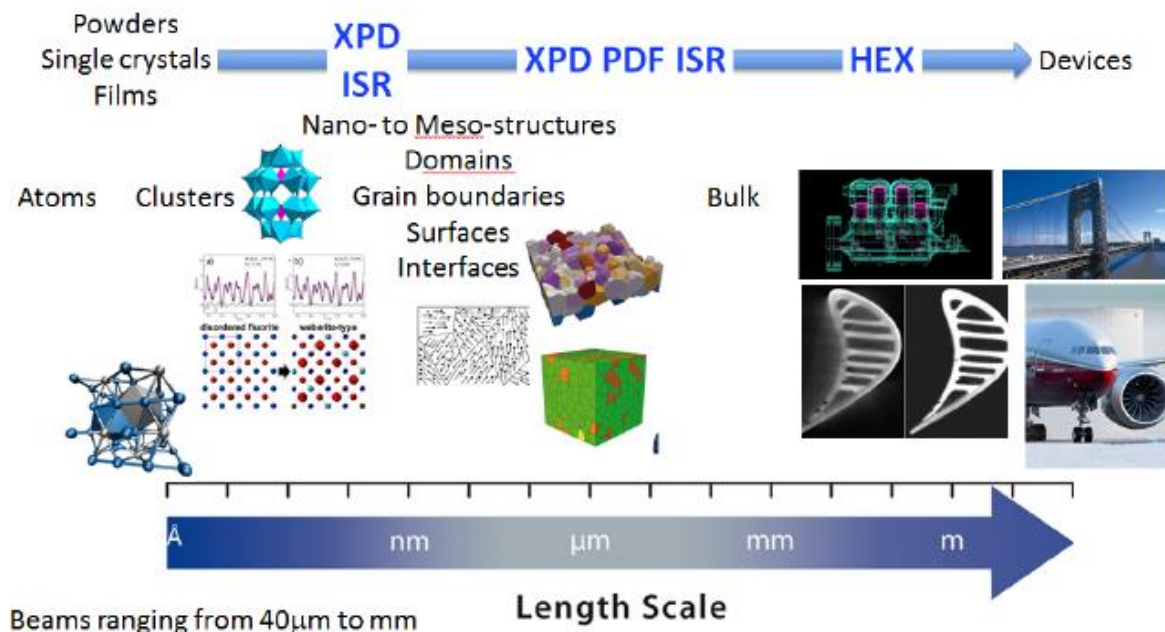
ADX	Angle-Dispersive X-ray Diffraction
BDP	Beamline Development Proposal
DCM	Double-Crystal Monochromator
DLM	Double-Crystal Laue Monochromator
DW	Damping Wiggler
EDX	Energy-Dispersive X-ray Diffraction
FE	Front End
FMK	Fixed Mask
FOE	First Optical Enclosure
FXI	Full-Field X-ray Imaging
HXN	Hard X-ray Nanoprobe
ISS	Inner Shell Spectroscopy
NEXAFS	Near Edge X-ray Absorption Fine Structure
SCW	Super-conducting Wiggler
XANES	X-ray Absorption Near Edge Structure
XPD	X-ray Powder Diffraction

## Abstract

Partnering with NY State, Brookhaven Laboratory will construct an experimental facility, the HEX beamline, at the NSLS-II synchrotron, providing intense high-energy x-rays produced by a superconducting wiggler source to advance energy storage technologies. Using state-of-art imaging and diffraction probes, researchers will be able to map the three-dimensional structure of energy storage materials in real time and under actual operating conditions. This unique NY State capability will advance battery development globally. Benefits will include a greater ability to integrate renewable energy into the grid, reductions in carbon emissions, and more efficient storage and use of energy—key elements to NY State becoming a national center for battery and grid science and technology.

The HEX beamline will be a new beamline facility to provide a suite of most advanced hard X-ray tools required for engineering-scale materials studies using hard X-ray diffraction, scattering, and imaging. The beamline will be located on a short-beta straight section using a superconducting wiggler as the high-energy high-flux X-ray source. It will consist of three independent endstations in a satellite building to provide hard X-ray diffraction and imaging probes in the 20-200 keV range for studies of engineering material systems under real operating conditions. Key science areas will be in the areas of structural analysis of the chemical reaction fronts and their evolution in real battery systems during charge and discharge cycles, materials microstructural changes under external extreme conditions such as high mechanical stress, high pressure, high temperatures, and corrosive environment, and phase contrast hard X-ray imaging with a large field of view in real space for studies of micro-crack formation and propagations under realistic operating loads, etc. These studies will have significant impact on the economic competitiveness of industries in New York state as well as in the nation.

HEX is part of the NSLS-II '*Diffraction and In-Situ Scattering*' program that focuses on the structural characterization and modeling of materials ranging from single crystals to powders to thin films. Often real or functional materials contain defects, surfaces, interfaces, and have particular morphologies and heterogeneities on different length-scales. The program offers a comprehensive suite of elastic scattering and diffraction techniques, tailored to studies of such complex or heterogeneous samples preferably under in situ and operando conditions, for advancing our understanding of the underlying material dependence of functional properties. The program also explores the combination of diffraction/scattering with imaging techniques (e.g., diffraction-tomography analysis of the bulk, coherent beam imaging of surfaces, phase-contrast full-field imaging). The objective is to examine the structure-function relationships that occur at different spatial and temporal scales, from Å to meters and from seconds to months.



HEX will meet the standards and high operating performance of other x-ray machines in the country and worldwide and the end station capabilities will be tailored for attacking and solving of fundamental/technological problems. When fully built out, HEX will consist of three independently operating branches, side branch, center branch (with a tandem pair of endstations), and white-beam branch. Both the center branch and white-beam branch are designed to be white-beam compatible. The initial scope, funded by NYSERDA will comprise the central branch only; the design will, however, allow addition (mature scope) of the side and white beam branches when additional funding becomes available. Consistent with worldwide equivalent facilities, HEX will integrate multiple high energy x-ray techniques: energy dispersive x-ray diffraction (EDXD); monochromatic angle dispersive x-ray diffraction (ADX), both wide (XRD) and small angle (SAXS); pair distribution function measurements (PDF); phase-contrast imaging, and computed tomography(CT)/radiography.

This preliminary design report (PDR) describes the following topics: Summary of the scientific case; Design of the beamline in terms of the source (super-conducting wiggler and Front End); Analysis of radiation shielding, in particular for the satellite building, including that of Bremsstrahlung, secondary Bremsstrahlung, and synchrotron x-rays; Optical design (three branches with two being white-beam compatible); Discussion of end stations for EDXD, ADXD and imaging; Thermal analysis and thermal management of the white-beam components; and Analysis of technical and schedule risks.

## Introduction

Industrial battery research requires real time studies under real conditions. Intermediate phases and non-stable phases are difficult to freeze. Thus, *operando* and/or *in-situ* structural measurements are desirable for battery research. High-energy x-rays provided by HEX, being able to penetrate about 100 mm of battery material, are the ideal probe.

HEX will consist of three independently-operating branches: (i) side branch, (ii) center branch consisting of two experimental enclosures, and (iii) white-beam branch. The center and white-beam branches are white-beam compatible. Consistent with worldwide equivalent facilities, HEX will integrate multiple high energy x-ray techniques: energy dispersive x-ray diffraction (EDXD); monochromatic angle dispersive x-ray diffraction (ADX), both wide (XRD) and small angle (SAXS); pair distribution function measurements (PDF); phase-contrast imaging, and computed tomography(CT)/radiography.

The center branch (initial scope) provides high x-ray energies up to 150 keV for phase contrast x-ray imaging in planar and CT modes. The resolution of about 1 microns combined with a field of view of 100 mm is suitable for most industrial batteries. Phase contrast techniques, such as Diffraction Enhanced Imaging, provide a new way for studying batteries and their micro-structure using the x-ray extinction contrast phenomenon. The center branch provides energy-dispersive x-ray diffraction (EDXD) at high x-ray energies up to 200 keV. Spatial resolution for EDXD is 5 microns in the transverse direction and 50 microns in the longitudinal direction. Data acquisition time is about 1 minute per line scan using a novel scattering geometry and an array detector.

The fixed-energy side branch (mature scope) offers x-rays above 75 keV for x-ray diffraction and pair distribution function measurements.

The white-beam branch (mature scope) provides dedicated EDXD at high x-ray energies up to 200 keV.

The techniques and specifications for the HEX endstations, both in the initial scope and mature scope, are summarized below. Red-colored branches and techniques are not in the current scope.

	Side branch	Center branch	White-beam branch
Technique	ADX, PDF	EDXD, ADX, imaging, small angle scattering, CT	EDXD
Beam size	0.5 mm x 0.5 mm	0.5 mm x 0.5 mm for diffraction 20 mm x 100 mm for imaging	5 mm x 5 mm
Flux/flux density (at 50 keV)	$10^{12}$ ph/s for focused beam	$10^{11}$ ph/s/mm <sup>2</sup> for imaging beam	$10^{15}$ /ph/s/0.1%bw/m rad <sup>2</sup> for white beam

		<b><math>10^{15}</math>/ph/s/0.1%bw/mrad<sup>2</sup> for white beam</b> <b><math>10^{10}</math> ph/s for focused beam</b>	
Resolution	0.5 mm	<b>10 microns for EDXD 0.5 mm for ADXD</b> <b>10 microns for ADXD with focused beam</b> <b>1 micron for imaging</b>	10 microns
Energy range (keV)	40-120	<b>20-200 keV for white beam</b> <b>30 – 150 keV for imaging beam</b> <b>30 – 150 keV for focused beam</b>	20 – 200 keV white beam
Mode	Monochromatic	<b>White/Monochromatic</b>	White

## 1 Benefits to New York State

Before closing in late 2014, Brookhaven Laboratory’s National Synchrotron Light Source (NSLS) served as a key resource for industry for more than three decades, including companies such as General Electric, who built a \$170 million battery factory in upstate New York (NY) based on research conducted at the NSLS X17 beamline [1]. The National Synchrotron Light Source II (NSLS-II) is a new facility of global importance, and its advanced capabilities will take these kinds of industry partnerships to the next level, enabling researchers to study materials and processes in ways not possible before now.

### *Catalyzing major energy technologies*

NSLS-II and this new beamline are expected to serve as a key catalyst for energy storage industry growth in NY State. The scientific program at NSLS-II builds on the legacy of its predecessor – the National Synchrotron Light Source (NSLS) – where work led to real-world impact, including industry partnerships that led to commercialization. Researchers at General Electric (GE) used the original NSLS to understand the internal chemical reactions and associated changes to materials an operating commercial battery undergoes during real-time charging and discharging. GE engineers then fine-tuned battery design. GE put the improved performance “Durathon” battery into commercial production for transportation and grid-storage applications at a newly constructed \$170 million production factory in Schenectady, NY, creating hundreds of jobs. GE remains committed to its research partnership with BNL and will help develop the characteristics HEX needs to make the greatest impact. About HEX, Glen Merfeld, energy storage leader at the GE Global Research, said: *“Researchers at GE Global Research look forward to utilizing the new capabilities at the high energy beam line at Brookhaven. This facility at the new NSLS-II synchrotron will help GE understand advanced materials such as metal alloys, ceramic composites, and battery cathodes with unprecedented resolution”*.

### *Attracting energy startups*

This beamline will be a focal point in the state’s energy storage innovation environment. It will combine NY State’s strong support ecosystem for entrepreneurs and startups with the HEX beamline’s easy-access features, fostering an attractive environment to launch and grow new companies on Long Island and across the state. New technology companies will be able to access this world-class facility to conduct both proprietary and non-proprietary research.

### *Supporting the full product development cycle*

The HEX beamline will enable NY State companies to test battery materials and individual components in real time as they operate, accelerating the path to commercialization. These



components then may be integrated into large-scale battery and grid applications at BNL's Northeast Solar Energy Research Center (NSERC). NSERC will offer access to a one-megawatt solar photovoltaic array, together with access to the Brookhaven Laboratory "microgrid" as a product test facility—a unique capability in the U.S. Finally, companies will have future access to the Laboratory's planned incubator space near these testing and development facilities.

### ***Leveraging federal investment for local industry***

The NY State funding will leverage the U.S. Department of Energy's (DOE) billion-dollar investment in the design and construction of NSLS-II along with its expected annual operating budget, when fully operating, of more than \$120M.

### ***Leveraging world-class scientific and engineering talent***

Through NSLS-II, NY State companies will have access to people with experience to help solve their toughest problems. NSLS-II will attract the foremost experts globally in energy technology research. NSLS-II will employ 500 staff and host 4,000 researchers on Long Island each year. Through the Laboratory's partnership with Stony Brook University, companies can access energy scientists across the entire New York region, including those affiliated with the New York Battery and Energy Storage Technology (NY-BEST) consortium and the New York State Smart Grid Consortium. Finally, Brookhaven Science Associates, the company that manages and operates Brookhaven Laboratory for DOE, will continue to invest as much as \$23M annually in local STEM education, expanding the local scientific and engineering workforce available to NY State companies.

### ***Science Goals***

NSLS-II is the newest facility at Brookhaven National Laboratory – a half-mile electron storage ring designed to deliver the brightest synchrotron x-rays in the world – and an important tool poised to enable scientists from industry and academia to solve fundamental and technological problems in engineering materials and to tackle the grand energy challenges facing our nation.

This cutting-edge facility achieved "first light" in October 2014, delivering x-rays to its first beamline. When fully built out, NSLS-II will be able to host thousands of scientific users each year from academia and industry, who will make breakthroughs in critical scientific areas such as energy security, environment, and human health.

NSLS-II enables the study of material properties and functions with nanoscale resolution and provides world-leading capabilities for x-ray imaging and high-resolution energy analysis. The facility will fuel major advances in materials that will enable new energy technologies – such as nanocatalyst-based fuel cells; the widespread, economical use of solar energy; the use of high temperature superconductors in a high-capacity and high-reliability electric grid; advanced electrical storage systems for transportation and harnessing intermittent renewable energy

sources; and the development of the next generation of nuclear power systems.

The High-Energy X-ray Diffraction (HEX) Beamline for Materials Engineering and Battery Research will be one beamline in the next phase to be developed at NSLS-II. The spatial resolution at the HEX beamline will allow scientists to map the structure of materials and understand material dynamics like never before, providing data that will lead to better batteries and new materials for grid-scale energy storage with impact in both the battery and grid markets.

### ***Expected use of state funds***

The \$25M state in state support will be used to design, specify, construct, and install the necessary equipment for a fully functional beamline, consisting of the center branch, dedicated to using high energy x-rays to understand energy-related materials and devices. This beamline is a direct connection between the multi-billion dollar investment at NSLS-II by DOE and the energy and utility industry in NY State.

In order to achieve world-class performance comparable to that available at the JEEP beamline in Diamond Light Source, at the BMIT beamline in Canadian Light Source, and at the imaging beamline in Australian Light Source, that is required to understand the chemistry of batteries, several unique machines and detectors must be designed and constructed. Those devices will be the core of a system for moving samples into and out of the experimental chamber and for gathering and analyzing the very large amounts of data resulting from each experiment. Brookhaven Lab scientists, supported by the NY State funding, will provide this innovative design and oversee construction and implementation.

Key equipment deliverables on the timeline are:

- the Superconducting Wiggler (SCW) to provide a bright source of high-energy x-rays,
- all enclosures (hutches) to accommodate the photon delivery systems and experimental systems, including sample environments with large format, and
- specialized sample chambers with controls and infrastructure.

## 2 SCIENTIFIC PROGRAMS AND TECHNICAL SCOPE

The HEX engineering materials beamline will be a state-of-the-art facility that will not only push the boundaries of fundamental science but also enable studies on materials and systems of industrial/societal relevance. In its mature configuration, the beamline's multitude of capabilities will enable strong university/industry/national-lab collaborations. The HEX beamline will be a central component to increasing the industrial relevance of synchrotron science. A leitmotif of the beamline will be to enable experiments to be performed on real materials/systems designed for applications, under real in-situ operating conditions, in real time. Deep-penetrating, high-energy X-rays will be used in high spatial resolution work enabling one to achieve 4D (3D space + time-temperature-voltage-applied stress, etc.) phase, strain, and morphology mapping capabilities in the study of materials research challenges that are central to this nation's technological future. The goal of the proposed beamline is to establish a sorely needed facility contributing to the US's competitiveness in materials research and in industrial applications (see [1]).

The concept of high energy synchrotron beamlines to provide unique insight into problems of technological interest has already been embraced by a number of other technology-dependent countries. Examples include the JEEP ID12-beamline at the UK Diamond synchrotron [2,3]; Beamlines ID15A (material engineering) & 15B (High pressure diffraction) at the EU's ESRF [4,5]; and engineering beamlines at Germany's HASYLAB synchrotron facilities [6,7]. In the US, Sector 1 at APS (with its planned upgrade as part of the APS-U upgrade) provides a superior high energy undulator-based set of materials science/engineering beamlines [8-10].

The proposed HEX wiggler beamline is intended to substantially surpass the operating parameters of the NSLSX17-B1 wiggler beamline and to greatly enhance the end station capabilities for attacking and solving fundamental/technological problems. Consistent with world-class beamline facilities, the HEX beamline will integrate multiple high energy techniques:

1. Energy dispersive x-ray diffraction (EDXD);
2. Wide- and small-angle monochromatic angle dispersive diffraction;
3. Pair distribution function measurements;
4. Tomography/radiography.

The benefits to be realized from integration of these core techniques were underscored at the HEX Beamline Development Proposal (BDP) Workshop by the experience of state of the art European and APS facilities [11,12]. The European facilities include the highly flexible wiggler-based white beam EDXD method [6] [2,4]. Currently, there is no similar\_dedicated wiggler engineering beamline in the US. Without such a beamline, the competitiveness of the US in high energy x-ray materials research is in jeopardy.

The problems facing advanced technology are diverse and continually evolving. The beamline

science justification presented here will be dual faceted. The first facet involves a set of fundamental science/engineering programs, some of which initiated at the NSLS X17B1 beamline, and which concretely illustrate the science which would be greatly expanded and enhanced at the NSLS-II HEX beamline. We will build on the experience gleaned in high energy x-ray research over the past decade, at NSLS and elsewhere, to create the enhanced experimental capabilities needed for materials research in the future. The second facet emphasizes a newly evolving way of doing mechanics/materials science in which powerful high-energy x-ray measurements, from the single grain up to the macroscopic (grain averaged) length scales, are interfaced with concomitantly emerging powerful computer modeling capabilities over the same wide length scales [13].

HEX is being designed to address two major focus areas, while the toolset of HEX is applicable to many other science research areas:

- 1) Advanced Energy Storage
- 2) Engineering and Grid Materials

These cases demonstrate the types of research that will be uniquely served by the HEX beamline. They illustrate how this proposed beamline will establish structure-function relationships in advanced materials, often at the nanoscale, to accelerate the development of new materials into devices and systems with advanced functionality for promoting innovation and enhancing US industrial competitiveness.

More discussions on the science case were presented by the HEX user community at the Beamline Development Proposal (BDP) meetings in 2012 and 2013, and at the HEX kick-off meeting in early 2015. These are linked in the Reference Documents at the back of this report.

## 2.1 Advanced Energy Storage

The growing need for alternative energy sources and greater energy efficiency, combined with our increasingly untethered lifestyles, have made development of improved battery systems crucial to the future of the nation. These batteries span applications from large scale energy storage for electricity grid applications to hybrid/electric vehicle applications and portable electronic devices. Despite tremendous technical progress over decades of research and development in battery technologies, too little is known about the evolution of the internal microstructure and detailed phase changes taking place during electrochemical cycling. These limitations result from the experimental inaccessibility, during cycling, of the batteries' active components. Ex-situ (or post-mortem) measurements performed on recovered battery components can lead to sample alteration and provide only a small window into extremely complex/dynamic processes.

The pressing need to study the internal processes of batteries in their full-sized commercial embodiments and under their real operating conditions has been identified in the DOE BES report on Basic Research Needs for Electrical Energy Storage [14]. Specifically, this report called for the development of "in situ analytical tools" capable of characterizing the structural changes and electrochemistry inside full-sized batteries with high spatial and temporal

resolution. In-situ characterization of the cathode, separator, electrolyte, and anode materials as a function of time, state of charge, stress, temperature, etc. would therefore constitute a breakthrough for battery development.

Precisely such a breakthrough capability has been developed at NSLS beamline X17B1 and involves in-situ, EDXD measurements that have detailed the chemical changes as a function of space and time (charge state) in the cathodes of three grossly different battery systems. The first system is GE's massive sodium-metal-halide battery technology intended for heavy-duty transportation and stationary power quality applications (see [15,16]). The second system involves ground-breaking visualization of the formation of silver matrix within the  $\text{Ag}_2\text{VP}_2\text{O}_8$  electrode [17]. The third system involves characterizing a less than 100  $\mu\text{m}$  thick  $\text{Li}_x\text{FePO}_4$  cathode in a coin cell [18]. Given these examples, this technique appears capable of extending the benefits of such in-situ studies to essentially the full panoply of prototype and production cells of all battery technologies.

### **GE sodium-metal-halide battery technology**

It is important to note that this collaborative effort between GE, NSLS, and Rutgers U. produced fundamental research results leading to actual factory construction and commercialization of GE's "Durathon™" battery system (see [1]). In this sense, the scientific results and economic fruits of this collaborative effort constitutes a paradigm for the future operation of the HEX beamline program. For details of scientific results the reader is referred to [15,16] and for the economic benefits (e.g. a new NY factory) one can refer to the "DOE Stories of Discovery & Innovation" release [1]. Only a brief illustration of the science illustration is included below.

The GE technology is based on the reaction  $\text{NaCl} + \text{M} \leftrightarrow \text{MCl}_2 + \text{M} + \text{Na}$  (with  $\text{M} = \text{Ni/Fe}$  alloy). The  $3.5 \times 3.5 \times 20 \text{ cm}^3$  cell consists of a central positive electrode comprising M-powder, NaCl, and  $\text{NaAlCl}_4$  that is separated from a liquid Na negative electrode by a ceramic  $\beta''$ -alumina solid electrolyte tube [16]. It operates at 300°C, where the Na and  $\text{NaAlCl}_4$  are molten. The large cell size and complex electrochemistry of this battery technology provide an excellent proving ground to establish both the penetrating power and detailed electrochemical structural insights possible with EDXD (see [16]).

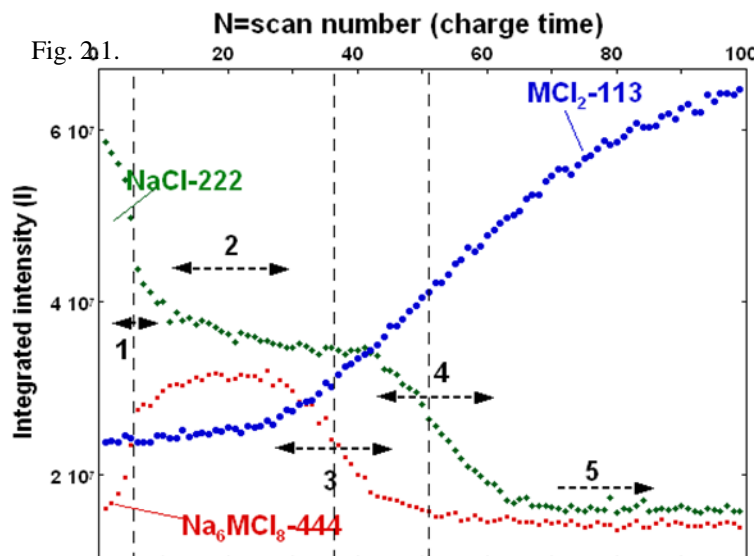


**Figure 2.1** The charging time (diffraction scan number) variation of the integrated spectral intensities for Bragg lines (see indices in figure) chosen to reflect the relative phase abundances of the NaCl,  $\text{MCl}_2$ , and  $\text{Na}_6\text{MCl}_8$  phases. The vertical lines and regions 1-5 identify regions of the electrochemical kinetics discussed in reference [16].

To probe the phase evolution, the gauge volume was positioned in the cathode just inside the  $\beta''$ -alumina separator and a sequence of 99 diffraction spectra, each collected for 70 sec., were then taken as the cell was charged at constant current. In Figure 1, the integrated intensities of selected Bragg peaks associated with phases involved in the cell charge cycle are displayed versus the charging time (pattern number). One should note the transient, intermediate,  $\text{Na}_6\text{MCl}_8$  phase formation from the NaCl phase, and its disappearance, before the conversion to the  $\text{MCl}_2$  phase proceeds. This Bragg intensity data allowed differentiation, with respect to time, thereby yielding reaction rate curves between these different phases [16]. Note that deep within a massive production prototype battery the EDXD technique is able to chronicle the detailed local electrochemistry involved in the temporal passage of the chemical reaction front. The appearance and disappearance of the intermediate  $\text{Na}_6\text{MCl}_8$  phase highlight both the complexity of the electrochemistry involved and the power of the characterization method.

See [16] for the combined spatial and temporal profiling of these cells. Before moving on it is worth emphasizing that the x-ray path length for these in situ experiments was ~50 mm of mostly Fe/Ni alloy, confined in a steel jacket, and inside of a furnace. The white beam of the highly penetrating, high-energy x-rays, such as available at the HEX beamline, is absolutely essential for such work. This work demonstrates that in-situ high energy x-ray diffraction characterization, in space and time, of advanced battery cells under realistic cycling conditions is a reality. The HEX facility could contribute greatly to the advancement of battery technology by enabling the study of the fundamental mechanisms at work inside commercially relevant cells of almost any battery type.

Computed tomography (CT) scanning is not a new technique and has been used frequently for failure analysis in the industry. Synchrotron-based X-ray microtomography is advantageous because the high brightness and flux of the source allow collection of images with high resolution and good signal to noise in a much shorter amount of time.

Many modes of battery failure occur on the micrometer scale. However, most battery materials are air sensitive making sample preparation for analysis by electron microscopy and traditional optical microscopy difficult. Synchrotron hard X-ray microtomography allows one to visualize the interior of a battery without disassembly. Furthermore, the technique produces a three-dimensional (3D) reconstruction of the assembled cell making it easy to find locations of failure. At HEX, with hutch F providing both EDXD and imaging capability, one can find the location of failure by imaging, and then proceed to perform detailed diffraction at the failure location. Finding robust techniques that enable researchers to develop the scientific understanding required to accurately predict the lifetime of a battery is critical for the design of next-generation battery technologies.

A recent study of the growth of lithium metal dendrites through solid polymer electrolyte membranes demonstrates that the synchrotron source provides sufficient flux to achieve good contrast between lithium metal and solid polymer electrolyte membranes enabling one to image lithium metal dendrites [17]. The study uses a high modulus, block copolymer electrolyte membrane. These high modulus membranes suppress lithium dendrite growth, lengthening the lifetime of batteries. However, dendrites still eventually puncture the membrane causing the battery to fail by short-circuit. It is important to understand the nature of dendrite formation and growth in these high modulus electrolyte membranes in order to design strategies to prevent their growth.

An example of a radiograph image from the study is shown in Fig.2.1a . Fig.2.1b shows an example of a cross-sectional slice taken from the stack of reconstructed images. In this study, the sample cell was cycled until it failed by electronic short-circuit. From the reconstructed images, it is apparent that the majority of the lithium metal electrode interface is featureless. However, K. Harry finds globular lithium dendrites extending through the solid polymer electrolyte membrane like that shown in the 3D rendering in Fig.2.1c. The globular features in the polymer electrolyte are shrouded by the electrolyte itself. In contrast, the uniform character of the globular dendrite is clearly seen in the cross-section. Note that the above CT was taken at a relatively non-penetrating x-ray energy of 20 keV , thus a special pouch battery of 3 mm diameter was required for this study. With the high energy x-rays and large field of view at HEX, industrial batteries of about 25 mm in diameter can be imaged.

# X-ray microtomography imaging

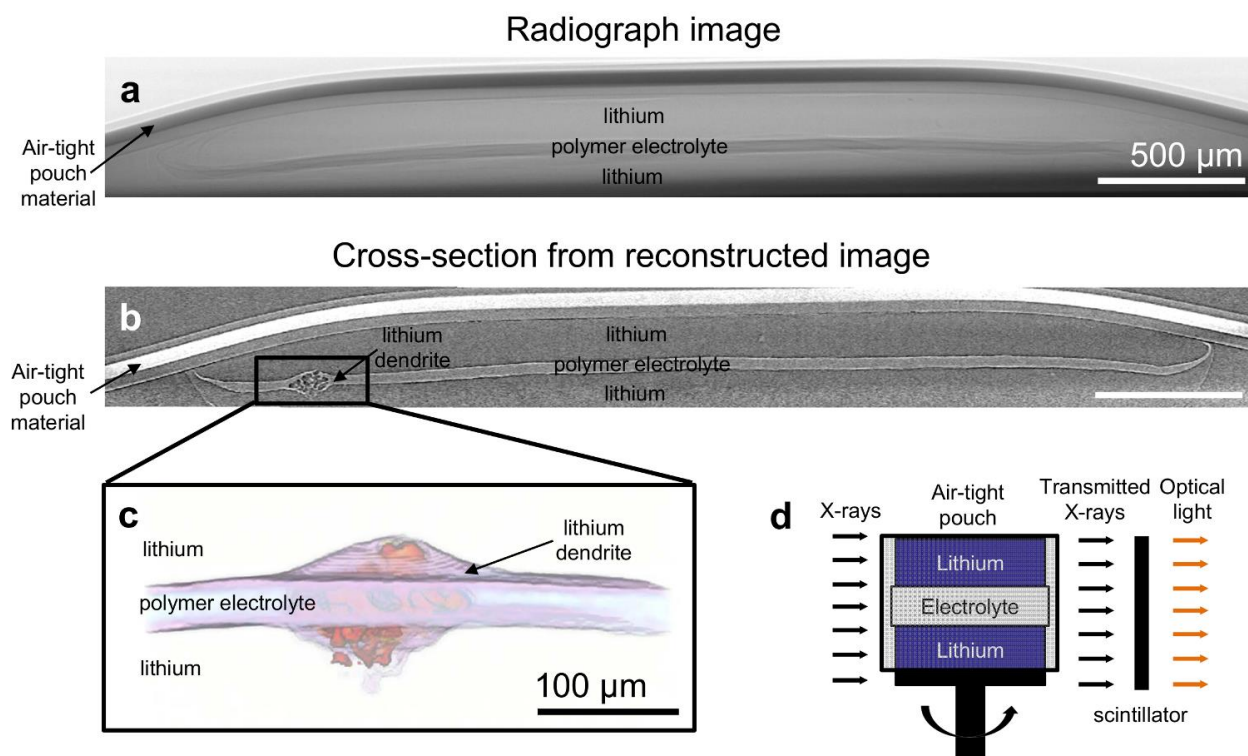


**Figure 2.2** (from K. Harry, <https://www.ncbi.nlm.nih.gov/pmc/articles/PMC4692560/>) Synchrotron hard X-ray microtomography is used to image a symmetric lithium cell that was cycled and failed by short circuit. **(A)** A radiograph image of the sample shows a dark polymer electrolyte band sandwiched between two lithium metal electrodes. The pouch material also appears in the image. **(B)** A cross-section slice through the reconstructed tomogram containing a lithium dendrite is shown. After reconstruction, the polymer electrolyte appears as a bright band sandwiched between two dark lithium metal electrodes. The pouch material also appears in the image. **(C)** Image segmentation was used to make a three-dimensional rendering of features in the sample. The dark, globular lithium metal dendrite is rendered in orange, so that the viewer can see its structure, while the bright, polymer electrolyte is rendered in purple. The top and bottom lithium metal electrodes are rendered transparent so they do not obscure the polymer electrolyte and the dendrite. **(D)** A schematic of the sample setup for X-ray microtomography experiments is shown.

Synchrotron phase contrast X-ray imaging was recently used to characterize different formations of Li microstructures in lithium electrochemical cells [18]. The improved spatial resolution and density differentiation enable the ability to discriminate between dendrite morphologies and compositions, namely metallic lithium and other HSAL (High Surface Area Lithium) deposits.

## 2.2 Engineering and Grid Materials



## Mechanics and Materials Science

In this section, we will review the new and emerging class of science that can be addressed by the HEX beamline. In recent years, high energy synchrotron radiation-based x-ray diffraction methods have been evolving, which allow such strain field profiling/ mapping of local strain field gradients, on the germane short length scales, deep in the interior of materials [19-30]. Such nondestructive cross-sectioning of the strain response, traversing a steep strain gradient, is now highly feasible for certain classes of problems in the elastoplastic deformation of solids. This capability provides a direct microscopic probe of the mechanical properties of materials on length scales down to the microns level.

As a result of the “Materials Science Engineering Strategic Planning for NSLS and NSLS-II workshop” [31] a white paper on “High-energy x-ray micro-mapping of materials: engineering applications” [32 (see link)] was written. This white paper gives specific case study applications of EDXD strain mapping to a range of materials deformation phenomena. Examples included were: compression processing techniques such as shot peening [22], laser peening, and split sleeve cold working (for rivet holes); residual strain profiling across a high-strength steel weld interfaces; and strain/phase profiling on plasma sprayed ceramic coatings on metals (for abrasion/corrosion resistance). The ability to profile beneficial or detrimental residual strains over the 10  $\mu\text{m}$  to several cm length scale was demonstrated. Also noted were a number of examples of practical engineering applications (including for the first time in situ battery studies) where such high energy x-ray strain/phase mapping could make important contributions.

Results presented at the workshop from Proto-Manufacturing Inc. shows impressive results on the  $\sim 200\ \mu\text{m}$  shot peening near-surface compression, along with the deep interior strains in Inconel 100 materials of interest to the Air Force. Moreover, the fatigue relaxation of the shot peened compressive layer under fatigue can be seen to ride upon a large and deep residual strain field also resulting from the bending fatigue process. Without such interior strain field information from the deeply penetrating x-rays, the near surface peening fatigue relaxation could be easily misinterpreted. It is worth noting that most of the surfaces inside turbojet engines are shot peened and are subject to vibrational fatigue.

A recent paper by the Rutgers group led by Tom Tsakalakos and Mark Croft reported EDXD measurements in the important Ti-6Al-4V aerospace alloy under in-situ four point bending [23]. This work allowed the exploration of elasto-plastic properties under both compression and tension. The group has also performed similar in-situ work emphasizing the anisotropic lattice elasto-plastic response on both Ti-6Al-4V and the nickel superalloy Inconel-100. This type of research provides a unique opportunity for studying plasticity phenomena in metals and alloys.

## Fatigue crack studies

It is in probing both the residual and load-induced strain fields in the vicinity of a fatigue crack tip that the EDXD techniques have been most groundbreaking [20-23]. Indications of this can be

found in recent tour de force synchrotron strain mapping articles from Withers's group [28] and Korsunsky's group [33] on the fatigue cycle overload effect.

### **Thermokinetics of Particulate Nanomaterials**

Time evolution of densification and microstructure in multi-component and multi-phase systems is a theoretically/computationally formidable area of materials research where there is little understanding of fundamental processes governing the sintering phenomenon. Of particular interest are the thermoelastic phenomena that take place during the processing of particulate nanomaterials with a particle size in the 100 nm range. Although there is a wealth of empirical evidence for increased mechanical strength in sinter-densified materials, the origin of these phenomena remains unknown. One such system is the  $Y_2O_3$ -MgO ceramic composite system in which such an increase in strength is observed. By using the HEX facilities, substantial advances in the understanding sintering in the <100 nm grain size range will be possible using in-situ high pressure and high temperature X-ray diffraction. The time evolution of thermokinetic and thermoelastic processes will be monitored by 3D phase and strain mapping and the microscopic sintering conditions determined and thereby optimized. The mapping of phases and strain in such materials will enable one to assess the elasto-optical coupling in multi-component and multi-phase systems processed at high temperatures and pressures, making such studies technologically important as most particulate nanomaterials are processed by hot isostatic pressing.

### **Mechanical Behavior of Nanostructured Ceramic Coatings**

High energy X-ray diffraction has proven to be most effective in the study of the mechanical behavior of nanostructured ceramic coatings on Ti-alloy substrates when coupled with in-situ 4-point bending [23]. It was found that the compressive strain due to the grit-blasting pre-deposition processing was present in all of the substrate strain profiles. The elastic response of both coatings under increasing bending moment is linear to a first approximation. However, the elastic strains are smaller in the nano- than the micro-coatings, which was indicative that the modulus of elasticity is larger in the nano-coatings. Also, a strain is observed from the interface to the surface of the coating, which is generated during plasma spraying. The high energy EDXD method's major advantage is that it allows one to assess the strain profile across the thickness of a given coating-substrate system in-situ and under load, which is otherwise not possible. This, in turn, enables one to analyze the micromechanics of the deformation process in a coating-substrate system in a phase-specific manner from which data-based models of the macroscopic deformation can be constructed.

### **Stress-corrosion cracking of materials**

Stress-corrosion cracking is encountered in virtually all aspects of structural engineering where a given load-bearing metallic member's mechanical strength decreases under the attack of the environment (water, salt water, water vapor). The HEX facility will enable US researchers to map the strains around the crack-tip in-situ under stress and in the hostile environment. The crucial crack tip strain field variation from the specimen center to the hostile-environment sub-surface surface will be accessible. This, in turn, enables one to obtain the elastic and plastic strains as well as the size of plastic zone in front of the crack as a function of the environmental

conditions and imposed stress. The deep penetration of HEX radiation will make it possible to obtain a microscopic picture of stress-corrosion cracking based on direct measurements, which can be used in theoretical analysis.

## 2.3 Development and Advisory Team

The development team consists of BNL team led by Andrew Broadbent. The team includes Eric Dooryhee, Erik Johnson, Mike Lucas, Chris Stebbins, Gregory Fries, and Zhong Zhong from the Photon Sciences Department of BNL.

Andrew Broadbent is experienced in superconducting magnets and has more than 15 years experience managing new beamline constructions at the Australian Light Source and NSLS-II. Zhong Zhong is the beamline scientist at the NSLS-II with 27 years experience in hard x-ray applications and instrumentation, and is fundamentally responsible for all of the work that has come out of the X17B1 beamline. Eric Dooryhee has more than 20 years experience in powder diffraction using synchrotron x-rays, and lead in the design, construction and operation of the XPD and PDF beamlines at the NSLS-II.

The beamline advisory team (BAT) consists of the following:

Michael Drakopoulos	Diamond Light Source	<a href="mailto:michael.drakopoulos@diamond.ac.uk">michael.drakopoulos@diamond.ac.uk</a>	+44 (0) 1235 778157
Esther Takeuchi	BNL	<a href="mailto:etakeuchi@bnl.gov">etakeuchi@bnl.gov</a>	631 344 4032
Yan Gao	GE Global Research	<a href="mailto:gaoy@ge.com">gaoy@ge.com</a>	518-387-6249
Mark Croft	Rutgers University	<a href="mailto:croft@physics.rutgers.edu">croft@physics.rutgers.edu</a>	(848) 445-8746
Jonathan Almer	APS	<a href="mailto:almer@aps.anl.gov">almer@aps.anl.gov</a>	(630) 252-1049

The BAT members cumulatively possess the necessary expertise and experience to implement the state-of-the-art HEX at the NSLS-II. M. Croft, an experimental solid state physicist, brings 30 years of experience in X-ray based research in materials science and also possesses experience in instrumentation design and development. Takeuchi is leader in the battery research field with large group and positions in research consortia. Y. Gao is a synchrotron experimentalist whose 30 years' experience is almost unparalleled in depth and breadth. Jon Almer manages the high-energy x-ray program at the APS, has three decades of experience in cutting edge high energy x-ray synchrotron research and is a world leader in the diffraction microscopy field. Moreover, he establishes a direct/synergistic connection with APS program. Michael Drakopoulos lead in the design, construction, commissioning and operation of the JEEP beamline to which HEX resembles in terms of source, optics and endstations.

## 2.4 Scope of HEX Project

### What is in the scope

1. Design, specification, procurement, installation and testing of superconducting wiggler
2. Design, specification, procurement, installation and testing of the front-end. In the front-end, the first mask will be designed to define three beam-lets. Subsequent mask(s) and collimators will accommodate all three beams. The front-end safety shutter will include only one shutter to shut-off all three beams together. The apertures for the beamlets will be discreet selections that include the option of complete block-off of the beamlet.
3. Design of the FOE and experimental enclosures to accommodate the three branches.
4. Specification and procurement of experimental enclosures for the three branches.
5. Design of the beamline optics (including imaging monochromator, vertical-focusing monochromator and focusing mirror for the center branch, side-bounce monochromator and vertical-focusing mirror for side branch) to accommodate the three branches.
6. Design, specification, and procurement of the imaging monochromator for center branch.
7. Design, specification, and procurement of the white-beam shutter for the center branch.
8. Design, specification, and procurement of beam-stops for the white-beam and side branches.
9. Design, specification and procurement of EDXD, imaging and ADXD experimental systems for the center branch. The three techniques will share the same beam conditioning (slits, filters, ion chambers) system and will share two sample stages, one for large sample and one for small sample. The detection systems for the three techniques will be moved in and out of the beam depending on the technique being used for the experiment.

### What is NOT in the scope

1. Shutters for the white-beam and side branches.
2. PPS for the white-beam and side branches
3. Beam transport pipes for the white-beam and side branches.
4. Procurement of sagittal-focusing monochromator and vertical focusing mirror for the center branch.
5. Procurement of side-bounce monochromator and vertical-focusing mirror for the side branch.
6. Design and procurement of the experimental systems for the white-beam and side branches.

## 2.5 What's Next

The following is planned in the next year to transition from PDR to FDR:

1. Perform final engineering design of the front-end and ID straight section.
2. Perform engineering design of the beamline that is detailed enough for obtaining vendor quotes.
3. Specify the superconducting wiggler in enough detail that a vendor quote can be obtained and/or work out a route for producing or assembling this in-house.

4. Complete radiation shielding analysis to enable specification of the experimental enclosures on the experimental floor.
5. Finalize beamline endstation equipment design and specifications.

### 3 HEX BEAMLINE

Figure 3.1 shows the layout and design concept of the HEX beamline. It illustrates the four pillars of the HEX design concept:

1. Emphasis on White Beams (2 considered)
2. Three independent branches
3. Imaging and Diffraction
4. Satellite building and concrete experimental enclosure

Here we briefly summarize what each of the four pillars means, and why they are important for achieving the scientific and technical goals of HEX as defined in chapter 2.

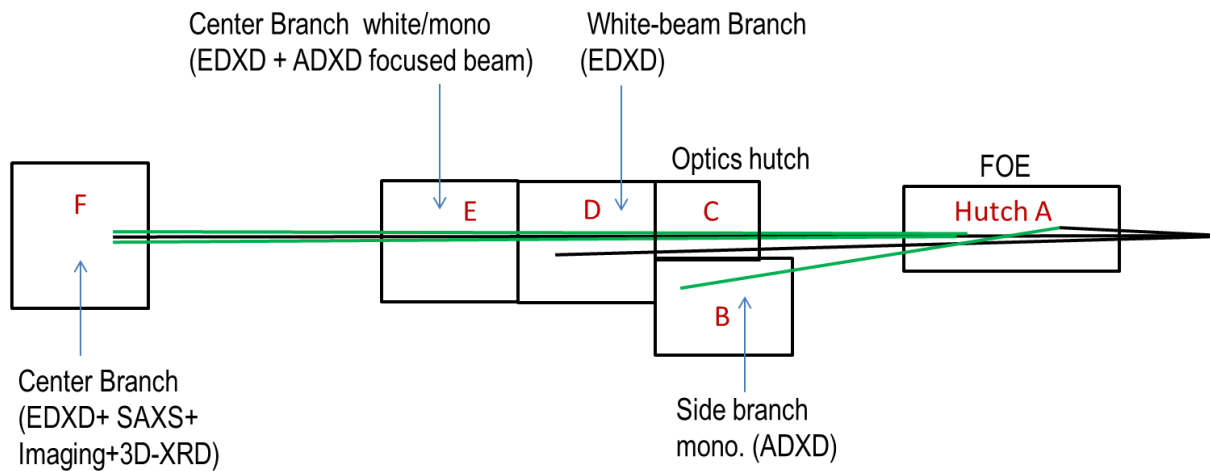


**Figure 3.1:** Layout of the HEX beamline at the ID-27 port of the National Synchrotron Light Source II, Upton, New York. The branch going to the F-hutch is the only branch included in the initial scope.

#### Emphasis on White Beams (2 considered)

White beam is necessary for EDXD. Since HEX is the first superconducting wiggler beamline at the NSLS-II, it will need to offer maximum flexibility to accommodate a variety of research needs. While white beam hutches can run both white- and monochromatic-beams, an experimental enclosure that is designed for monochromatic beam cannot be used for white-beam experiments in the future without a major and disruptive retrofit. Furthermore, white beam hutches allow for a small gap on the double-crystal monochromator, resulting in superior stability and lower optics cost.

#### Three independent branches

HEX will be designed to accommodate three independent branches. The large, greater than 9 mrad, wiggler fan allows segregating the fan into three branches. The distribution of the three

branches are:

- Side branch is a fixed energy (~80 keV) branch for ADXD;
- Center branch is the main branch capturing 1.0 mrad on the center of the wiggler fan, offering ADXD, EDXD with multi-element detector and imaging. This branch will have 2 time-share endstations in tandem.
- The white-beam branch captures 0.2 mrad and in the future will serve as a work-horse EDXD beamline.

## **Imaging**

3D visualization under real operating conditions is crucial for understanding fuel cell, batteries, and engineering materials. HEX's high-flux, high-energy x-rays, with a large field of view of 20 mm (V) by 100 mm (H), enable in-situ imaging of large samples. We note that in many cases phase contrast imaging (propagation, grating-based, or analyzer based/diffraction enhanced imaging) is superior to absorption contrast.

## **Satellite building and concrete hutch**

In line with the worldwide trend for high-energy superconducting wiggler beamlines, HEX center branch will have one concrete experimental enclosure in a satellite building. The experimental enclosure offers high ceiling to accommodate large samples and mechanical testing equipment, and complex experimental setup. The hutch will offer dedicated gas exhaust system for battery and fuel-cell research. The large satellite building allows for small-angle scattering with sample in the E hutch and detector in the concrete hutch. According to the JEEP and HXN (hard x-ray nanoprobe) experience, a concrete hutch is cost-effective compared to a lead hutch. The large distance to the source benefits propagation phase contrast imaging which requires a large distance to the source, and provides a large field of view (especially vertical) for imaging.

Figure 3.2 shows the design of the HEX beamline, over 100m long. This consists of the following sub-systems:

- Photon delivery system
- Experimental equipment
- Experimental enclosures (hutches)
- Beamline infrastructure and safety system
- Frontend
- Source (SCW)
- Straight section
- Controls
- Satellite building

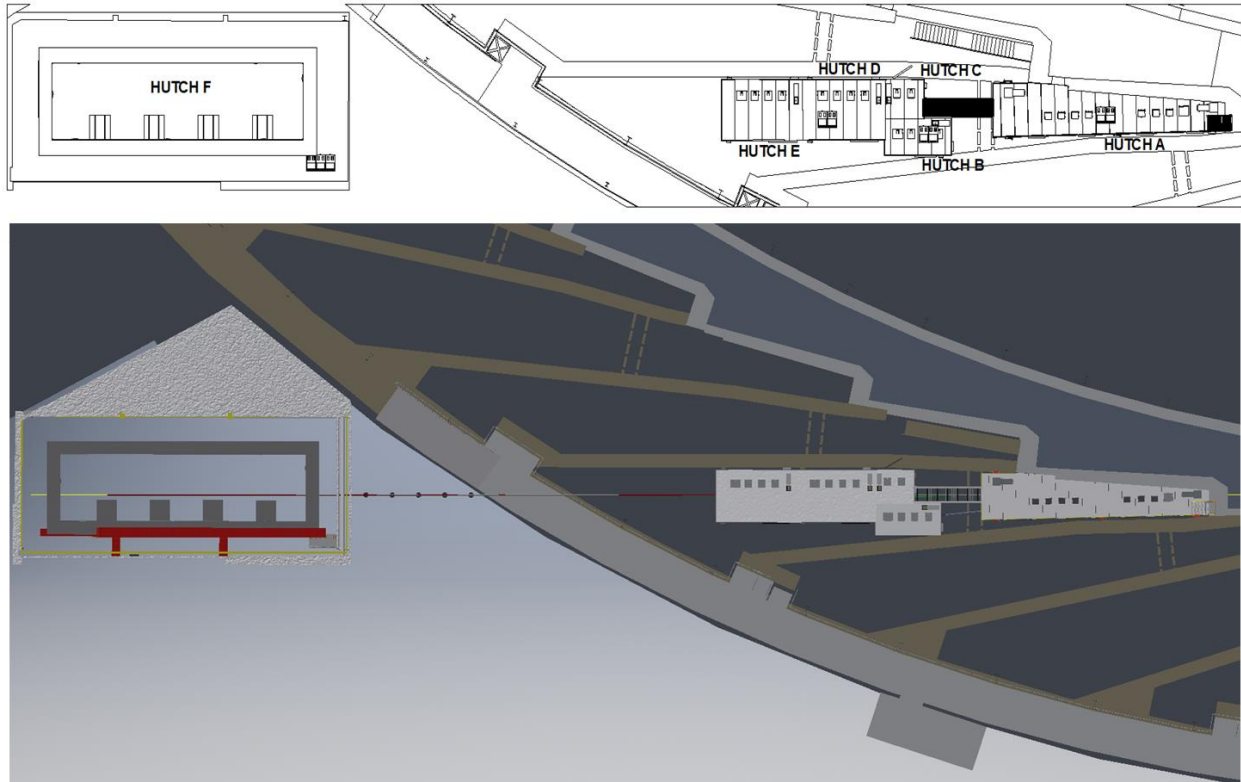


**Figure 3.2:** Preliminary Design of the HEX beamline at the ID-27 port of the National Synchrotron Light Source II, Upton, New York.

The HEX beamline design is largely based on the proven design concept at the NSLS X17 superconducting wiggler beamline, which was the world's first superconducting wiggler beamline, having been in service for more than 30 years. The X17 beamline over the years generated many innovations that include Diamond Anvil Cell (DAC), Digital subtraction angiography, Microbeam Radiation Therapy (MRT), Sagittal-focusing monochromator, and Strain- and phase-mapping with EDXD.

We describe in this chapter the HEX Beamline in terms of source, front-end, white-beam transport and conditioning.

### 3.1 Super-conducting Wiggler Source

At NSLS-II, the machine energy is 3GeV, compared to 6GeV, 7GeV and 8GeV, respectively for ESRF, APS and SPRING8. To-date, the highest critical energy at NSLS-II is offered by damping wigglers of 1.8 T field with a critical energy of 10.8 keV. At 80 keV, the flux rate of a superconducting wiggler (SCW) is an order of magnitude higher than that provided by a damping wiggler. A superconducting wiggler is therefore chosen to provide the desired high-energy x-rays for the HEX program.



The radiation is broadband with high power at high x-ray energies. For HEX imaging and micro-focusing components, the brightness should be as high as possible, which means the wiggler period length should be as small as possible. The combination of high field and small period requires a super-conducting wiggler design. Such devices are available commercially.

As the critical energy  $E_c$  of a wiggler scales with the square of the storage ring energy  $E$ , as  $E_c[\text{keV}] = 0.665 B[\text{T}] E^2[\text{GeV}^2]$ , a high magnetic field is necessary to produce a high-energy x-ray spectrum. However, the horizontal fan of the emitted radiation needs to be kept within the boundaries given by the design of the straight section and the front-end. The total emitted power is also affected by the choice of wiggler parameters. The width of the horizontal fan is proportional to the deflection parameter  $K$ , with  $K = 0.93 B_0 \lambda$ , where  $B_0$  is the peak magnetic field in Tesla, and  $\lambda$  is the period length in cm.

The total power  $P$  (kW) is given by  $P = 0.633 E^2 B_0^2 L I$ , where  $L$ (m) is the length of the wiggler, and  $I$  (A) is the storage ring current. Increasing the peak magnetic field has the desired effect of increasing the critical energy; however, the deflection parameter increases by the same factor (linear in  $B_0$ ) and the total emitted power escalates (as the square of  $B_0$ ). The source size, viewed off-axis, is proportional to the length of the wiggler, so a 1 m device length is preferred to minimize the source size for the C branch, which will be oriented  $\sim 3$  mrad off-axis.

A 1 m long superconducting wiggler with 80 mm period and 4.5 T peak field is designated SCW80 in the NSLS-II CD0 proposal for HEX. This wiggler provides a 26.9 keV critical energy, higher than the 20 keV critical energy of the NSLS X17 SCW, and is well suited for HEX. Note that SCW80 provides a horizontal fan size of 11.5 milli-radians which exceeds the fan that can be extracted from the storage ring, estimated to be about 6 milli-radians, resulting in about half of the radiation fan being un-used. Furthermore, a recent preliminary design of the HEX ID-straight and front-end by the NSLS-II insertion device and front-end group indicates that if the horizontal fan is larger than 10 milli-radians, substantial redesign, if possible at all, of the accelerator components at the ID straight section and front-end would be required.

To minimize the technical risk and inevitable high cost of the re-design, a 4.3 T wiggler with 70 mm period, designated SCW70, has been proposed (Oleg Tchoubar). SCW70 is more suitable for HEX due to its compatibility with front-end design, and higher brightness in the spectral range we are interested in, as shown in Fig. 3.3 below.

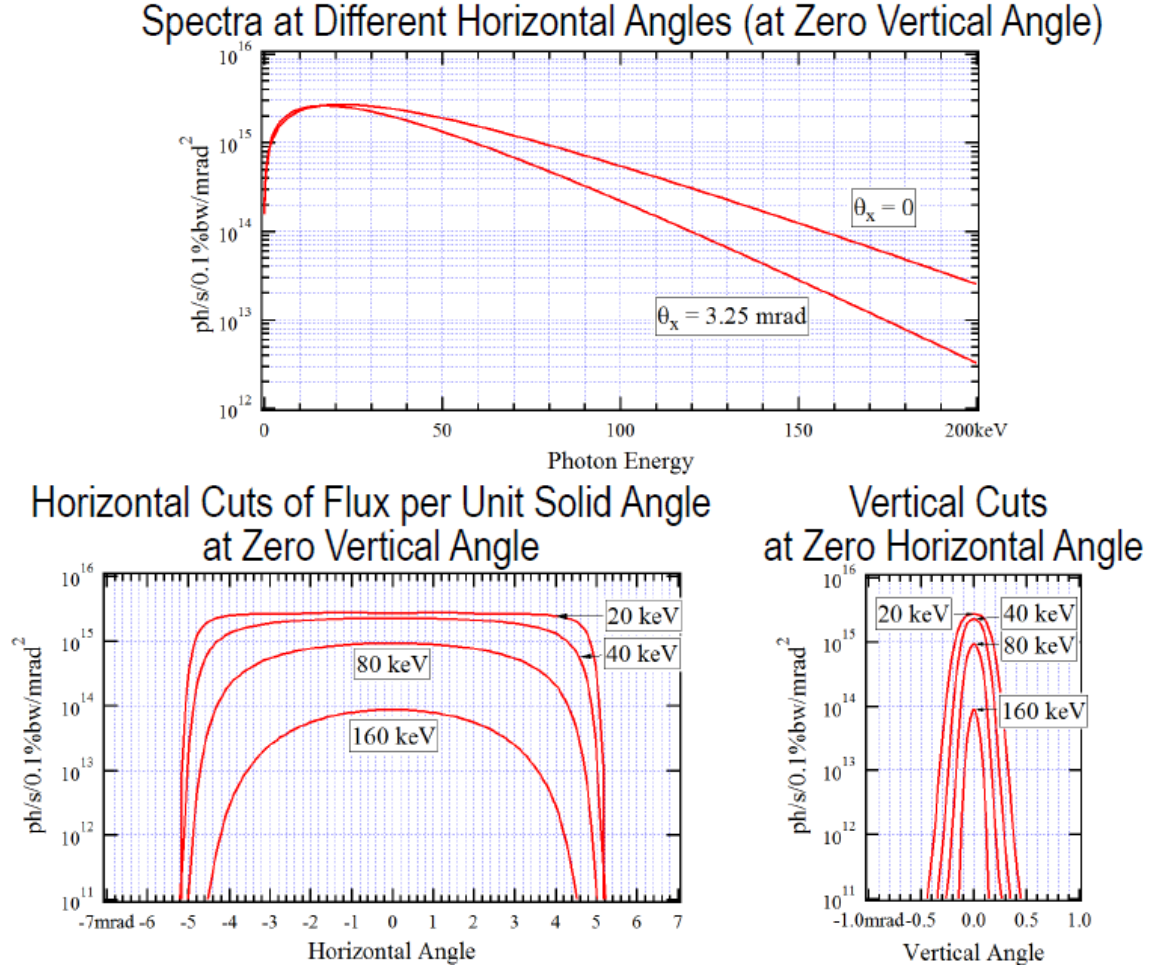


**Figure 3.3:** Spectral angular distribution of x-rays from SCW70.

The specifications of the proposed wiggler SCW70 and the alternatives SCW55 and SCW80 are listed in table 3.1:

	SCW55	SCW70	SCW80
Magnet Field $B_0$ (T)	4.2 T	<b>4.3 T</b>	4.5 T
Period Length $\lambda$ (cm)	5.5	<b>7</b>	8
Number of Main Poles (N)	31	<b>29</b>	25
Wiggler Magnetic Length L (m)	0.85	<b>1.015</b>	1.0
Critical Energy $E_C$ ( $0.665BE^2$ ) (keV)	25.1	<b>25.7</b>	26.9
Deflection Parameter ( $K=0.93B_0\lambda$ )	21.5	<b>28.0</b>	33.5
Radiated Power at 500mA ( $5.7B_0^2LI$ ) (kW)	42.7	<b>53.5</b>	57.7
Fan size ( $2K/\gamma$ ) (mrad)	7.3	<b>9.5</b>	11.4

Amplitude of electron oscillation ( $x_0 = \lambda_w K / (\gamma \pi)$ ) (microns)	64	<b>106</b>	145
---	----	------------	-----

**Table 3.1.** Specifications of the SCW70, along with alternative SCW55 and SCW80.

In the table above,  $\gamma=5871$  is the relativistic factor for the storage ring, calculated as  $\gamma=E/E_R$ , where  $E$  is the energy of the storage ring, 3 GeV for NSLS-II, and  $E_R$  (0.511 MeV) is the rest mass of the electron.

Specifications of similar wigglers that are currently in service at medium-energy synchrotrons are listed in table 3.2. It shows that the HEX wiggler specification is conservative for superconducting wiggler technology, both in terms of magnetic field and in terms of field-to-period ratio.

Facility	Manufacturer	Field(T)	Period (cm)	# full-field poles
NSLS X17	Oxford	6	14.7	5
BESSY II	Budker Institute	7	14.8	13
CLS (BMIT)	Budker Institute	4.2	4.8	25
ELETTRA	Budker Institute	3.6	6.4	45
DIAMOND	Budker Institute	4.2	4.8	45
CLS (HXMA)	Budker Institute	2.1	3.4	61
<b>NSLS-II (HEX)</b>	<b>TBD</b>	<b>4.3</b>	<b>7.0</b>	<b>29</b>

**Table 3.2.** A partial list of working super-conducting wigglers similar in specifications to our proposed wiggler SCW70.

The HEX beamline will be sited at ID27 which is a low-beta straight section. The specifications of superconducting wiggler, as detailed in the current RSI document “RSI for the Superconducting Wiggler Source and Front End for the HEX Beamline” (NSLSII-27ID\_RSI-001 version 2, March 2018), are shown below.

Beamline	HEX
Type	SCW
Device envelope length	~1.8 m
Magnetic Length	1.2m nominal (29 main and 4 partial poles)
Canted	No
Period: nominal	70 mm
Nominal (minimum) gap of vacuum bore tube *	10 mm TBC
Peak field nominal	4.3 T
Keff: nominal	28.1 <sup>*1</sup>
Energy Range:	8 keV –200 keV
Power total: nominal	55.7 kW <sup>*1</sup>
Max.power per unit solid angle: nominal	28.4 kW/mr <sup>2</sup> <sup>*1</sup>
Straight	Low beta
Device center <sup>*2</sup>	May be offset in the straight to the downstream end.
Fan angle <sup>*3</sup> (mrad H) : nominal (maximum)	9.87 (10.15)
Fan angle <sup>*3</sup> (mrad V) : nominal (maximum)	0.88 (1.47)
Magnetic field variation range	Current adjustment 0 – 100%

**Note 1:** Assuming sinusoidal magnetic field distribution in central part of the wiggler.

**Note 2:** The ray tracing should accommodate axial movements of the IDs by +/-5mm, which might be required in the design of the straight.

**Note 3:** The fan angles of the radiation quoted here are as seen at 16m from the source, and take into account the effects of source length; the worst case fan size is taken. The two values quoted are for the points where the power density falls to values that are 1% and 0.1% of the central value. Designs of the fixed mask entrance shall take into account these fringe power loads.

**Table 3.3:** HEX SCW specifications.

The impact of SCW55 and SCW80 on the emittance and momentum spread of the NSLS-II electron storage ring is small, as illustrated in table 3.4. The impact of SCW70, similar to that of SCW55 and SCW80, is expected to be small.

Impact on Storage Ring	Emittance (nm)	Momentum spread (%)
Lattice+3DW	0.91	0.083
Lattice+3DW+SCW80	0.79	0.097
Lattice+3DW+SCW55	0.81	0.094

**Table 3.4:** Impact of an SCW on the NSLS-II storage ring

Simulation of the spectral flux of SCW70 is shown by the green line in Fig. 2.1. At 500 mA ring current, the spectral flux is approximately  $10^{15}$ - $10^{14}$  ph/s/0.1%bw/mrad<sup>2</sup> from 30 to 150 keV. For comparison, the spectral flux for the NSLS-X17 wiggler, and the NSLS-II damping wiggler are also shown.

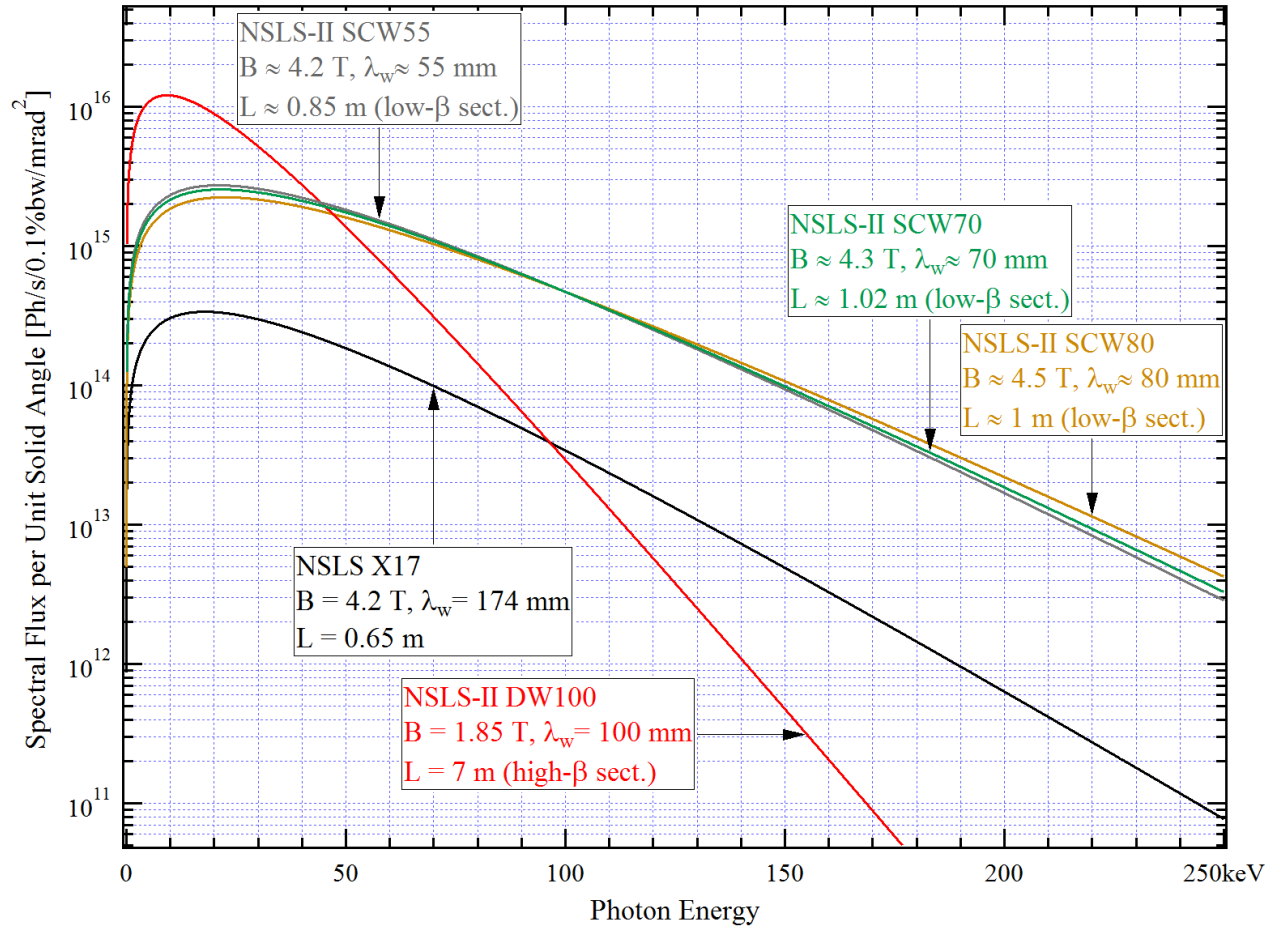


**Figure 3.4:** Spectral flux per unit solid angle of SCW. Electron beam current is assumed to be 500 mA.

Figure 3.5 shows the power load per unit solid angle by SCW70 and SCW55/SCW80 compared to other insertion devices at the NSLS-II. Note that SCW70 has comparable horizontal and vertical divergences as the damping wiggler DW100, but has less power density than the damping wiggler. Thus, we can use experience gained by the XPD facility beamline and the ISS beamline (both of which use DW100) to guide our optical design, especially regarding heat-load management.

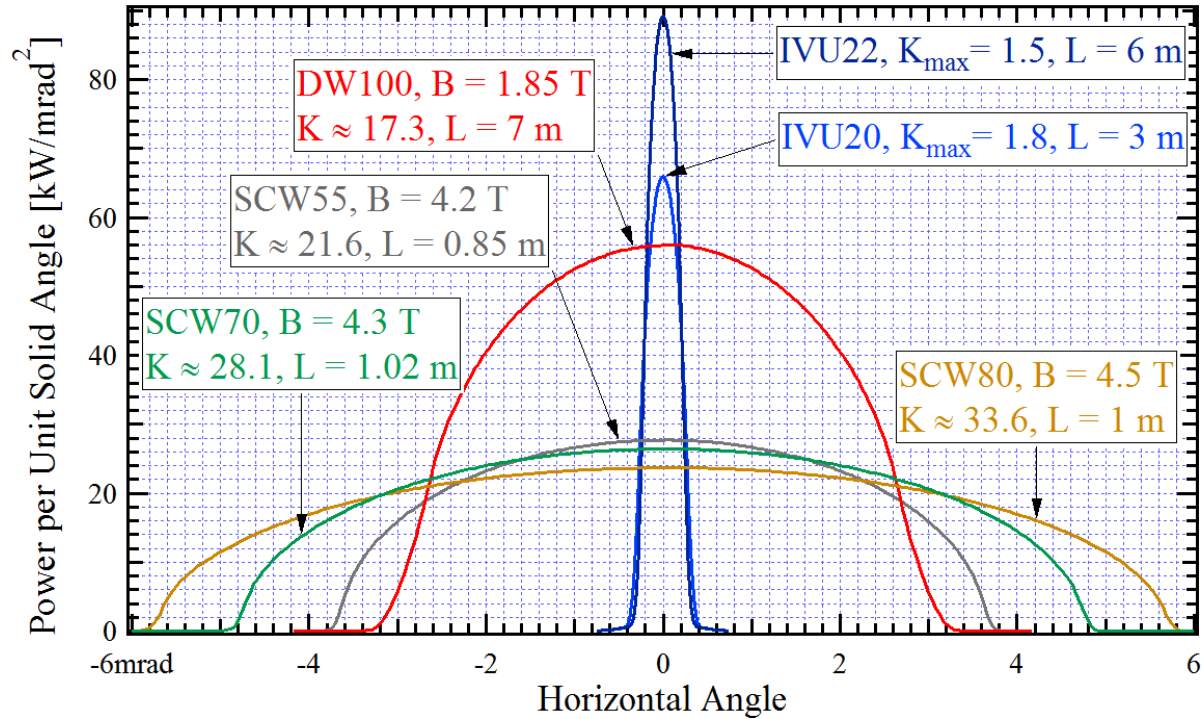


**Figure 3.5:** Power load variation with horizontal divergence by SCW55 and SCW80 compared to other insertion devices at the NSLSII. (courtesy of Oleg Tchoubar)

SCW70 provides peak power density of  $28.4 \text{ kW/mrad}^2$ . The maximum power through the  $0.2$  by  $1 \text{ mrad}^2$  front end fixed aperture is  $5.7 \text{ kW}$  for center and  $1.1 \text{ kW}$  for side branches. The power density and total power for both devices are much less than those of the NSLS-II IVU undulators and damping wiggler. Fig. 3.5 shows that the power density is  $60$  to  $90 \text{ kW/mrad}^2$  for the IVU22 and IVU20 beamlines at NSLS-II. Thus, we can rely on experiences gained by the facility beamlines to guide our optical design, especially regarding heat-load management.

Simulated magnetic field distribution, horizontal position and angle of the electrons as a function of position along the wiggler length are shown in figure 3.6. It is seen that the maximum excursion of the electron from inboard to outboard is about  $100$  microns. This excursion dominates the horizontal source-size of the irradiated x-ray beam.



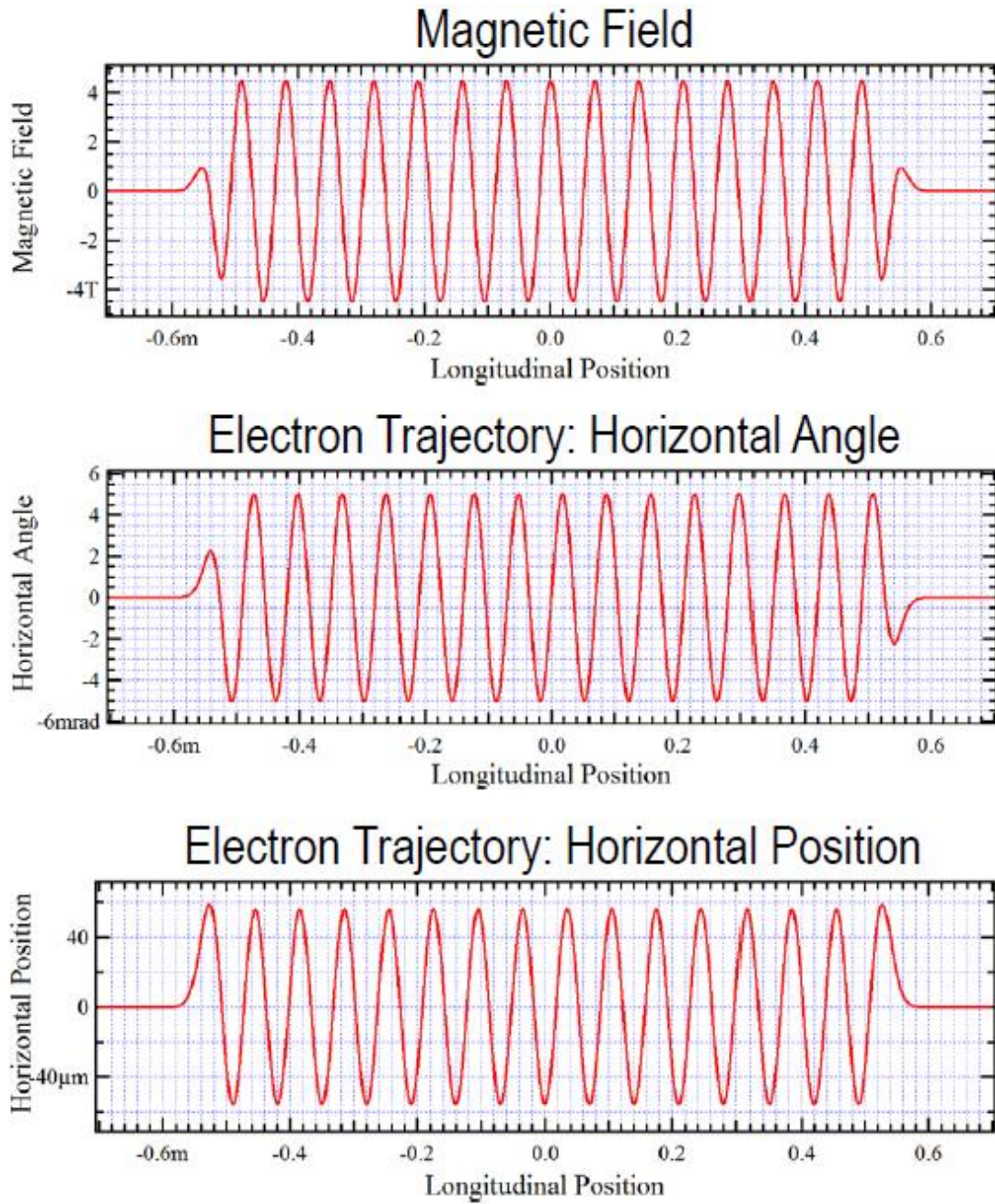


**Figure 3.6:** Model of the magnetic field and electron trajectory in SCW70.



### 3.2 Front End

The front end is also similar to the standard front end design, with the opening angle customized to be 0.2 milli-radians vertically. Instead of having a fixed mask with one or two apertures, HEX will have a fixed mask with three apertures to accommodate the three HEX beamlines. Specifications for the front end components are shown in Table 3.5. No mirrors are planned for the front-end.

	HEX
Photon shutter (BMPS)	Y
Slow Gate Valve (SGV)	Y
Beam Position Monitor 1 (XBPM1)	N
Beam Position Monitor 2 (XBPM2)	N
Fixed Mask (FM)	Y (Mk2 design)
Type	Triple aperture
Source	SCW
Vertical aperture (mrad)	0.2 mrad *Note 1
Horizontal apertures (mrad)	Location and Aperture Size
	HEX
In-board	At 1.15 mrad, 0.2mrad H
Center	At 0 mrad, 1.0mrad H
Outboard	At 3.0 mrad, 0.2mrad H
Tolerance on apertures	+/-0.01mrad
Shape	Corner Radius
Bremsstrahlung Collimator BC1	Y
Water Cooled Beryllium Window	N
Fast Gate Valve (FGV)	Y
Number of X-Y Slit sets	3
X-ray flag	N
Fixed Mask 2	Y
Gate Valve	N
Diagnostics Cross	N
Photon Shutter (PSH)	Y
Bremsstrahlung Collimator BC2	Y
Safety Shutter (SS) (x2)	Y
Cycles per year required	50,000
Ratchet Wall Collimator	Y
Gate valve outside Ratchet Wall	Y

Table 3.5: HEX front-end component specifications.

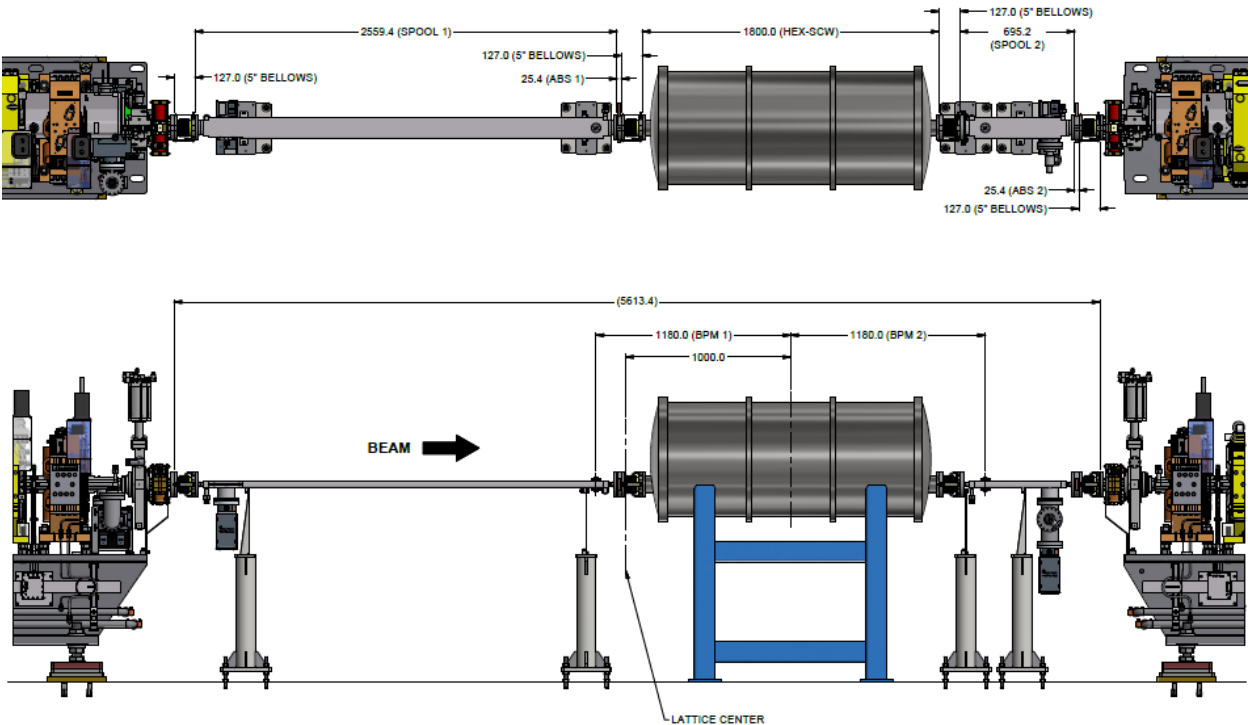
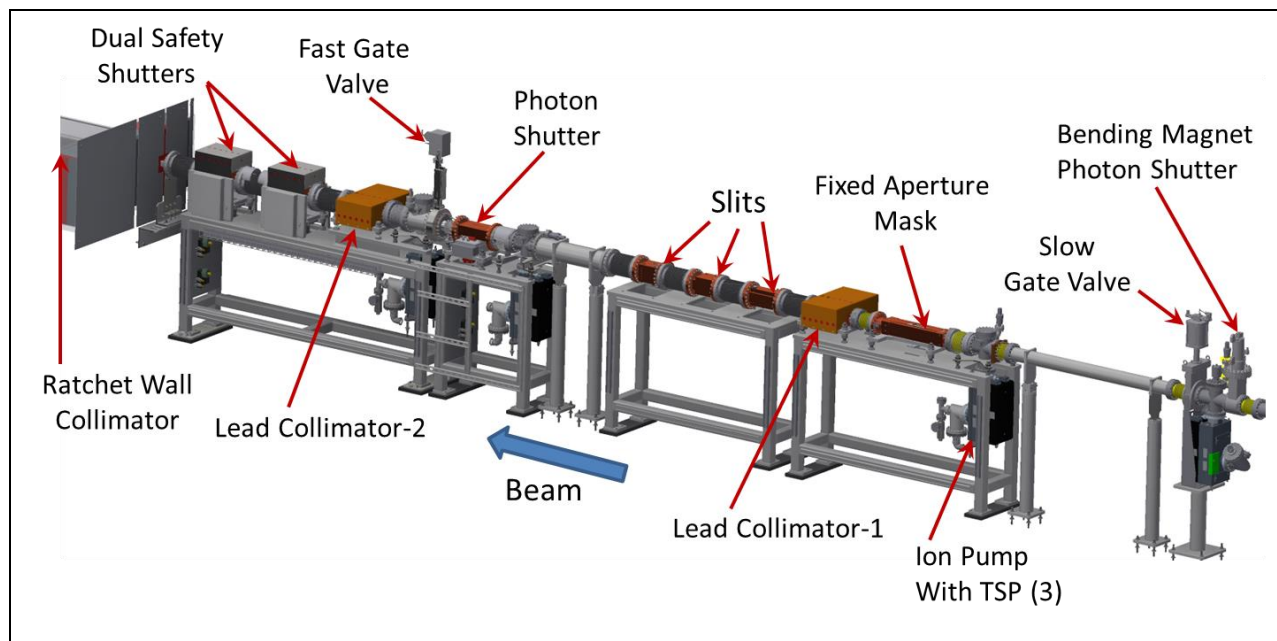


Figure 3.7 Proposed layout of the 27-ID straight section.

A layout of the HEX straight section at ID-27 is shown in Figure 3.7. It is seen that the longitudinal center of the wiggler is 1 m downstream of the center of the straight section. The offset is necessary to prevent the wiggler's synchrotron fan from striking the storage ring vacuum chamber. Beam Position Monitors (BPM 1 and 2) provide electron orbit information for active interlock.



**Figure 3.8:** Preliminary design of the HEX front-end.

The preliminary design of the HEX front end is shown in Figure 3.8. HEX will utilize a new fixed three-aperture mask design to provide radiation fans to the FOE. The mask is at approximately 17 m from the source. The preliminary design of the fixed mask for HEX is shown in Figure 3.9. It provides three beamlets for the three HEX branches. The inboard aperture, at  $-1.15$  mrad, will provide white beam to the side-branch monochromator. The center beam serves the center branch with  $1.0$  mrad horizontal divergence. The small aperture at  $3$  mrad outboard provides a white beam, with adequate separation from the center branch beam, for the white-beam branch.

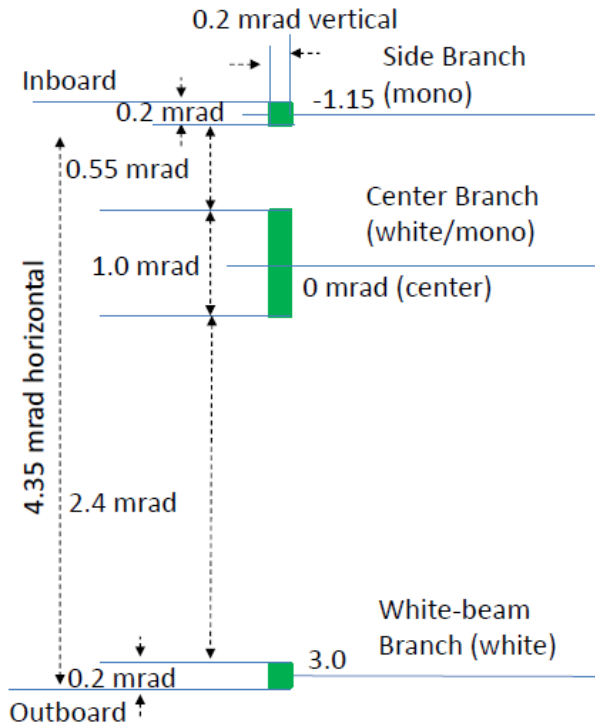


**Figure 3.9:** Preliminary design of the HEX fixed mask.

The new design of fixed mask uses CuCrZr alloy which is considerably less expensive than Glidcop, is now well-proven at the NSLS-II, and uses only vertical tapering so that the region between the two apertures is passively safe for the unused portion of the wiggler beam. The CuCrZr alloy allows for integral conflat flange, thus eliminating the need for brazing stainless-steel flange to Glidcop mask, an undesirable feature in the old design. The mask will be tapered to safely absorb possible mis-steered wiggler beam. The vertically tapered beam-intercepting surface features internal fins to improve thermal efficiency.

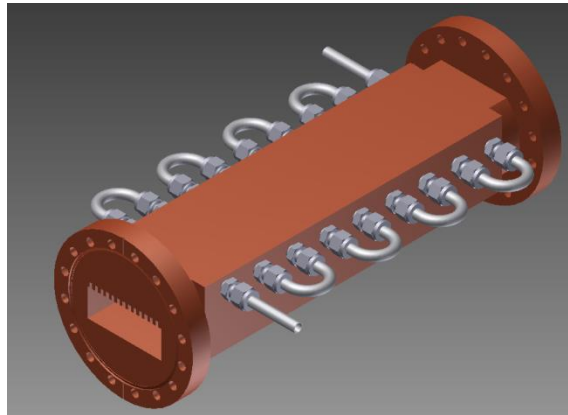


**Figure 3.10:** Design concept of the new front end fixed aperture mask. SST was the first

13-April-2018

beamline at the NSLS-II to utilize this new design. HEX will benefit from the experience gained at the SST beamline.

Simulations (results shown in Fig. 3.11) performed by Sushil Sharma show that this design keeps the water-cooled surface below 300°C at normal-incidence power density of 103 kW/mrad<sup>2</sup>. The resulting temperature and stress distribution are shown in Figure 2.8. It is assumed that the full beam is intercepted by the mask. This is a worst-case scenario which accounts for any mis-steering of the beam. Compared to the assumed 103 kW/ mrad<sup>2</sup>, the maximum power per unit solid angle at HEX is much less at 28.4 kW/mrad<sup>2</sup>. Thus we are confident that the basic design of the fixed mask is conservative for HEX.

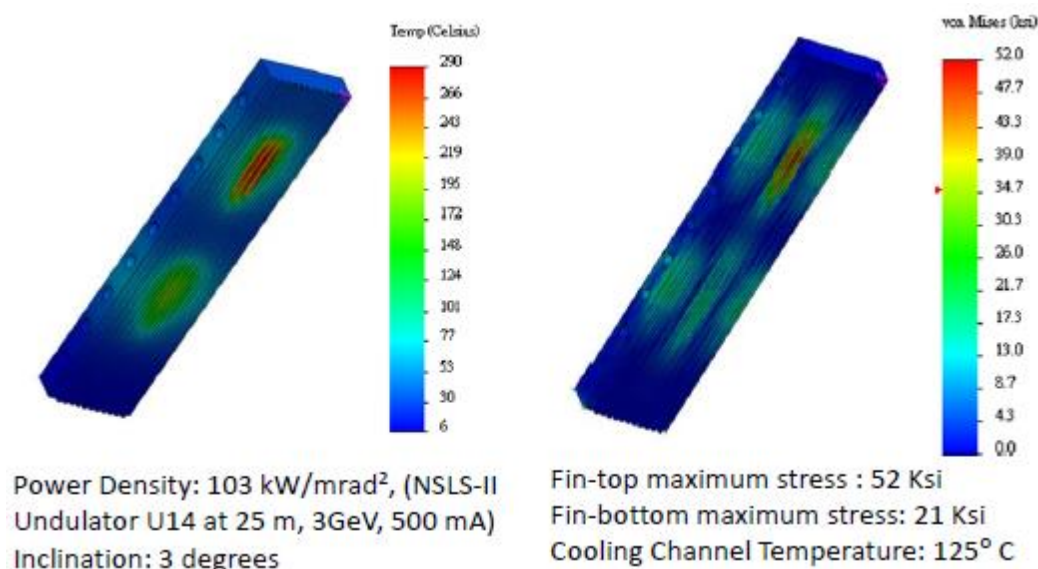


**Figure 3.11:** Parameters and FEA result for the front-end fixed aperture mask.

We plan to use the same design for the fixed mask at the upstream end of the FOE. This mask can have larger taper angle due to lower power density

Due to the small angular space between the center branch and the side branch, it is not feasible to use L slits in the frontend region. Thus all three branches will be designed with discrete apertures that include the option to completely block the beam for that branch. Fig3.12 below shows that preliminary design of the branch slit apertures.

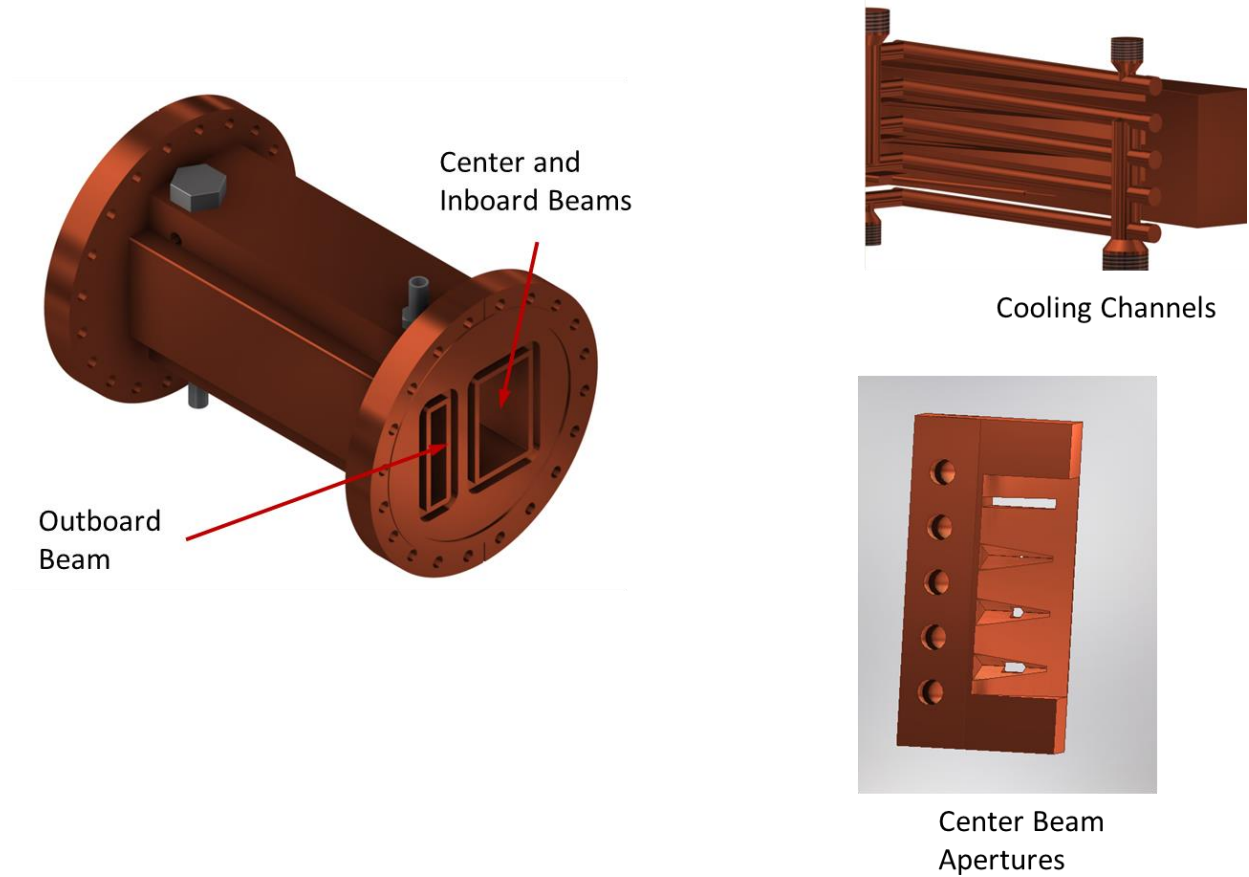


**Figure 3.12:** Preliminary design for the HEX front-end adjustable apertures

### 3.3 White Beam Management

The HEX beamline first optical enclosure (FOE), shown in figure 3.13, contains three groups of components: beam conditioning, optics, and the shutter/collimator. The beam conditioning group shapes and conditions the white beam coming from the front end. The optics group consists of three monochromators and two mirrors for the middle and fixed-energy branches. At the downstream of the FOE, three shutters, one for each branch, are followed by fixed mask/Bremsstrahlung collimator combination. In this section, we will discuss the beam conditioning components at the beginning, and the shutter/collimator at the end of the FOE. The optics, due to its uniqueness, will be discussed separately in the next chapter.

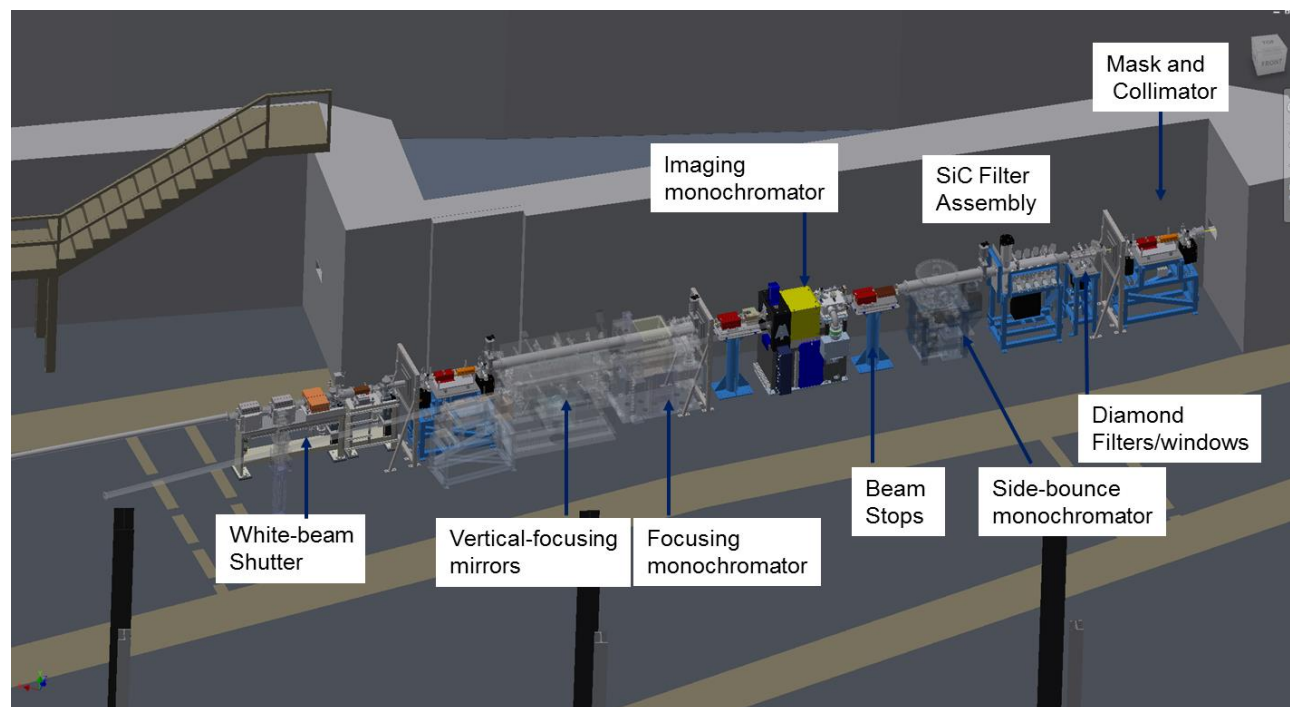


**Fig 3.13:** Overview of the HEX first optical enclosure.

The beam conditioning group includes a fixed water-cooled mask that collimates the three HEX beams followed by a Bremsstrahlung collimator, diamond filters followed by diamond windows, fixed silicon carbide (SiC) filters and removable SiC filters.

### Water-cooled Fixed Mask

The water-cooled fixed mask aperture will be of the same basic design as that of the new front-end fixed mask. The heat load from the incident beam is distributed across a large surface area by the use of grazing incidence geometry.

The segregation of the wiggler fan beam is achieved by the fixed mask in the front-end. The fixed mask located at the upstream end of the FOE passes the same angular space as the front-end fixed mask and serves to protect the Bremsstrahlung collimator just downstream of it from any mis-steered beam.

### Filtering Module

The design of the white-beam conditioning components, including diamond filters, diamond windows, and SiC filters, closely follows the design used by the XPD and PDF beamlines at NSLS-II.

Figure 3.14 shows the preliminary design of the diamond filter/window module, followed by fixed SiC filter(s). This diamond window/filter module is located downstream of the fixed mask in the FOE. The function of the diamond filter/window module is to filter the white beam, using water-cooled clamped diamond filters, to low enough power density to not damage the downstream water-cooled diamond windows. The diamond windows serve to isolate the beamline vacuum from the ring vacuum and to further filter the beam. The fixed SiC filters are designed to assure survivability of downstream monochromator crystals in the worst-case event that all removable filters are removed and the slits are opened to the maximum position.

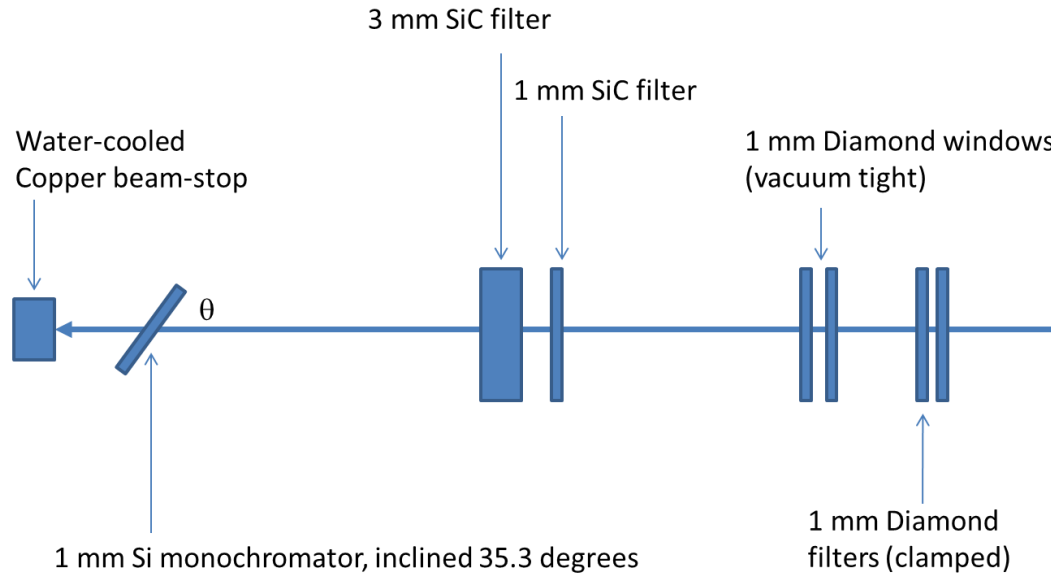


**Fig 3.14:** Preliminary design of the diamond filter/window module, followed by SiC fixed filter module.

To assure survivability of the filters and windows, worst-case power load were calculated for each component, and FEA will be performed based on the power load.

The XOP application “Wiggler Spectrum” was used to simulate the wiggler spectrum. 3 GeV ring energy, 500 mA ring current was assumed for the storage ring. A superconducting wiggler of 7 cm period and 14 periods was assumed. The field was assumed to be 4.3 T, with  $K_y$  being 28.22. The simulation shows that the wiggler provides x-rays with a total power of 55 kW, with on-center power density being  $23.6 \text{ kW/mrad}^2$ . This spectrum is then used to simulate the power load on windows, filters, monochromators, as well as to simulate the performance of optics.

A program was then written in IDL programming language to calculate the worst-case absorbed power from windows/filters. To be conservative, absorbed power is assumed to be incident power minus the transmitted power, hence ignoring the scattered x-ray power. The spectrum from the center  $0.1 \times 0.1 \text{ mrad}$  is used.

Fig.3.15 shows the simulated incident spectra on the window and filtering elements. The monochromator is assumed to be 2 mm thick Silicon crystal, inclined at 35.3 degrees, resulting in 3.5 mm along the beam path. It shows that the filtering elements progressively remove power, particularly at x-ray energies below 20 keV, while preserving most of the high-energy x-rays



above 50 keV. Diamond, being low-Z, is effective at filtering unwanted x-rays below 10 keV, while SiC, with higher Z than carbon, is effective at filtering unwanted 10-30 keV x-rays. The combination of diamond and SiC filters is ideal for conditioning the HEX beams, to reduce the power density of the beam incident on monochromator while preserving the high-energy x-ray flux.

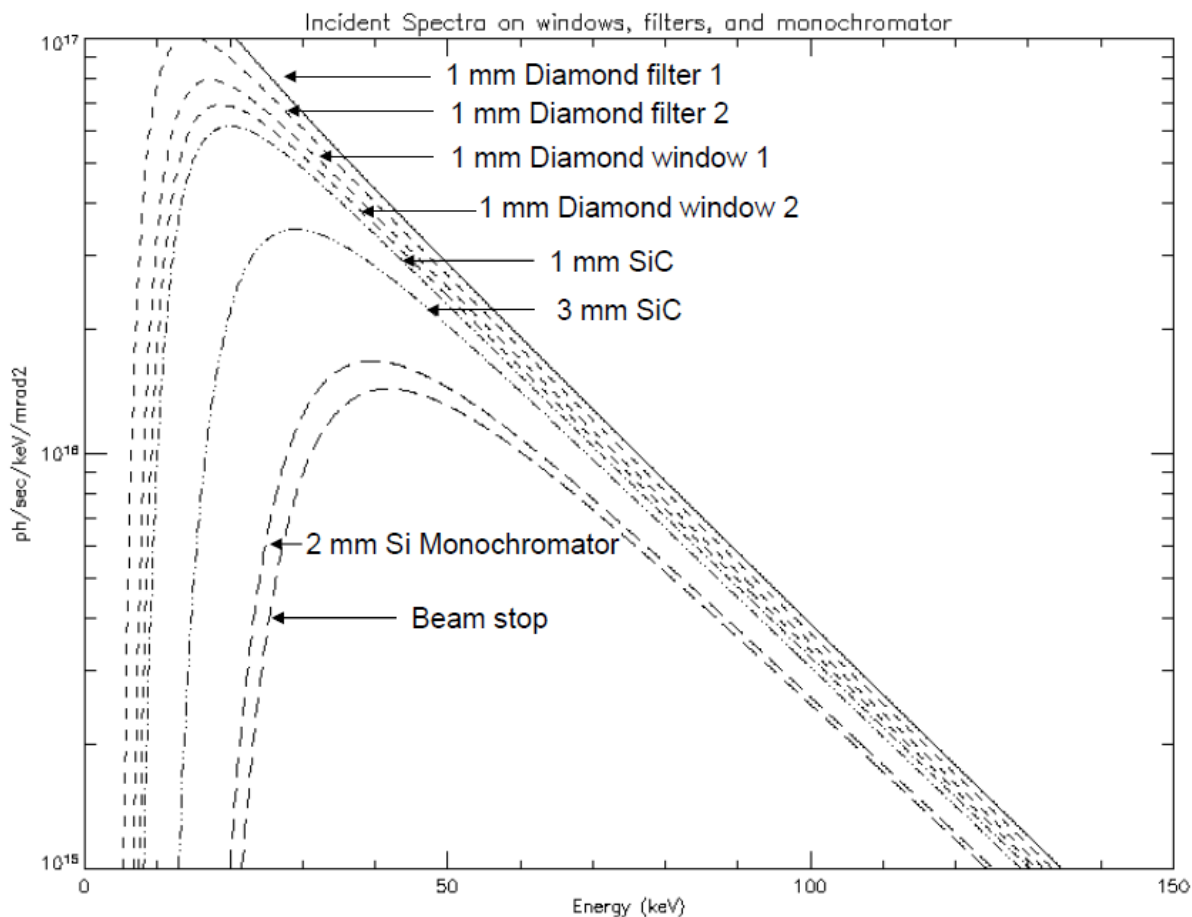


**Fig 3.15:** Simulated incident spectrum incident on wiggler on each window or filtering elements and the monochromator.

Fig. 3.16 shows the simulated absorbed spectrum for each of the four diamond filter/windows and SiC filters, as well as for the monochromator.

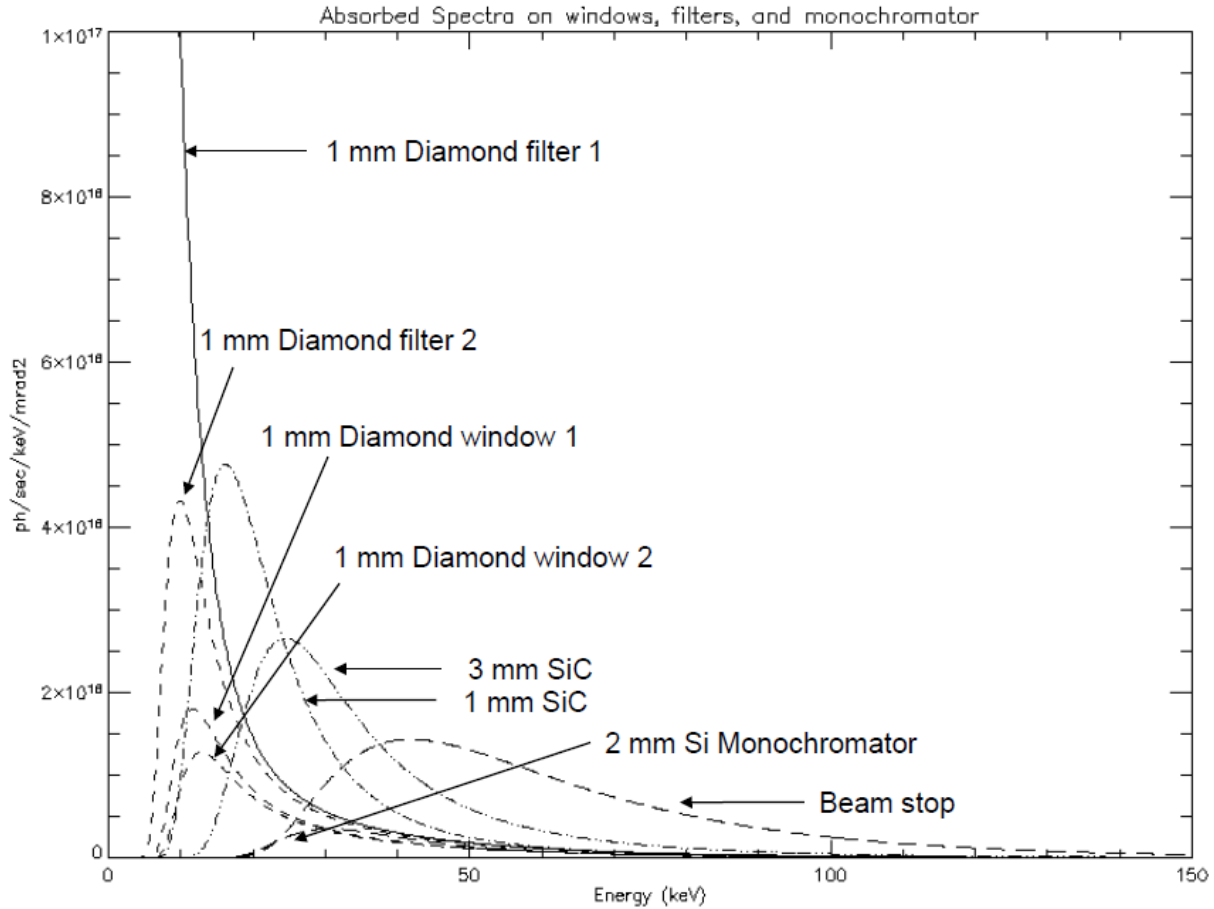


**Fig 3.16:** Simulated absorbed spectrum on each window or filtering elements and the monochromator.

The absorbed power density is then calculated using the data shown in Fig 3.14. Table 3.6 shows results of power load simulation.

	Material	Thickness Along Beam (mm)	Incident Power Density (kW/mrad <sup>2</sup> )	Absorbed Power Density (kW/mrad <sup>2</sup> )	Maximum Absorbed Power (W)
Diamond filter 1 *	Diamond	1	25.1	4.25	850
Diamond filter 2	Diamond	1	20.9	2.13	426
Diamond window 1	Diamond	1	18.8	1.29	258
Diamond window 2	Diamond	1	17.5	1.14	228
SiC filter 1 *	SiC	1	16.3	3.64	728
SiC filter 2	SiC	3	12.7	4.45	890
Monochromator *	Si	2	8.25	1.62	324
Beam stop	Cu	n/a	6.63	6.63	1326

**Table 3.6 :** Results of the power simulation. FEA will be performed for components denoted by \* to assure survivability.

As seen in the table above, of the four diamond filters, diamond filter 1 has the worst-case heat load at  $4.25 \text{ kW/mrad}^2$ . The power load on the diamond window is approximately one-third that of the diamond filter. FEA simulations have been performed for the first diamond filter based on the simulated power load with mechanical and cooling models of filters from XPD filter design. The results in Fig. 3.17a show that the maximum temperature is  $200^\circ\text{C}$ . The SiC filters, 1 mm and 3 mm in thickness, respectively, absorb similar power load. Thus, the 1 mm thick SiC is expected to be the most challenging SiC filter. FEA simulations have been performed for the 1-mm SiC filter (Fig. 3.17b) resulting in a maximum temperature of  $810^\circ\text{C}$ .

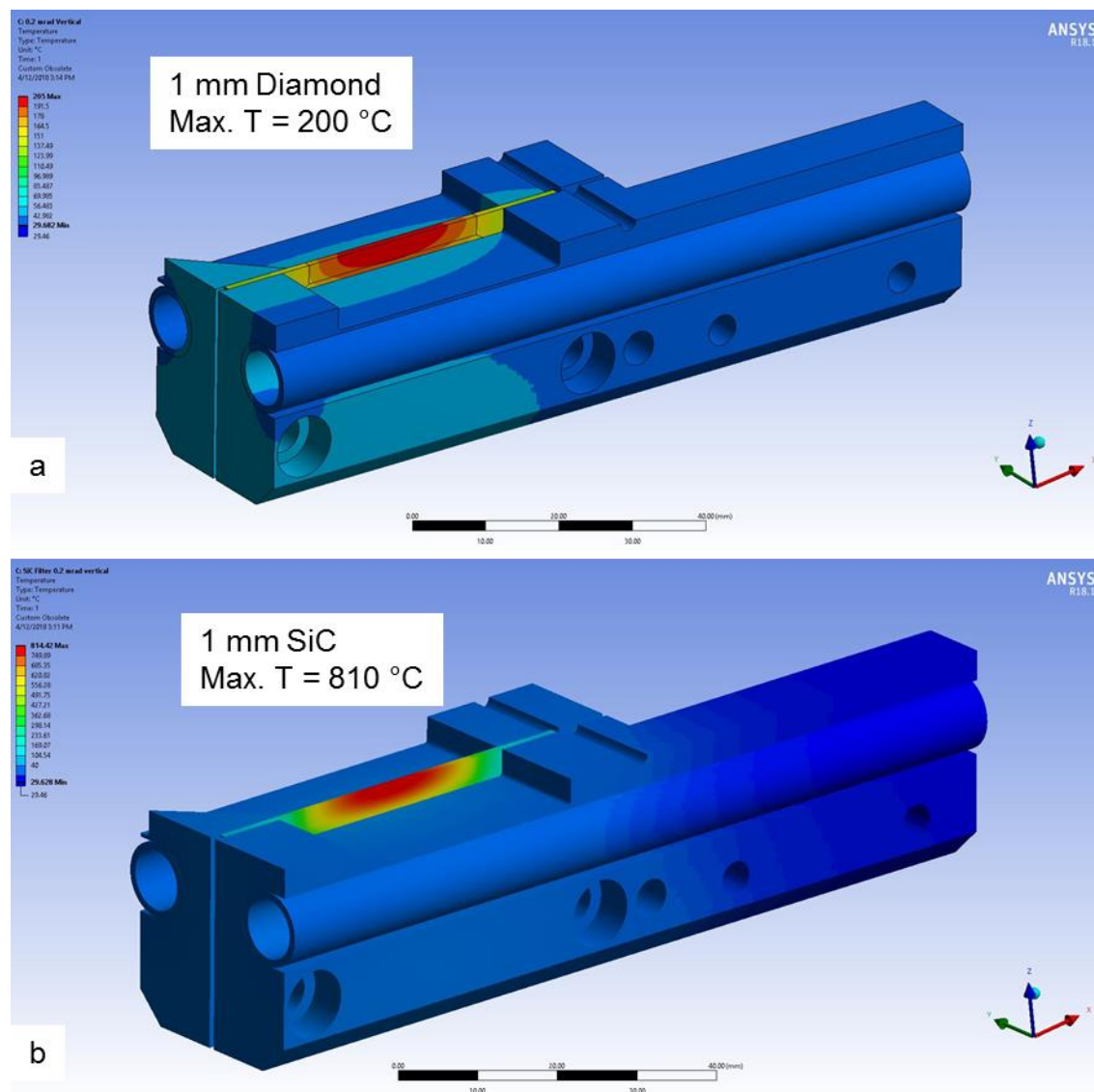


**Fig 3.17:** FEA result of 1<sup>st</sup> diamond filter and 1 mm SiC filter

The preliminary design, shown in Fig. 3.14, has been optimized based on the simulation results. Based on experience at the XPD, we are confident that the design assures survivability of the filters and the monochromator and windows downstream that these filters are designed to protect.

## White-Beam Slit

A four-jaw white-beam slit is located upstream of the imaging monochromator to allow tailoring of the beam size and power on the monochromator. Since the slit is downstream of the fixed windows and filters, the power density is  $8.25 \text{ kW/mrad}^2$ . This corresponds to a power density of  $4.8 \text{ W/mm}^2$ . Preliminary FEA shows that normal incidence of the full HEX center fan on a water-cooled copper block with a power density of  $4.8 \text{ W/mm}^2$  is acceptable.

## White Beam Stops

Three white-beam stops, one for each of the beamlets, will be in the FOE. Of the three, the white-beam stops for the side branch and white-beam branch beams will be tapered to handle the heat load assuming that the filters do not exist. These two will be PPS interlocked. Fig.3.17 shows the design of the beam stops. For the center branch, the white-beam stop is removable and is not PPS interlocked.

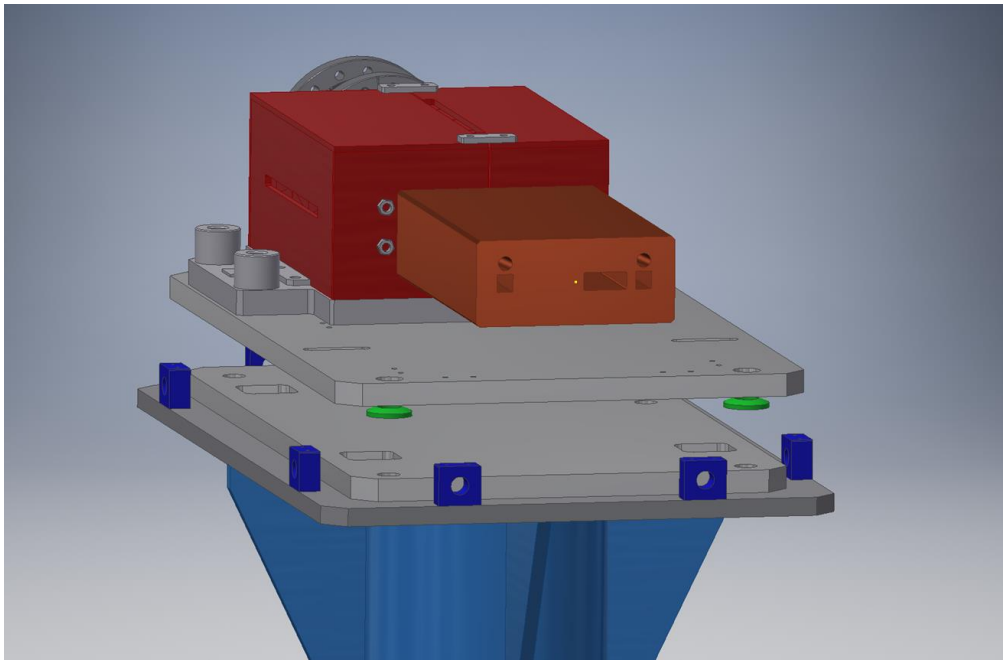


**Fig 3.17:** Design of the white-beam stops.

## 3.4 Radiation Shielding

### First Optical Enclosure

The First Optical Enclosure (FOE) is designed to be white beam compatible and be able to shield from the Gas Bremsstrahlung (GB) radiation generated in the front end straight section. The

13-April-2018

specifications for the first optics enclosure in the NSLS-II guidelines, “NSLS-II Guidelines for Beamline Shielding,” was followed for the FOE design and lead thickness specification.

Calculations have been performed on the lead thickness requirements for sidewalls, roofs, and downstream walls of FOEs and experimental stations for a variety of standard sources; these are documented in “Guidelines for NSLS-II Beamlines and Front End Radiation Shielding Design,” LT-ESHDES-08-003-Rev 001, summarized in the table below.

Source	FOE Shielding*	Endstation Shielding*
IVU	18 / 6 / 50 Pb	6 / 3 / 6 Fe
EPU	18 / 5 / 50 Pb	6 / 3 / 6 Fe
DW	18 / 10 / 50 Pb	4 / 3 / 4 Pb
BM	3 Fe / 3 Fe / 30 Pb	2 / 2 / 2 Fe
TPW	5 / 4 / 30 Pb	3 / 2 / 3 Fe
<b>SCW</b>	<b>18 / 10 / 50 Pb</b>	<b>4 / 3 / 4 Pb</b>

**Table 3.7:** NSLS-II guidance for hutch shielding. \* the shielding recommended is for sidewalls / roof / downstream wall, in mm.

Note that the above guidance for endstation shielding applies only to monochromatic beam hutch B. Subject to verification by radiation calculations, the HEX FOE and white-beam hutches will be designed with 18 mm-thick lead for the lateral and upstream panels, 50 mm-thick lead for the downstream panel, and 10 mm-thick lead for the roof. We will consider using thicker than 50 mm for the downstream panel to minimize the need for secondary Bremsstrahlung shielding in the white-beam experimental enclosures.

Access to the roofs of the FOE is via the roof of the storage ring tunnel. Rails are designed to allow personnel access to the roof. Equipment racks for vacuum instrumentation and FOE-related motion control will be placed on the FOE roof.

### Secondary Bremsstrahlung radiation shielding

The secondary Bremsstrahlung shields are designed according to the NSLS-II shielding guidelines. The main scatterers are masks, monochromator crystals, and beam stops in the FOE, and slits and sample in the white-beam compatible experimental hutches. A preliminary SGB design will be proposed using ray-tracing of 2, 4, and 8 degree angles from the straight centerline. An NSLS-II radiation physicist will then verify the effectiveness of the proposed secondary Bremsstrahlung shields and shielded beampipes via Monte-Carlo simulation using FLUKA code. The simulation results will be used to guide the final design for secondary Bremsstrahlung shields.

### White Beam Transport Pipe

The transport pipes from the FOE to the experimental hutches will be shielded with 7 mm thick lead according to the requirements for white beam. The pink beam transport pipe will be sized so that no synchrotron rays can hit the transport pipe, and that white beam is greater than 25 mm from the inside all of the transport pipe according to the NSLS-II shielding policy.

## Hutches Specification

The FOE, SOE, and two experimental hutches are designed to be white beam compatible. Thus they are lead-shielded for white beam and Bremsstrahlung scatter. The specifications for the first optics enclosure in the NSLS-II guidelines “NSLS-II Guidelines for Beamline Shielding” will be used for all white-beam HEX hutches. Due to the larger distance from the source for the experimental enclosures compared to that of FOE, the shielding thickness may be less than that required by the FOE. Preliminary shielding analysis has been performed using FLUKA code to specify the concrete thickness for hutches F.

For the satellite building, the simulations determine

1. Is the proposed concrete hutch thickness large enough
2. If so, also determine the minimum required thickness

The following assumptions are made for the simulation:

1. Wiggler is SCW70 as specified in the HEX CDR, pages 26-29. To be conservative, we assume the magnetic field to be 4.5T instead of the nominal value of 4.3T.
2. We use the following typical assumptions for storage ring: Electron Energy: 3 GeV, Stored Beam Current : 500 mA. GB Power: 17  $\mu$ W (1 ntorr gas pressure and 15.5 m straight section). The pressure of 1 ntorr is conservative due to the bore-tube of the SCW70 acting as cryo-pump.
3. The divergence of the synchrotron beam entering the hutch is 0.2 mrad vertical x 1.0 mrad horizontal. This is defined by the fixed mask in the front-end. This results in a solid angle of 0.2  $\text{mrad}^2$  for the purpose of calculating the maximum synchrotron flux that is allowed into hutch F.
4. The divergence of the Bremsstrahlung beam entering the hutch will be slightly larger than that of the synchrotron beam. To be conservative, we consider adding 0.1 mrad on top and bottom edges, and 0.25 mrad on each side as being reasonable and conservative. This results in a maximum assumed Bremsstrahlung fan of 0.4 mrad vertical x 1.5 mrad horizontal.
5. Assume a Lead Bremsstrahlung stop at the end of the F hutch, within 1 m of the downstream hutch wall. The size of the Bremsstrahlung stop is large enough to capture the assumed Bremsstrahlung fan of 0.4 mrad vertical x 1.5 mrad horizontal plus required clearance.
6. Worst-case scatter materials are assumed to be Copper (as model for masks and slits) and Silicon (as model for mirrors). The scattering points at 1 m away from the end of the hutch, and 1 m from the beginning of the hutch are considered worst-case scenarios.
7. For the simulation, we will consider the roof of the hutch un-occupied. The external roof of the building should be considered occasionally occupied by people with no GERT training.
8. If necessary, Lead can be considered for the downstream wall of the hutch.

GB Total Ambient Dose rates (mrem/h)  
Target: Cu (2cm dia, 5 cm long)

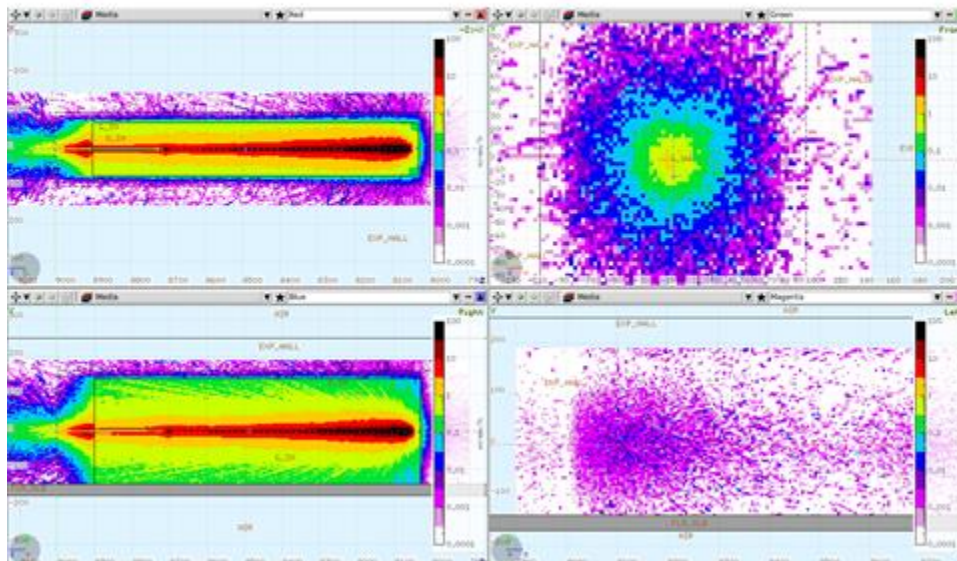


**Fig. 3.13** Results of preliminary Bremsstrahlung shielding simulation.

Fig. 3.13 shows the results of preliminary Bremsstrahlung shielding simulation, using FLUKA code, for the experimental enclosure F. Using the NSLS-II shielding criteria of 0.05 mrem/hr, the downstream wall needs additional lead shielding, of about 50 mm thick covering an area of 1m by 1m, around the beam center. Preliminary results show that the front wall, side walls, and roof of the satellite building F are adequately shielded.

Similar simulations will be performed for the lead experimental enclosures on the experimental floor. Currently, we expect the lead thickness to be 18 mm for the front and side walls, 10 mm for the roof and 50 mm for the downstream wall to be conservative due to the enclosures receiving smaller fan than the FOE. Effect of not being able to use secondary Bremsstrahlung shielding will be analyzed.



## 4. OPTICS

Fig. 4.1 shows the preliminary layout of the HEX optics in the horizontal view. The design of HEX optics includes the one-bounce monochromator for the side branch, the center-branch imaging monochromator, and a sagittal focusing monochromator for the middle branch. The reason for placing the side-bounce monochromator at the upstream end of the optics is that the inbound white beam can be stopped immediately after the side-bounce monochromator, thereby greatly easing the design of the focusing monochromator and mirrors downstream. The monochromatic beam from the side-bounce monochromator crosses the white beams of the center branch and outboard white-beam branch. There is a mirror chamber, hosting two vertically-focusing mirrors, downstream of the sagittal-focusing monochromator.

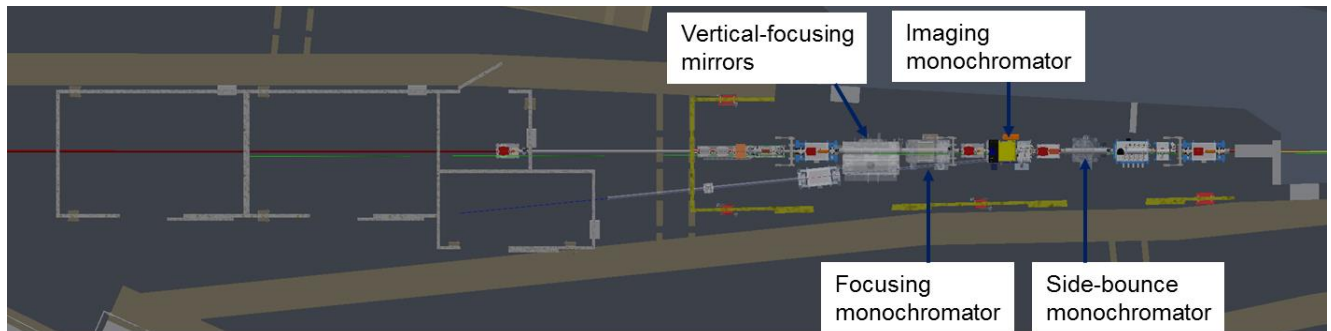


**Fig 4.1:** Preliminary layout of the HEX optics in the horizontal plane.

Two bent-Laue monochromators will serve the center branch: meridionally bent for imaging with large fan beam in the F experimental enclosure, and sagittal-focusing Laue monochromator for ADXD with focused beam in the E enclosure. Since the center branch is white-beam compatible, we will use a small offset of 25 mm to allow compact design and facilitate beam stability. The sagittal-focusing monochromator was invented at the NSLS, and is a proven design, having been used successfully over the past decade at the X17B1, C, X7B beamlines at the NSLS, the XPD beamline at the NSLS-II, and the high-energy beam line at CHESS.

The imaging monochromator will use meridionally bent asymmetric crystals. This is also proven design used at JEEP beamline at the Diamond Light Source, the Imaging Beamline at the Australian Light Source, and the BMIT facility at the Canadian Light Source. Water-cooled slits are upstream of the imaging monochromator.

The sagittal-focused beam for the center branch will be vertically focused by a vertical-focusing mirror with approximately 1 mrad incident angle. Fig. 4.2 shows the preliminary layout of the optics for the center branch in the lateral view, showing the monochromatic beams with 25 mm vertical offset in the upward direction, and the mirror bouncing the beam in the downward direction. This minimizes the distance between the three beams (white beam, imaging monochromatic beam, and focused monochromatic beam) allowing for a single large aperture white-beam shutter at the downstream end of the FOE to control the three beams. A similar shutter at the end of E experimental enclosure controls the three beams in the F enclosure.



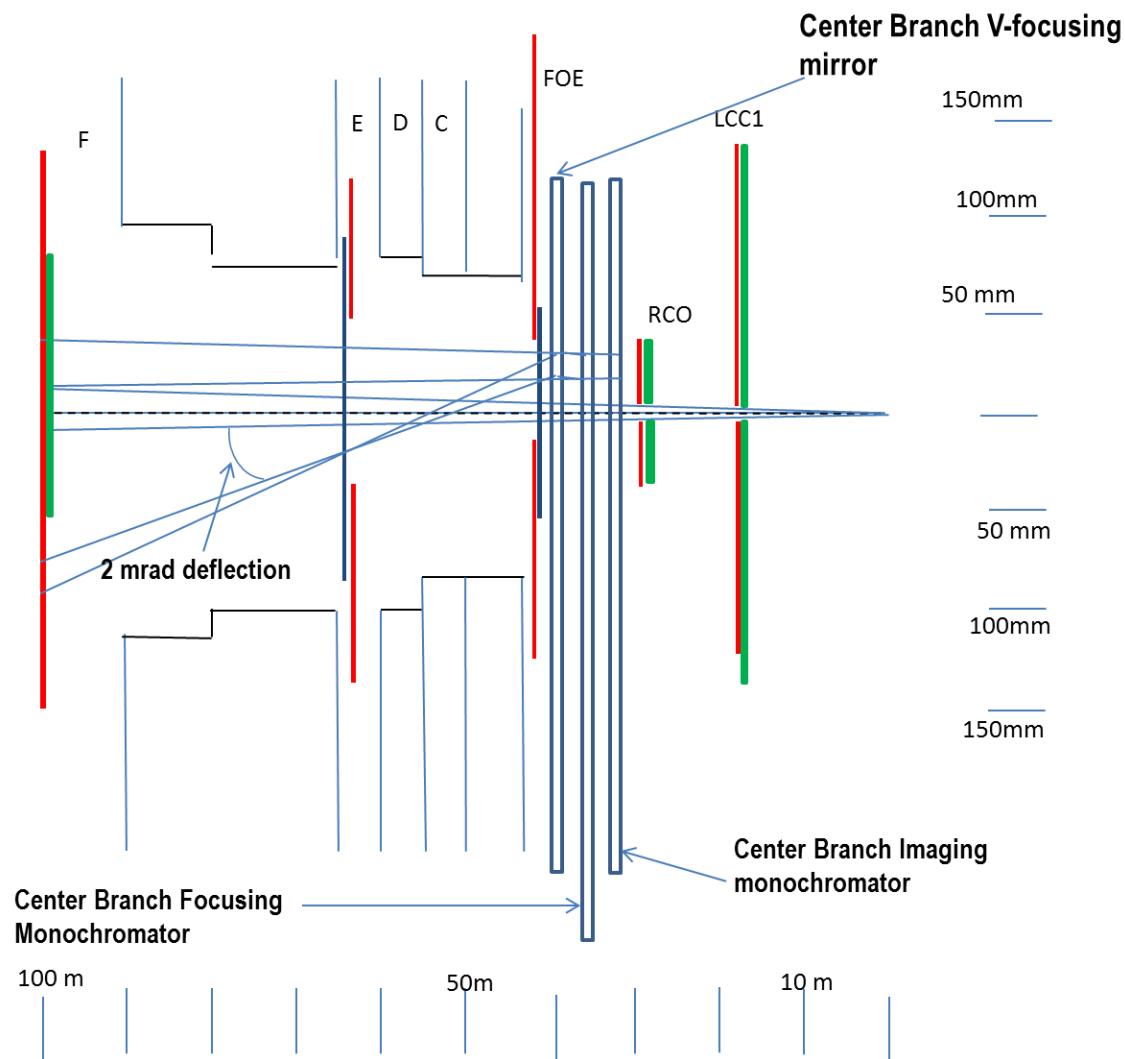


**Fig 4.2:** Lateral view of the center branch optics.

We note that only the imaging monochromator is in the current scope of the project. However, the design of the beamline (FOE layout, beam transport, hutches) accommodates future addition of a focusing monochromator, and future utilization of the outboard white beam branch. Table 4.1 summarize the optics being considered. The red-colored optics are not in the current scope.

	Side branch	Center Branch	White-beam Branch
Monochromator	One-bounce bent-Laue	Sagittal focusing mono Imaging mono	N/A
Mirror	Vertical-focusing	Vertical-focusing	N/A
Mode	Monochromatic	White/Monochromatic	White

**Table 4.1:** Summary of the HEX beamline optics. Red-colored optics are not in the current scope.

## 4.1 Center Branch Imaging Monochromator

HEX will be designed with a new high-energy non-focusing x-ray monochromator for full-field imaging. The design/construction/installation/commissioning of the imaging monochromator is in the current scope. Here we describe the preliminary design and specification of the imaging monochromator. Further design refinement and engineering design and design review of the imaging monochromator will be required before commencement of procurement.

High-energy x-rays are especially suitable for imaging batteries, engineering materials, and earth science samples. Simulations show that bent-Laue crystal monochromator can be used at HEX to provide high-energy x-rays at a flux on the order of  $10^{11}$  ph/s/mm<sup>2</sup>. It will allow EDXD (high spatial resolution and depth resolution, low angular resolution) and imaging on the same sample, greatly enhancing the HEX scientific programs. In the absence of the focusing monochromator, when the monochromatic beam size is reduced by slits, the non-focused beam can be used for ADXD.

Fig.4.3 shows schematically the design of the imaging monochromator, consisting of two identical bent crystals with the first crystal being water-cooled. Both crystals have pitch and roll angular adjustment and the second crystal can be translated along the white-beam direction to allow for energy change while maintaining a fixed exit beam height.

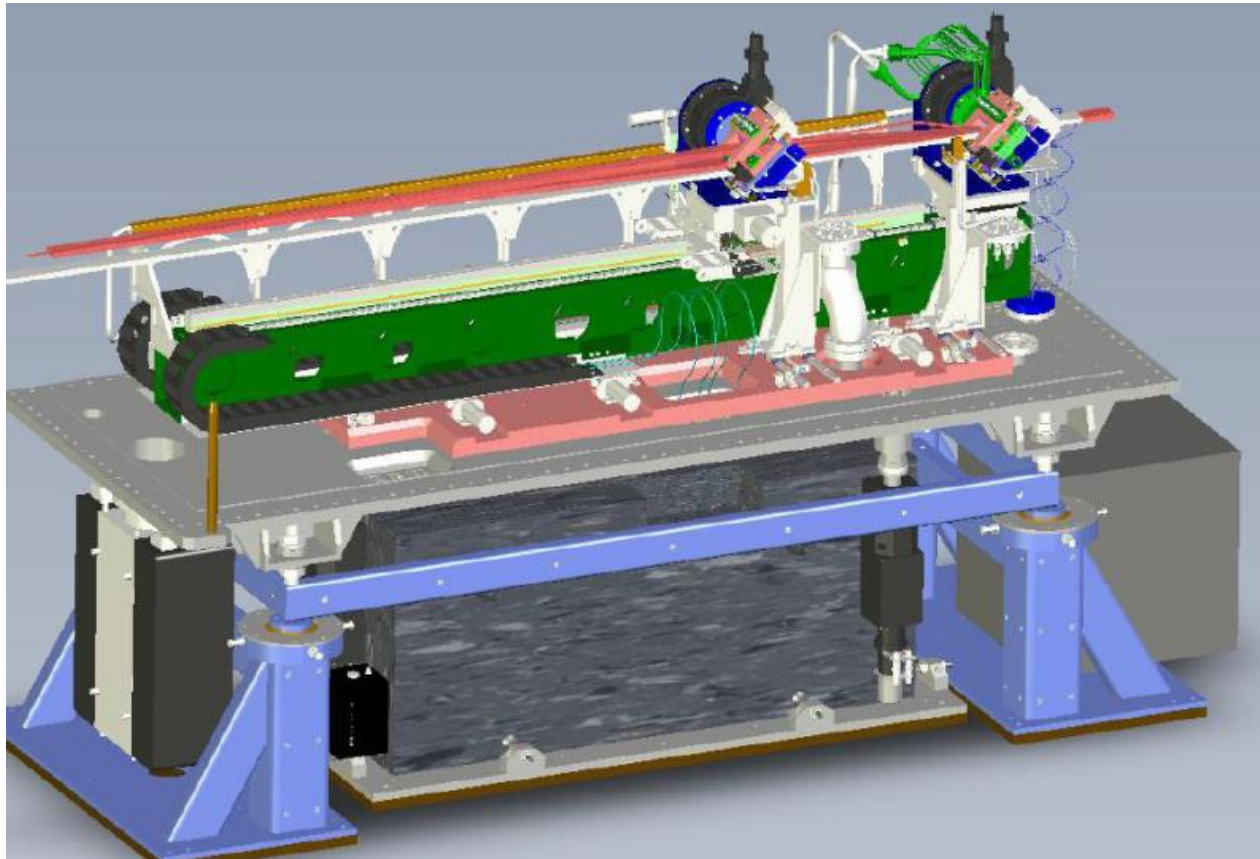


**Fig 4.3:** Preliminary design of the imaging monochromator for HEX will be similar to the imaging monochromator currently in use at the BMIT beamline at the Canadian Light Source.

## Design Ideas and Goal

The following design ideas apply to the imaging monochromator:

1. The HEX center branch is white-beam compatible. Thus, a small offset of 25 mm is chosen to minimize the distance between the two crystals and between the monochromatic and white beam heights. This affords compact design and higher stability.
2. The XPD monochromator has the second crystal/bender in the air. We will also consider this option.
3. The monochromator and beam stop must be removable and EPS interlocked to allow white-beam operation. We will propose a design that allows both to move together to simplify the mode change.
4. The vacuum tank needs to accommodate future addition of a one-bounce monochromator on the inboard side. We prefer the monochromator tank to be opened from the side for easy access and alignment.

The monochromator is located in the FOE with the following parameters: source to monochromator distance ( $f_1$ ) is 31 m; Monochromator to sample distance ( $f_2$ ) is 73 m. The design goal is to provide a large (100 mm x 20 mm) field of view at the G station in the satellite building. We will design the monochromator to cover adjustable x-ray energy range of 30 to 150 keV. It is desirable to achieve energy-change without readjusting the bending.

We note that energy resolution is not important for imaging. However, if possible, the monochromator should offer a high-resolution mode, at about  $10^{-3}$  dE/E, allowing it to be used for diffraction in the future.

## Monochromator Design Considerations

Fig.4.4 shows the geometry for a cylindrically bent Laue monochromator. The plane of diffraction is in the plane of the figure. X rays from a point source are diffracted by the lattice planes in the bent crystal and are focused at a virtual focal point.

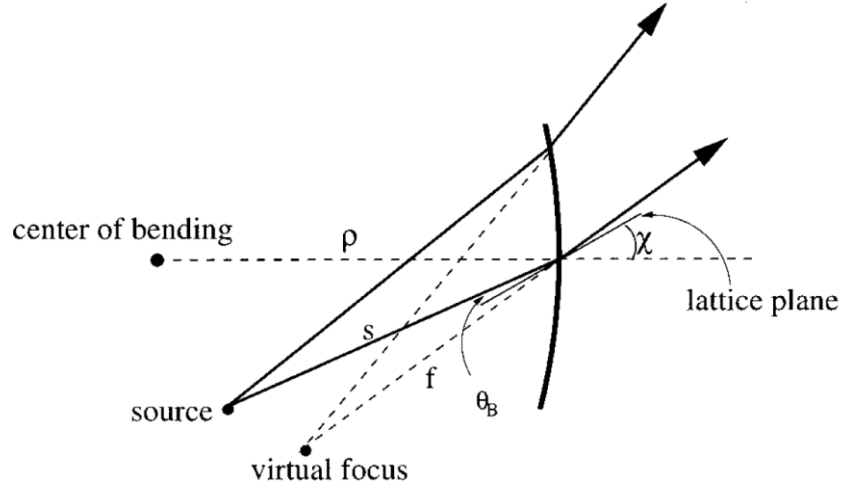


**Fig 4.4.** Geometrical optics considerations for a cylindrically-bent Laue crystal

The asymmetry angle  $\chi$  is defined as the angle between the normal to the crystal's surface and the lattice planes used for reflection of x rays;  $\theta_B$  (the Bragg angle) is the angle required by the Bragg's law,  $\lambda = 2d \sin \theta_B$ , for a given x-ray wavelength  $\lambda$  and crystal lattice spacing  $d$ . The distance between the source and the center of the crystal is  $s$  and the distance between the virtual focus and the crystal is  $f$  ( $f$  is negative for a virtual focal point, as is the case in Fig. 4.3). Geometrical considerations give the following relationship between  $s$  and  $f$ :

$$\frac{2}{\rho} = \frac{\cos(\chi \mp \theta_B)}{s} - \frac{\cos(\chi \pm \theta_B)}{f}$$

where  $\rho$  is the bending radius of the bent crystal.  $\rho$  is positive when the source point is on the concave side of the crystal, as shown in figure above, and negative with the source on the convex side. The upper sign corresponds to when the source and the center of bending are on the same side of the crystal's lattice plane (as shown in figure above). For the lower sign, the source and the center of bending are on different sides of the lattice plane. The upper sign case will be the case for our monochromator.

The variation of the x-ray's angle of incidence  $\theta$  along the crystal surface for a monochromator length  $L$  is

$$\Delta\theta = L/2 \left[ \frac{\cos(\chi - \theta_B)}{s} + \frac{\cos(\chi + \theta_B)}{f} \right]$$

According to the Bragg's law, the diffracted beam energy bandwidth (FWHM) is

$$\frac{\Delta E}{E} = \cot \theta_B \sqrt{\Delta\theta^2 + \omega_0^2 + (\sigma_s/s)^2}$$

where  $\omega_0$  is the angular width of acceptance of the bent crystal diffraction, and  $\sigma_s$  is the size of the x-ray source in the plane of diffraction.

For the special case of zero variation of the angle of incidence along the crystal surface, the diffracted beam will exhibit no energy broadening due to the geometry [i.e., with the highest monochromaticity, and  $\Delta\theta = 0$  in the above equation]. The condition for producing such a beam is

$$s = \rho \cos(\chi - \theta_B) \quad \text{and} \\ f = -\rho \cos(\chi + \theta_B)$$

In this case, commonly referred to as the inverse Cauchois geometry, both the source and the focal point are on the Rowland circle, a circle whose diameter is equal to the bending radius of the crystal. This mode has been used to produce a diverging monochromatic beam.

Both crystals are bent towards the source to minimize energy difference between the top and bottom parts of the beam. Inverse Cauchois geometry, at approximately 40 m bending radius for our first crystal, gives zero energy difference. However, 10-20 m bending radius yields acceptable energy difference, with larger bandwidth and higher intensity.

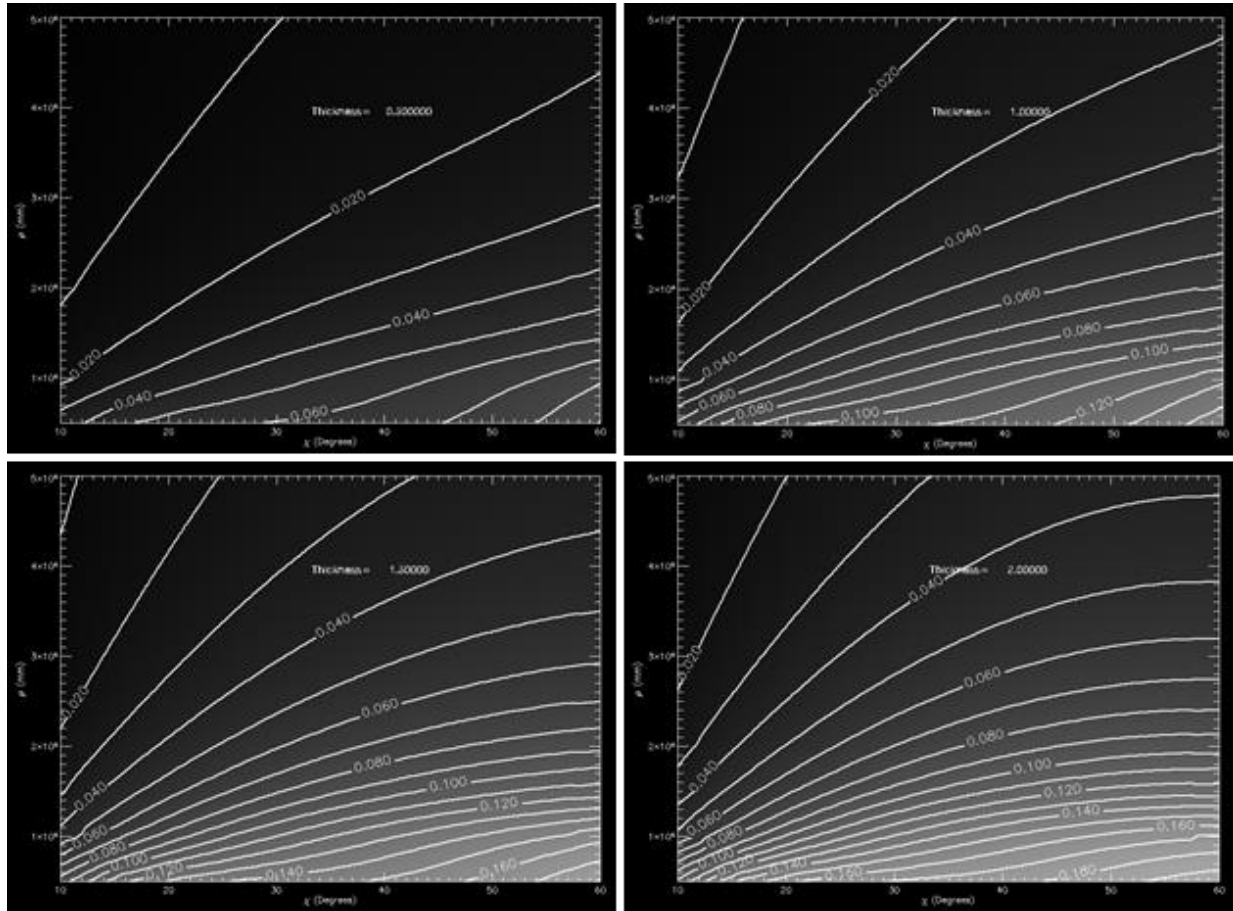
For bent Laue crystals, the bandwidth of the monochromatic beam is proportional to  $\tan(\chi - \theta_B)$ , where  $\chi$  is the asymmetry angle defined as the angle between the diffraction vector and crystal surface.  $\theta_B$  is typically small for high energy x-rays using Si 111 reflection. Thus, asymmetric crystals with asymmetry angle from 10 to 45 degrees are typically chosen to enhance bandwidth.

## Optimization

The monochromator design choice involves a large parameter space that includes asymmetry angle, crystal thickness, and bending radius. The above factors also depend on the desired operating x-ray energy. Generally, larger asymmetry angle results in higher bandwidth and higher flux. However, if the asymmetry angle is too large, the beam footprint on the crystal increases. A thicker crystal results in larger bandwidth and higher flux at high x-ray energy. However, thicker crystals affect performance at low x-ray energy due to the crystal's self-absorption. As mentioned above, a bending radius of approximately 40 m gives best energy resolution, while 10-20 m gives higher flux.

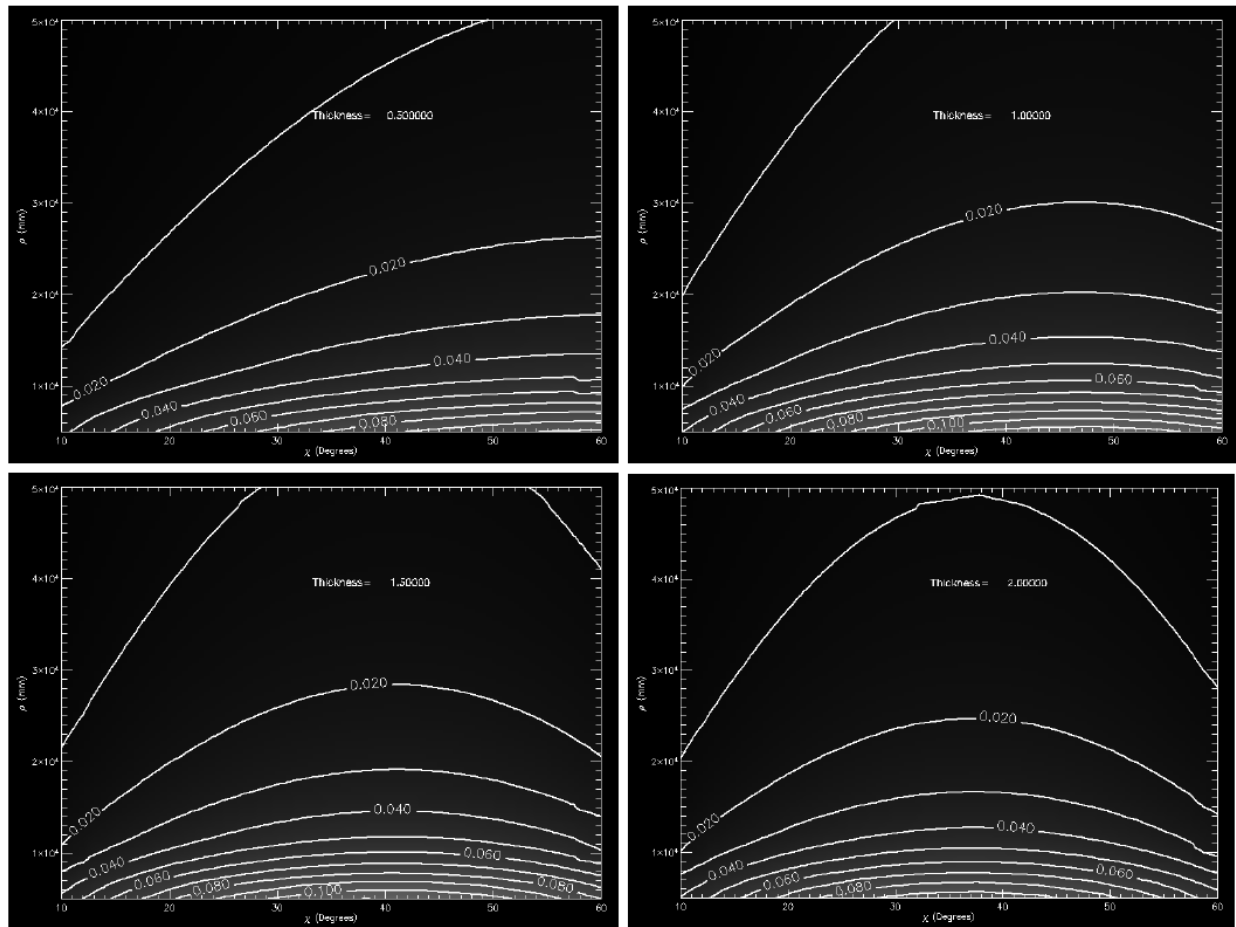
To explore the parameter space to guide an intelligent choice of crystal parameter that suits the unique requirement for imaging at HEX beamline, an IDL program was written, using lamella model for bent-crystals, to explore the parameter space.

Fig. 4.5 shows result of the optimization at 50 keV for various imaging monochromator parameters: asymmetry angle, thickness, and bending radius. The figure of merit (FOM), represented by grayscale in Fig 4.5 (lighter color means higher FOM), is the reflectivity multiplied by the integrated reflectivity in milli-radians. This FOM is proportional to the output flux of the two-crystal monochromator system.



**Fig 4.5:** Result of the optimization at 50 keV for various imaging monochromator parameters: asymmetry angle, thickness, and bending radius.

Similar simulations were performed at 30 and 150 keV to assess the effects of the parameters on the performance across the desired energy range. The results for 30 keV are shown in Fig. 4.6.



**Fig 4.6:** Result of the optimization at 30 keV for various imaging monochromator parameters: asymmetry angle, thickness, and bending radius.

Analysis of optimization results in Figs. 4.5 and 4.6 show that the benefit of larger asymmetry angle levels off after about 40 degrees. Thus the symmetrical crystal cut of 35.3 degrees asymmetry angle, with crystal surface being 100, shown in Fig. 4.7, is an appropriate choice.

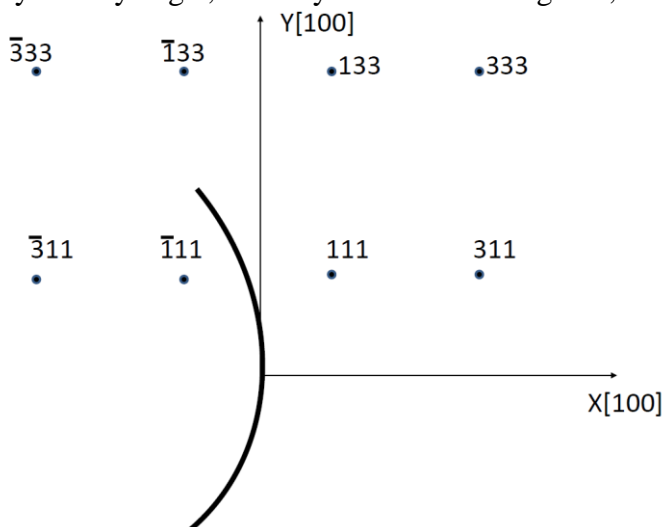


**Fig 4.7:** Reciprocal space configurations of a Laue crystal with surface normal being 100, and the 111 reflection at 35.3 degrees asymmetry angle.

The advantages of a 100 crystal are:

- Simple symmetrical crystal design minimizes confusion. For example, accidental or deliberate flipping the crystal would have no negative consequences.
- 111 reflection at 35.3 degrees asymmetry angle has high flux for imaging and no second harmonics.
- On the same crystal, it is shown in Fig 4.6 that the 022 is a symmetrical reflection with 0 asymmetry angle. At 0-degree asymmetry angle, bending the crystal does not broaden the rocking-curve width. This reflection is a thus good choice for very high resolution, and consequently lower flux, beam.
- The 311 reflection on the same crystal has high resolution and moderate flux, with no second harmonics. This reflection is a good candidate for diffraction studies that require high resolution.

We note that the 022 and 311, both about 30 degrees from nominal 111 position, may not be accessible if we use an InGa-filled trough on top of the crystal for cooling

As for the choice of crystal thickness, the optimization studies show that 1.5- 2 mm allows reasonable 30 keV performance, while thicker crystals benefit higher energies. We choose 2 mm for our baseline design due to the desire to image at 30 keV.

As expected, smaller bending radius results in higher flux at the cost of larger energy difference between the top- and bottom- parts of the beam. The flux benefit levels off at smaller than 10 m radius.

According to the lamellar model, as a result of the systematic change of the angle of lattice plane from the front to the back of the crystal along the beam path, the bent-Laue crystal's rocking curve is typically rectangular in shape. The rocking curve between two identical crystals is the convolution of two rectangles, resulting in a triangular rocking curve. Operating the monochromator with a triangular rocking curve results in the intensity fluctuation as the relative angle between the crystals changes. Since the rocking curve width is proportional to the crystal thickness, if the second crystal is slightly thicker than the first crystal, then the rocking curve would be a trapezoid, resulting in better intensity stability of the monochromatic beam. Thus, we will consider the second crystal having slightly larger thickness than first crystal to achieve a flat-top in the rocking curve. This concept was successfully implemented by the MECT monochromator at X17B beamline of the NSLS.

## Crystal Cooling

Since the micro-imaging program does not require x-rays less energetic than 30 keV, diamond windows and SiC filters can be used for reducing the heat load. We will use four diamond



windows and at least 1 mm of SiC followed by a set of removable SiC filters. The diamond windows serve both as heat filters and as a vacuum barrier while providing added reliability because each is capable of carrying the full power load. The removable SiC filters can be selected to adjust the tradeoff between transmitted power and transmitted flux in real time. The filtering scheme proposed for this beamline closely follows the solution adopted at the JEEP beamline at Diamond Light Source and is similar to the scheme chosen for the XPD beamline at NSLS-II.

One can restrict the horizontal aperture on the monochromator when operating without SiC filter to limit the total power on the monochromator at low x-ray energies. This strategy is consistent with full-field imaging in that samples that use low x-ray energies are typically small samples requiring small field of view. For larger samples that require the full horizontal field of view and accordingly higher x-ray energies, our thermal studies shown in Chapter 3 show that the monochromator can effectively utilize SiC filtering to further reduce heat load and improve thermal stability at higher x-ray energies above 50 keV.

Currently, FEA is being performed to assess the feasibility of water-cooling for the first crystal. If the results allow, water-cooling (instead of liquid nitrogen cooling) will be specified to reduce cost and simplify operations.

## **Monochromator Specifications**

Our optimization study suggests the following parameters for our baseline imaging monochromator design: 35.3 degrees asymmetry angle, approximately 1.8 mm first crystal thickness and 2.2 mm second crystal thickness, 10-50 m bending radius, 25 mm offset between white beam and monochromatic beam,  $\pm 35$  degrees pitch angle range if allowed by the cooling arrangement.

For the motion control specifications, each crystal needs independent adjustments on the inboard and outboard sides of the crystal. The roll and pitch of each crystal should be adjustable. In addition, the second crystal should be able to translate along the white-beam direction to allow for energy change with a fixed beam offset. The modified Boomerang mechanism, pioneered at the NSLS X7B beamline, can be considered to allow one-motion changing of energy.

## **Performance**

The photon flux and energy resolution in the experimental station F were simulated for various bending radii using the baseline crystal specification listed above. Figs.4.8 and 4.9 show the photon flux results for 30 m, and 10 m bending radii, respectively.

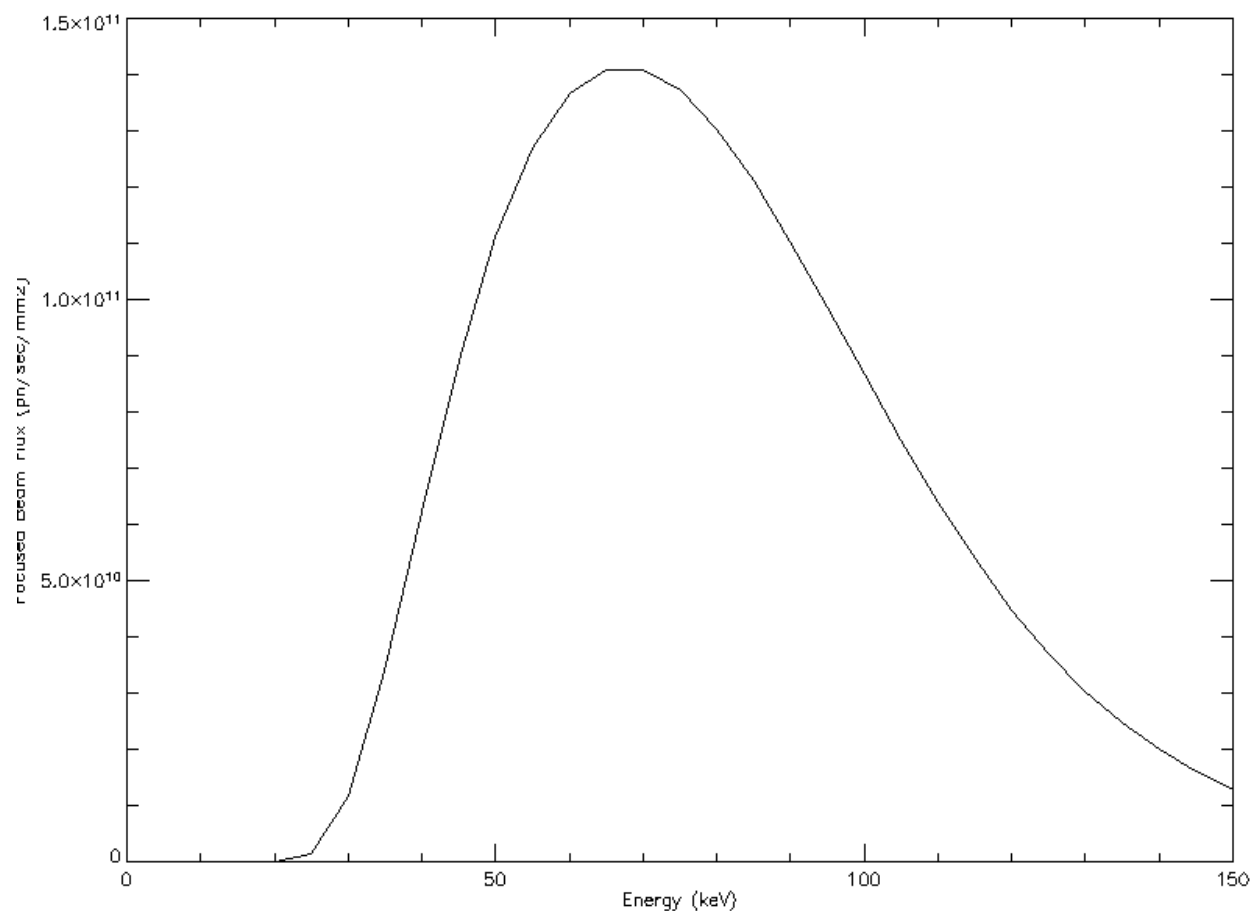


**Fig 4.8:** Performance of the imaging monochromator with 30 m bending radius

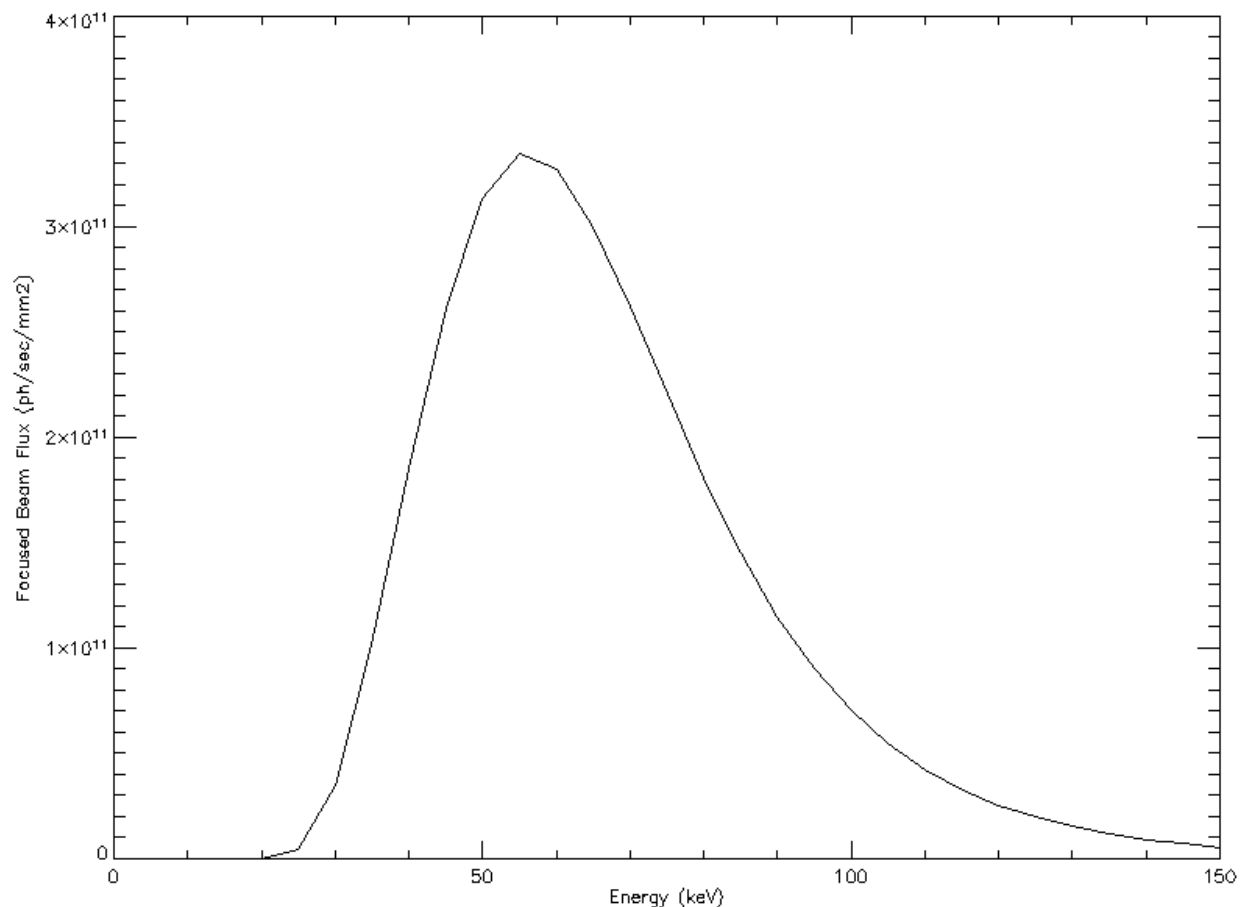


**Fig 4.9:** Performance of the imaging monochromator with 10 m bending radius

### Comparison with similar monochromators

Table 4.2 shows parameters and cooling mechanisms by other facilities for double bent-Laue monochromators, along with that for the proposed HEX imaging monochromator. We note that JEEP and Shanghai monochromators were not designed exclusively for imaging, and thus have larger crystal-thickness of 4 mm, compared to imaging monochromators that use 1-2 mm thickness.

	BMIT (CLS)	JEEP (Diamond)	UHX (Shanghai)	IMBL (Australia)	CAMD	HEX (NSLSII)
Asymmetry angle (deg.)	15	44	45	15	35.3	<b>35.3</b>
Reflection	111 & 220 (either/or)	111	111	111, 311 via rotation	111	<b>111, 220 &amp; 311 via rotation</b>
Thickness (mm)	2.0	4.0	4.0	1.0	0.7	<b>1.8 1<sup>st</sup> crystal 2.2 2<sup>nd</sup> crystal</b>
Offset (mm)		50	50	20	8-25	<b>25</b>
Energy range (keV)	25-150	53-150	45-150	30-100	30-80	<b>30 – 150</b>
Cooling	Water, In-Ga trough	Cryogenic	Cryogenic	Water, In-Ga bath	Water, one-side	<b>Water, one-side</b>
Bender	2 Leaf Springs	2 Leaf Springs	2 Leaf Springs	2 Leaf Springs	2 Leaf Springs	<b>2 leaf springs</b>

**Table 4.2:** Parameters and cooling mechanisms by other facilities for double bent-Laue monochromators, along with that for the proposed HEX imaging monochromator.

## 4.2 Center Branch Focusing Monochromator (Mature Scope)

High-energy x-rays are especially suitable for in-situ powder diffraction and PDF measurements, the bread-and-butter experiment performed at the highly-productive XPD beamline. The idea of sagittal focusing using Laue crystals was originally developed at the NSLS. Simulations show that it can be implemented at HEX to provide the high-energy x-rays at a flux of  $10^{13}$  ph/s. This allows EDXD (high spatial resolution and depth resolution, low angular resolution) and ADXD (high angular resolution, low spatial resolution, no depth-resolution) on the same sample, greatly enhancing the HEX scientific programs.

The center branch of HEX will be designed with a high-energy focusing x-ray monochromator that, together with a vertically focusing mirror, focuses the monochromatic beam in the E experimental enclosure. The building of the focusing monochromator is not in the current scope. We note that the design of the beamline (FOE layout, beam transport, hutches) must

accommodate the future addition of the focusing monochromator. The design effort for the focusing monochromator will be limited to preliminary design. Engineering design and design review of the monochromator design will be required before commencement of procurement/installation in the future, if and when funds become available

### **X-ray Optics Principles of the Focusing Monochromator**

The idea of sagittal focusing using Laue crystals was originally developed at the NSLS a decade ago (Zhong et al. 2001a,b, Zhong et. al. 2002, Zhong et al. 2003). The extent of such focusing is similar to that of sagittal focusing by a Bragg crystal, except for a factor related to the asymmetry angle. The anticlastic bending facilitates the use of inverse-Cauchois geometry in the meridional plane to provide better energy-resolution and to increase the photon flux by an order-of-magnitude compared to traditional sagittal focusing with Bragg crystals. Furthermore, sagittal focusing by a Laue crystal is preferred over a Bragg crystal at x-ray energies above 30 keV because, unlike Bragg crystals, the length of the beam's footprint on a Laue crystal is small and insensitive to energy. The conditions imposed on the asymmetry angle of the Laue crystal to achieve simultaneous sagittal focusing and inverse-Cauchois geometry in the meridional plane were derived by NSLS scientists for both single-crystal and double-crystal fixed-exit sagittal focusing monochromators.

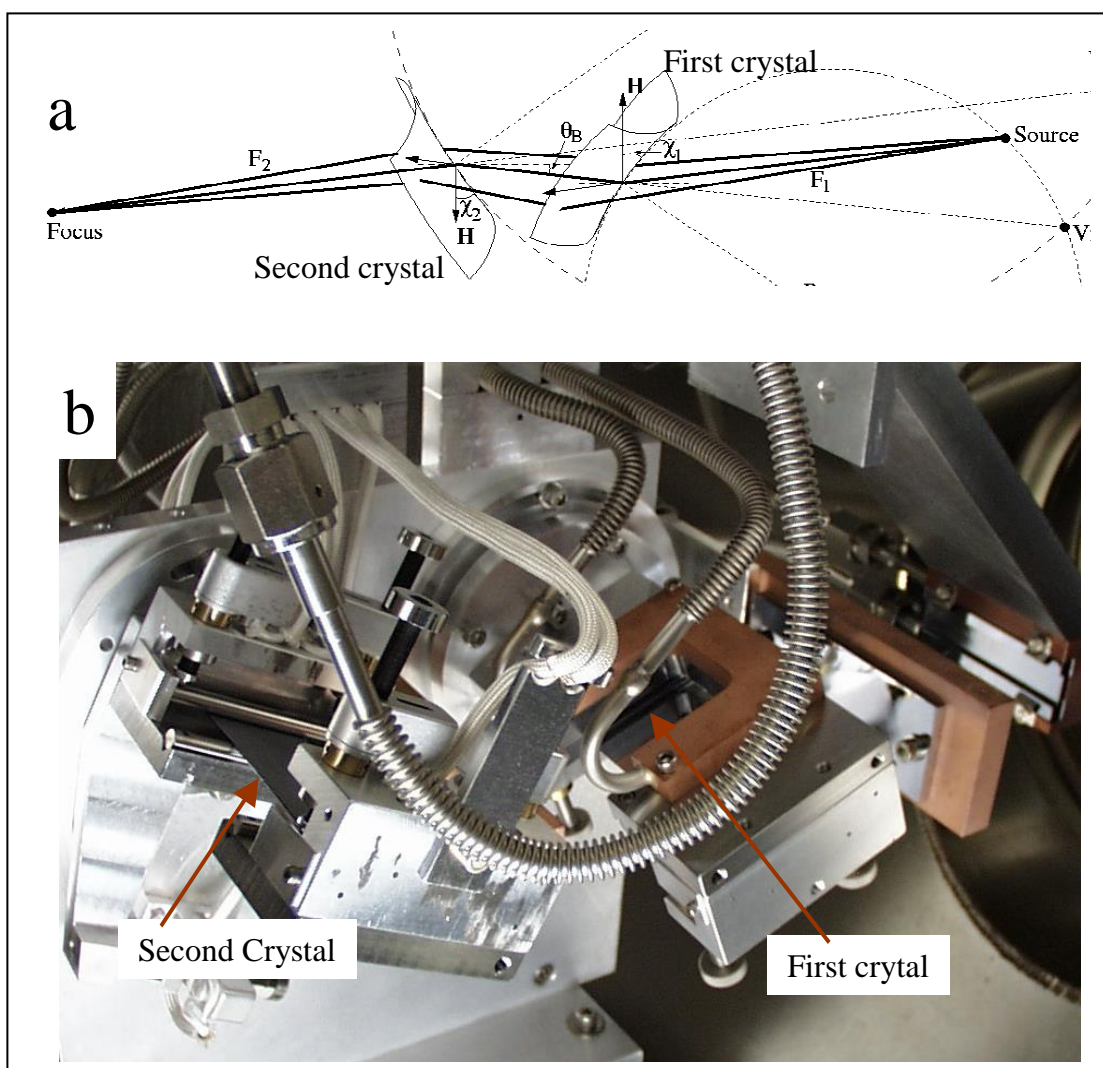


**Figure 4.10.** The mechanism of the sagittal focusing with asymmetric Laue crystals, bending of the crystals causes precession of the diffraction vectors ( $H$ ) around the axis of sagittal bending, and the resulting focusing of the diffracted beams. b) Photograph of a monochromator installed at the NSLS X17B1 beamline.

The use of bent asymmetric Laue crystals to sagittally focus synchrotron x-rays from 15 to 50 keV have been tested at the NSLS X15A, which is a standard NSLS bending magnet line. A four-bar bender, bending a rectangular planar crystal, produced the necessary sagittal- and meridional-bending for this unique application. A double-crystal sagittally focusing monochromator, based on this concept, has been constructed and tested, and was in use at the X17B1 beamline for about 10 years, providing 67 keV x-rays (see figure 4.10). It focuses a horizontal divergence of 3 milli-radians to a horizontal dimension of about 0.4 mm. The x-ray flux-density at the focus was a few hundred times larger than that of unfocused x rays.

The same concept was successfully used at the x-ray powder diffraction (XPD) beamline of the NSLS-II, the X7B beamline of the NSLS, and at InSiTu (F2) beamline at the CHESS facility.

## Design Ideas and Goal

As with the imaging monochromator discussed above, a small offset of 25 mm is chosen to minimize the distance between the two crystals, affording compact design and higher stability. The XPD monochromator has the second crystal and its bender in the air. This design was experimentally proven to be convenient. We will consider this option for the focusing monochromator. As with the imaging monochromator, the focusing monochromator and its beam stop must be removable and EPS- interlocked to allow white-beam operation.

The basic parameters and constraints for the focusing monochromator is listed below:

- Source to monochromator distance ( $f_1$ ): 33.210 m
- Monochromator to sample distance ( $f_2$ ): 25.787 m (E hutch), 70.782 m (F hutch)
- Focal length  $f_0 = 1/(1/f_1 + 1/f_2) = 14.5$  m (E), 22.6 m (G)
- Adjustable x-ray energy 30-100 keV, the design should maximize performance at approximately 65 keV

The goal is to focus the 1 milli-radians horizontal fan to approximately one mm horizontal size in the E experimental hutch. For diffraction, it is desirable to have energy resolution of about  $10^{-3}$  dE/E.

The baseline design is a monochromator similar to that used by XPD, with 0.6 mm thick crystals. We will consider using 4 mm thick SiC filter to control heat load on monochromator. This filtering scheme is expected to reduce the heat-load sufficiently to allow water-cooling instead of cryogenic cooling of the first crystal, thus reducing cost and simplifying operations.

As discussed previously, the modified Boomerang design allows for one-motion changing of energy. This option will be considered for the engineering design.

Fig.4.11 shows the reciprocal space configuration of the Silicon crystal for the proposed sagittal-focusing Laue monochromator. Si 111 and 311 reflections are considered. This design is the same as that of the XPD monochromator at the NSLS-II.

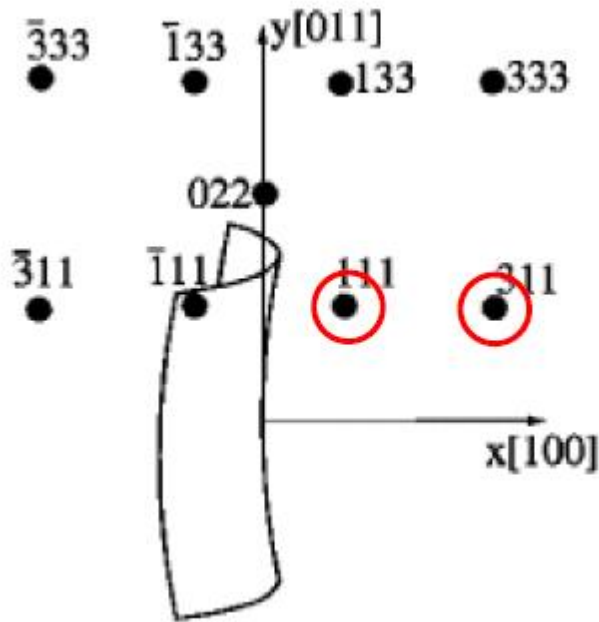


**Figure 4.11:** Reciprocal space configuration of the Silicon crystal for the proposed sagittal-focusing Laue monochromator. The crystal surface normal is the 100 direction. The bending axis points to the 011 direction. Si 111 and 311 reflections are accessible with asymmetry angles of 35.3 and 64.8 degrees, respectively.

### Performance Simulation using 111 reflection

A simulation was performed for the 111 reflection on 100 crystal (the asymmetry angle is 35.3 degrees). The simulation assumes that the monochromator focuses the beam at the center of E experimental enclosure. Both crystals are assumed to be 0.6 mm thick. The distance between the crystals, defined as shift, is calculated assuming a 25 mm offset between the monochromatic beam and the white beam.

Energy (keV)	30	40	50	60	70	80	90	100
Bragg angle (deg)	3.779	2.833	2.266	1.888	1.618	1.416	1.259	1.133
Shift (mm)	188	251	315	378	442	505	469	632
Bending Radius (mm)	2208	1656	1325	1104	947	828	736	662
dE/E ( $\times 10^{-3}$ )	0.47	0.82	1.3	1.9	2.3	3.4	4.3	5.4
Integrated Reflectivity	23	35	46	54	54	49	42	35



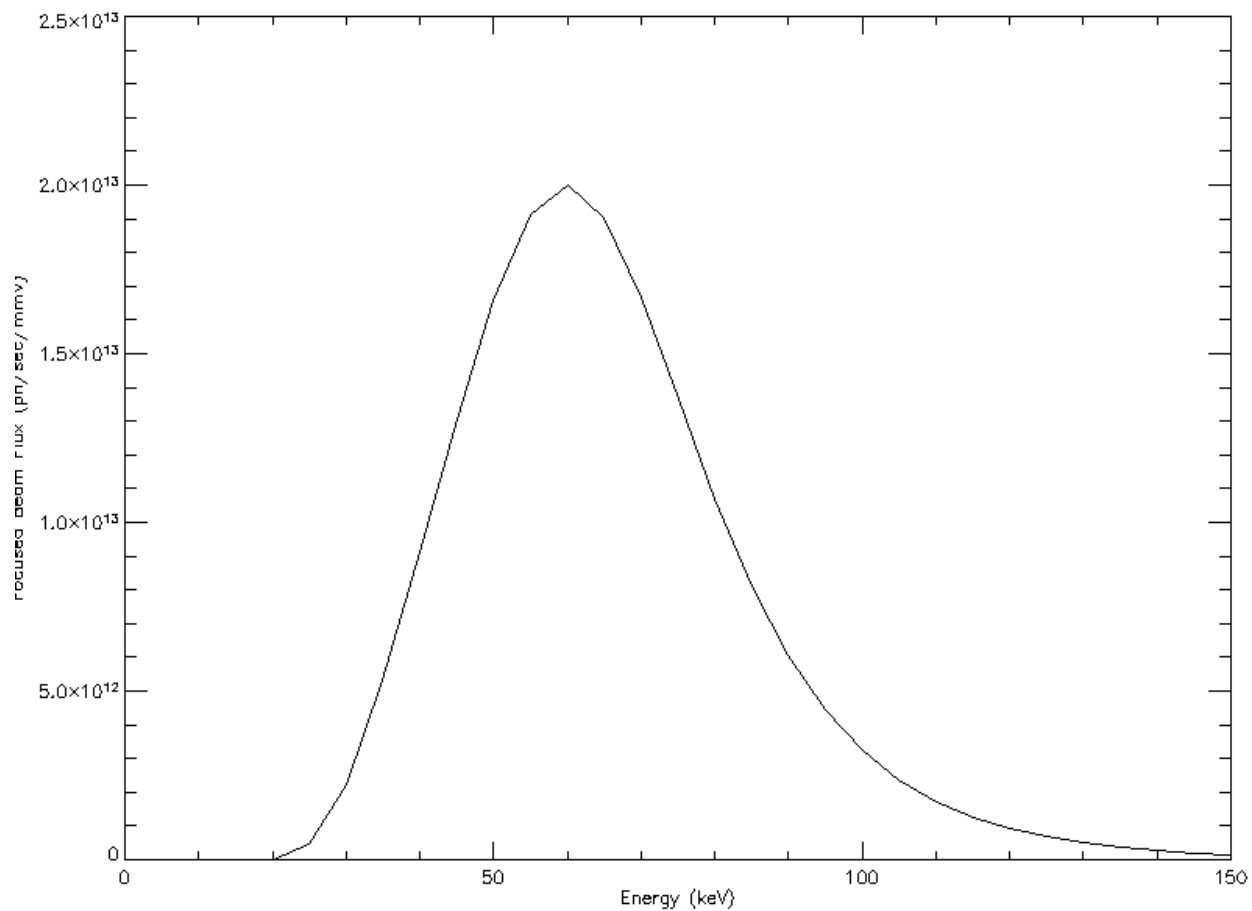
(micro-radians)								
Reflectivity (%)	75	97	92	89	76	60	46	35
Flux at Focal spot ( $10^{12}$ ph/s/vertical mm)	2.2	9.1	16	20	17	11	6.0	3.2

**Table 4.3:** Simulation of shift, sagittal bending radius, energy resolution, crystal reflectivity and integrated reflectivity, and flux at focal spot per 1 mm of vertical beam (assuming that the vertical focusing mirror is not used) as a function of x-ray energy. The simulation assumes using the 111 reflection and that the monochromator focuses 1 mrad of horizontal beam at the center of E experimental station.

It is seen that the 25-mm offset affords a compact monochromator design with a distance of 631 mm between the two crystals for 100 keV x-ray energy. We would like to extend the length to about 1 m to allow for extension of x-ray energies to 150 keV.

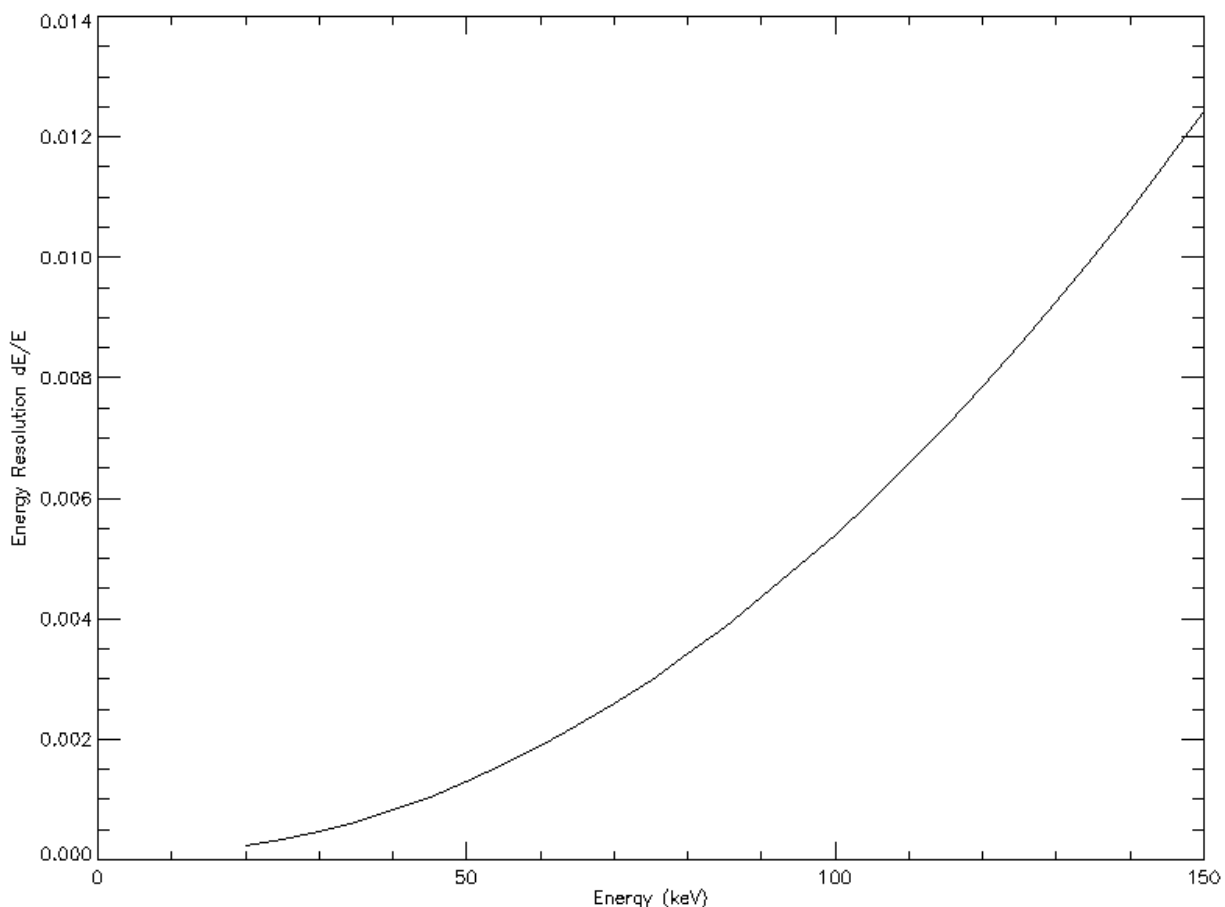
The sagittal bending radius for focusing 100 keV x-rays is 663 mm. This dictates that the crystal thickness should be smaller than 0.63 mm using the rule-of-thumb that the smallest cylindrical bending radius for a Silicon crystal is about 1000 times the crystal's thickness. This is the reason for our choice of 0.6 mm crystal thickness in the base design.

Fig. 4.12 shows the simulated photon flux as a function of x-ray energy for focusing in the E hutch using the 111 reflection.



**Fig 4.12:** Simulated photon flux as a function of x-ray energy for focusing in the E hutch using the 111 reflection.

Fig. 4.13 shows the simulated energy resolution as a function of x-ray energy for focusing in the E hutch using the 111 reflection.



**Fig 4.13:** Simulated energy resolution as a function of x-ray energy for focusing in the E hutch using the 111 reflection.

It is seen from the figure above that the energy resolution at 50 keV exceeds  $10^{-3}$ . This is due to the combination of two effects: a. as the energy increases, the bending radius must be smaller to maintain the same focal point in the E experimental station, resulting in proportionally increased rocking curve width; and b. higher x-ray energy results in smaller Bragg angle. To achieve higher resolution, especially for high x-ray energies, we consider an additional reflection accessible on the same crystal next.

### High-resolution 311 reflection

Fig.4.14 shows the experimental rocking curves for the proposed sagittally bent Laue crystal, bent to 0.7 m radius, at 67 keV x-ray energy. It shows that the 111 reflection offers a good reflectivity and moderate resolution (proportional to rocking curve width, about 150 microradians). Interestingly, the 311 reflection, with asymmetry angle of 64.8 degrees, delivers a higher resolution beam with less flux. The 311 reflections offers higher resolution than 111 for three reasons: its factor-of-three smaller rocking curve width for the same bending radius; it requires larger bending radius than 111 due to larger asymmetry angle, further reducing the

rocking curve width; its factor-of-two larger Bragg angle results in smaller  $dE/E$  for the same rocking curve width. We thus consider using the 311 reflection (asymmetry angle 64.8 degrees) to achieve about an order of magnitude higher resolution beam than 111 reflection. This can be especially useful for high x-ray energies from 50 to 100 keV.

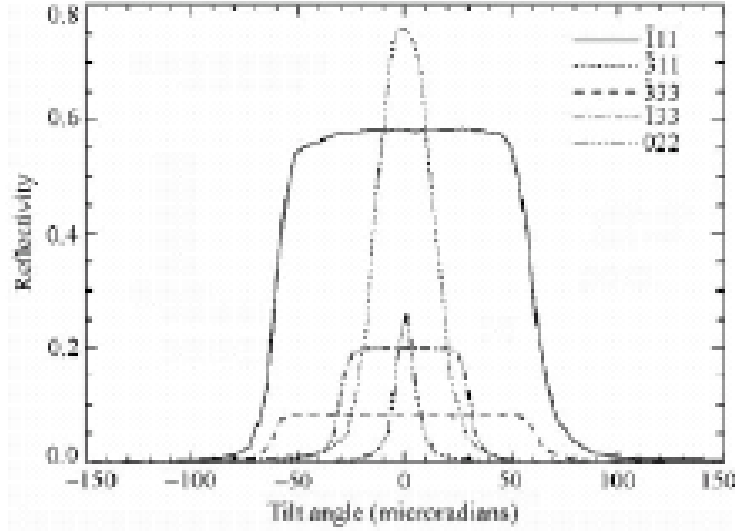


**Fig. 4.14:** Experimental rocking curves, acquired at the NSLS X17B1 beamline, for the proposed sagittally bent Laue crystal, bent to 0.7 m radius, at 67 keV x-ray energy.

A simulation was performed for the case of using the 311 reflection on 100 crystal. As with the 111 reflection, the simulation assumes that the monochromator focuses the beam at the center of E experimental enclosure. Both crystals are assumed to be 0.6 mm thick. A 25 mm offset is assumed between the monochromatic beam and the white beam for calculating the required shift between the crystals.

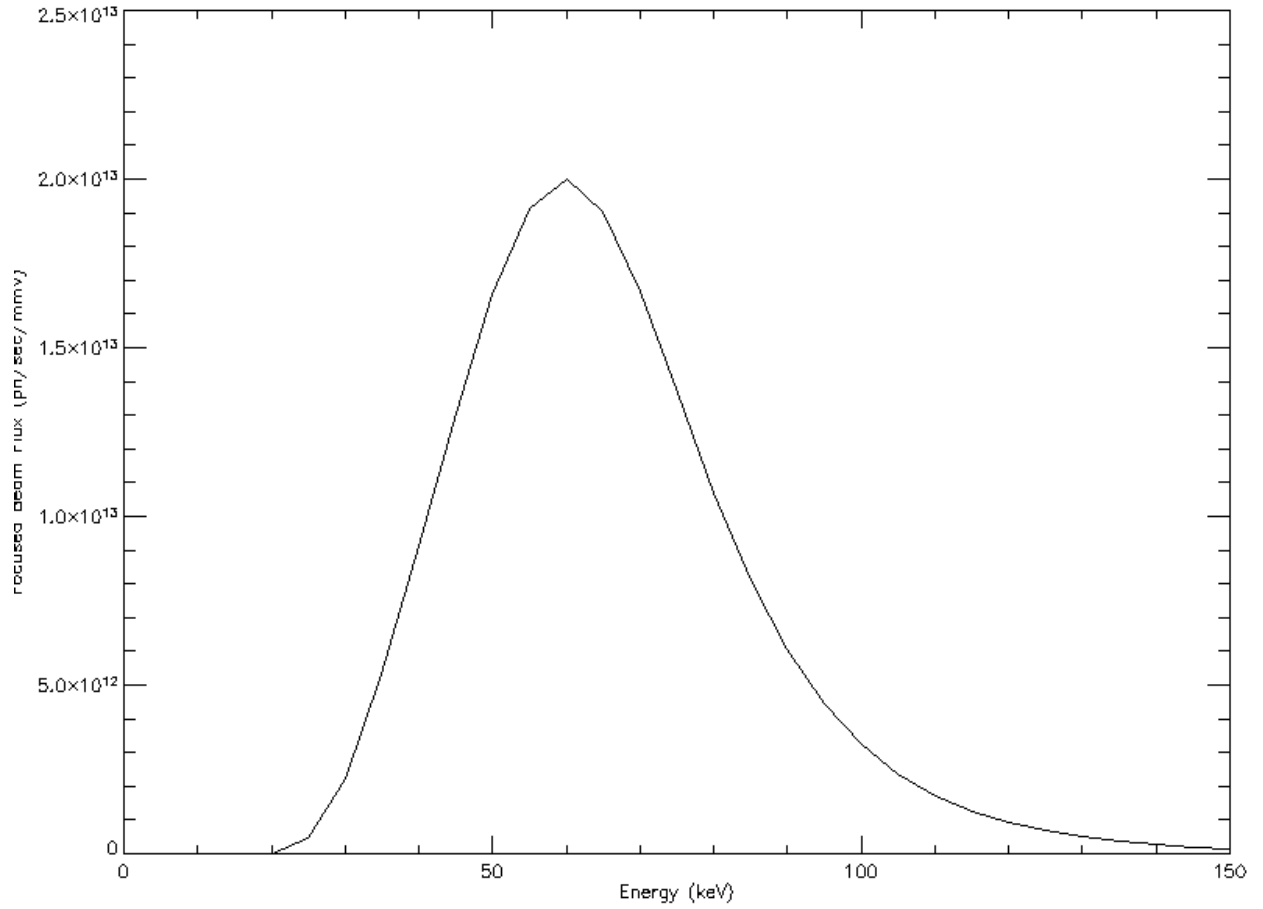
Energy (keV)	30	40	50	60	70	80	90	100
Bragg angle (deg)	7.249	5.431	4.342	3.618	3.100	2.712	2.411	2.170
Shift (mm)	96	130	164	197	230	263	296	329
Bending Radius (mm)	6627	4970	3976	3313	2840	2485	2209	1988
$dE/E$ ( $\times 10^{-4}$ )	0.42	0.34	0.43	0.97	1.5	2.4	3.4	4.6
Integrated Reflectivity	0.40	1.1	1.8	2.5	3.1	3.7	4.3	4.9

(micro-radians)								
Reflectivity (%)	0.11	0.38	0.62	0.76	0.84	0.89	0.91	0.92
Flux at Focal spot ( $10^{11}$ ph/s/vertical mm)	0.31	0.63	2.2	4.1	5.5	6.3	6.5	6.3

**Table 4.4 :** Simulation of shift, sagittal bending radius, energy resolution, crystal reflectivity and integrated reflectivity, and flux at focal spot per 1 mm of vertical beam (assuming that the vertical focusing mirror is not used) as a function of x-ray energy. The simulation assumes using the 311 reflection and that the monochromator focuses 1 mrad of horizontal beam at the center of E experimental station.

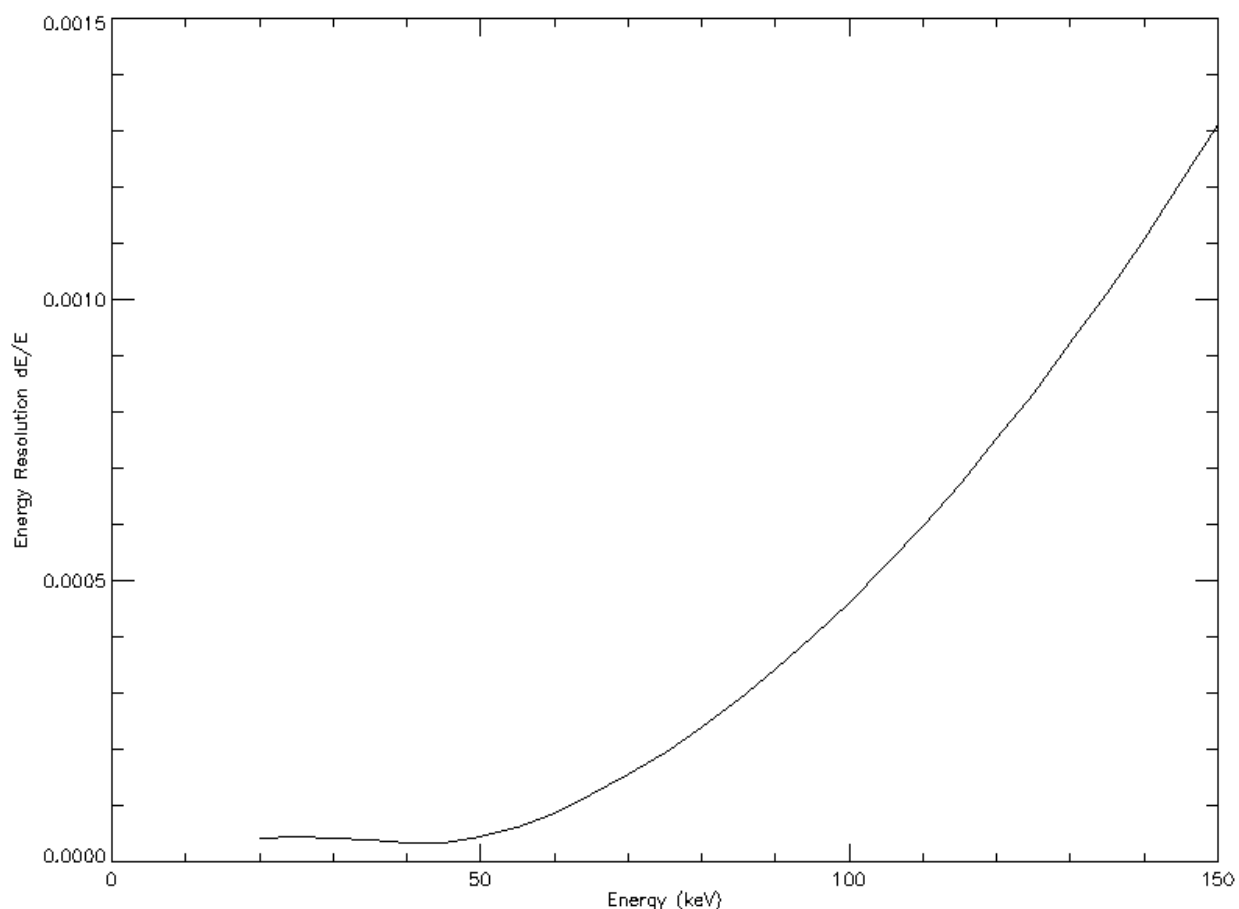
Comparing table 4.3 with 4.4 shows that 311 indeed offers an order of magnitude higher resolution than 111 reflection, at the expense of commensurately smaller flux. We note that the 311 reflection requires a very compact monochromator, with a distance of 96 to 325 mm between the two crystals for tuning the x-ray energy from 30 to 100 keV. Table 4.4 shows that the smallest bending radius is about 2 meters. Thus for a stand-alone device, one can consider using a thicker crystal to offer higher mechanical stability and higher performance at high x-ray energies. As noted before, the current crystal thickness, 0.6 mm, is optimum for the 111 reflection.

Fig. 4.15 shows the simulated photon flux as a function of x-ray energy for focusing in the E hutch using the 311 reflection.



**Fig 4.15:** Simulated photon flux as a function of x-ray energy for focusing in the E hutch using the 311 reflection.

Fig.4.16 shows the simulated energy resolution as a function of x-ray energy for focusing in the E hutch using the 311 reflection.



**Fig 4.16:** simulated energy resolution as a function of x-ray energy for focusing in the E hutch using the 311 reflection.

We note that while the focusing monochromator is similar in design to that at XPD, the 311 reflection, which is not feasible at XPD due to its cooling design, is important for HEX that desires to achieve x-ray energies of 100 keV and above. Thus, we would focus on making the 311 reflection accessible for the engineering design in the future. We believe that by using simpler water-cooling, as opposed to XPD's cryogenic cooling, it would be feasible to rotate the first crystal by about 25 degrees to access both the 111 and 311 reflections.

### 4.3 Side Branch Monochromator (Out of Base Scope)

The side branch monochromator will be a single-bounce (horizontal) bent Laue crystal. The monochromator uses the same two-theta angle, 5.8 degrees, as that used at the PDF beamline of the NSLS-II. PDF will be commissioned in 2018. As such, we will study the performance of the PDF beamline after it becomes operational in 2018. If all is satisfactory, we plan to copy the same design for the HEX side branch monochromator.

Table 4.5 shows the preliminary design parameters for the monochromator crystal.

Crystal	1	2	3	4
Reflection	111	220	311	511
X-ray energy (keV)	39.1	63.8	74.8	117.3
Asymmetry angle (deg.)	35	35	35	35
Thickness (mm)	3.0	5.0	5.0	5.0

**Table 4.5 :** preliminary specification for the side-bounce monochromator.

We note that the HEX power density is less than that at PDF, and the fan size, 0.2 mrad by 0.2 mrad, is also less than the PDF fan size. Thus we are confident that the PDF monochromator design, after being proven by experiment to be suitable for high-energy x-rays, can be used with little modification at HEX.



## **5. EXPERIMENTAL SYSTEMS**

HEX experimental system will eventually consist of three independently operating branches: the white beam branch, the center branch, and the side branch. The white beam branch and center branch are white-beam compatible. The side branch offers high-energy x-rays at fixed energy for x-ray diffraction and pair distribution function measurements.

The center branch is in the initial scope. The branch consists of experimental station E inside the storage ring for EDXD, and experimental station F in the satellite building for combined imaging and EDXD. While the experimental hutches for the white beam branch and side branch is in the current scope, the outfitting of them is not in the scope.

The center branch provides high x-ray energies up to 150 keV for phase contrast x-ray imaging in planar and CT modes. The resolution of about 10 microns combined with a field of view of 100 mm is suitable for most industrial batteries. The ability of phase contrast mechanisms to provide information on microstructure provides a new way for studying batteries.

The center branch will be equipped with special sample environment such as battery cycler. The design of the endstation will be compatible with the inclusion of equipment such as a large volume press owned by the COMPRES program. The imaging detectors will consist of two types of camera systems: CCD-based cameras for high spatial resolution and a CMOS-based camera for very high frame rate.

### **5.1 Experimental Station E Center Branch (Not In Scope)**

In the future, the experimental station E located on the experimental floor will be outfitted for monochromatic high-energy x-ray powder diffraction. The endstation equipment will be similar to that at XPD beamline, with beam-defining slit followed by clean-up slit and ion chamber, sample XYZ-stage and spinner, and an area detector will adjustable detector distance between 0.1 m and 2 m.

### **5.2 Experimental Station F in Satellite Building (In Scope)**

The satellite building design is similar to the JEEP satellite building, with one experimental enclosure consisting of concrete walls and roof. The overall size and design concept of the HEX satellite building is also similar to that of the Hard X-ray Nanoprobe (HXN) satellite building at the NSLS-II.

Techniques offered at the F station include EDXD (with multi-element Ge detector in the future), ADXD, small-angle x-ray scattering (SAXS), and imaging. In the future, SAXS with a sample

in hutch E and detector in hutch F can be performed. Imaging capabilities will offer a unique large field of view (especially vertical) of 100 mm horizontal by 20 mm vertical for imaging. Being white-beam compatible, a filtered white beam can be used at the F station for high-speed imaging using filters in the FOE and those in the endstation. The endstation allows for propagation phase contrast imaging that requires a large distance of up to 15 meters from the detector to the sample.

The endstation will feature the following:

- Large hutch size: 5 m wide by 20 m long.
- Large-scale samples/equipment
- Accommodates large volume press
- Accommodates complex experimental set up like 3D metal printing
- (Thermal) mechanical loads & contained processing cells
- Accommodates large mechanical testing equipment, load frame/translation stage
- High ceiling
- Dedicated gas exhaust system for battery and fuel-cell research

The design concept for the endstations in F features a modular concept, with three movable detector modules and the two removable sample modules. Figure 5.1 below shows schematically the modular arrangement in the endstation.

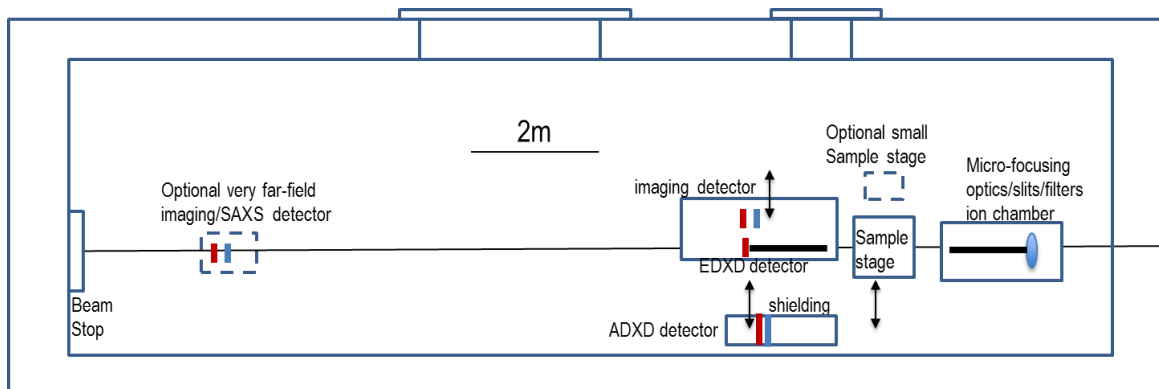


**Fig 5.1:** Preliminary design for the arrangement of imaging, ADXD and EDXD modules in the F experimental enclosure.

### Specifications for the experimental hutch in the satellite building:

The satellite building should be similar to the HXN satellite building, with the following changes:

- The hutch concrete wall thickness shall be 1m thick (compared to ~0.2m for HXN).
- The internal dimensions of the hutch should be unchanged
- The roof thickness is 0.5 m. This will make the roof of the hutch into an exclusion zone.
- The number of wall labyrinths is 20
- We will fit heavy lead labyrinth doors to the inside of the hutch (to simplify the PPS installation; a simple release switch can be fitted avoiding expensive locks or administrative controls The unistrut embedded in the wall shall be full height, Due to the weight of the doors (~1" lead), it is necessary that these are sliding rather than swing doors; Crane – not needed (we will use a small engine hoist as required for small lifting tasks, we will specify that all components are fitted with wheels).
  - Floor trenches for hidden and protected cable routing

Permissible changes:

- Temperature stability is as follows;
  - Hutch +/-0.5C over a two hour period, +/-1C over a 24 hour period.
  - Surrounding area +/-1C.
  - A hutch entrance vestibule is not required.
  - The air handling system can feed through a roof labyrinth to two air socks running the full length of the hutch; the false ceiling is not required. Air outlet labyrinths are required in each corner. The scope of the conventional construction contract will include the following;
    - Air inlet tube through the roof comprising a straight through steel pipe of adequate diameter to meet the ventilation requirements. This tube shall be cast into the concrete and finish flush with the surface. The wall thickness shall be >0.5" (adequate for welding the air labyrinth to the outside.
    - Air outlet tubes through the hutch sidewalls in each corner, similar to the air inlets but the diameter may be reduced since the flow will be carried by 4 such pipes.
- The vibration requirement is as follows;
  - The use of Concredamp, or similar such material is NOT required
  - The floor thickness under the hutch could be 15" (same as the experimental floor), Some trenches will be required in the floor for concealment of cables, see detail drawing.
  - The vibration isolation joints should be retained as used for the HXN design.

A vacuum pipe shall connect the beamline in the Experimental Hall to the beamline in the Satellite Building. This pipe will be no larger than 10" in diameter (this comprises 6" beam, 1" clearance each side to the tube, and 1" radial allowance for lead). The pipe will be fitted with 10" OD flanges; no allowance has been made for insulation. The pipe must be connected to the Satellite Building in a manner that permits survey alignment and preserves the building thermal performance.

### Other requirements

An exhaust system with fan (may be connected to the main exhaust system above the walkway inside the main ring building).

LN2 system: will be installed under a separate contract by a specialist supplier.

Trenches in the floor for installation of cables is shown in Fig.5.2b.

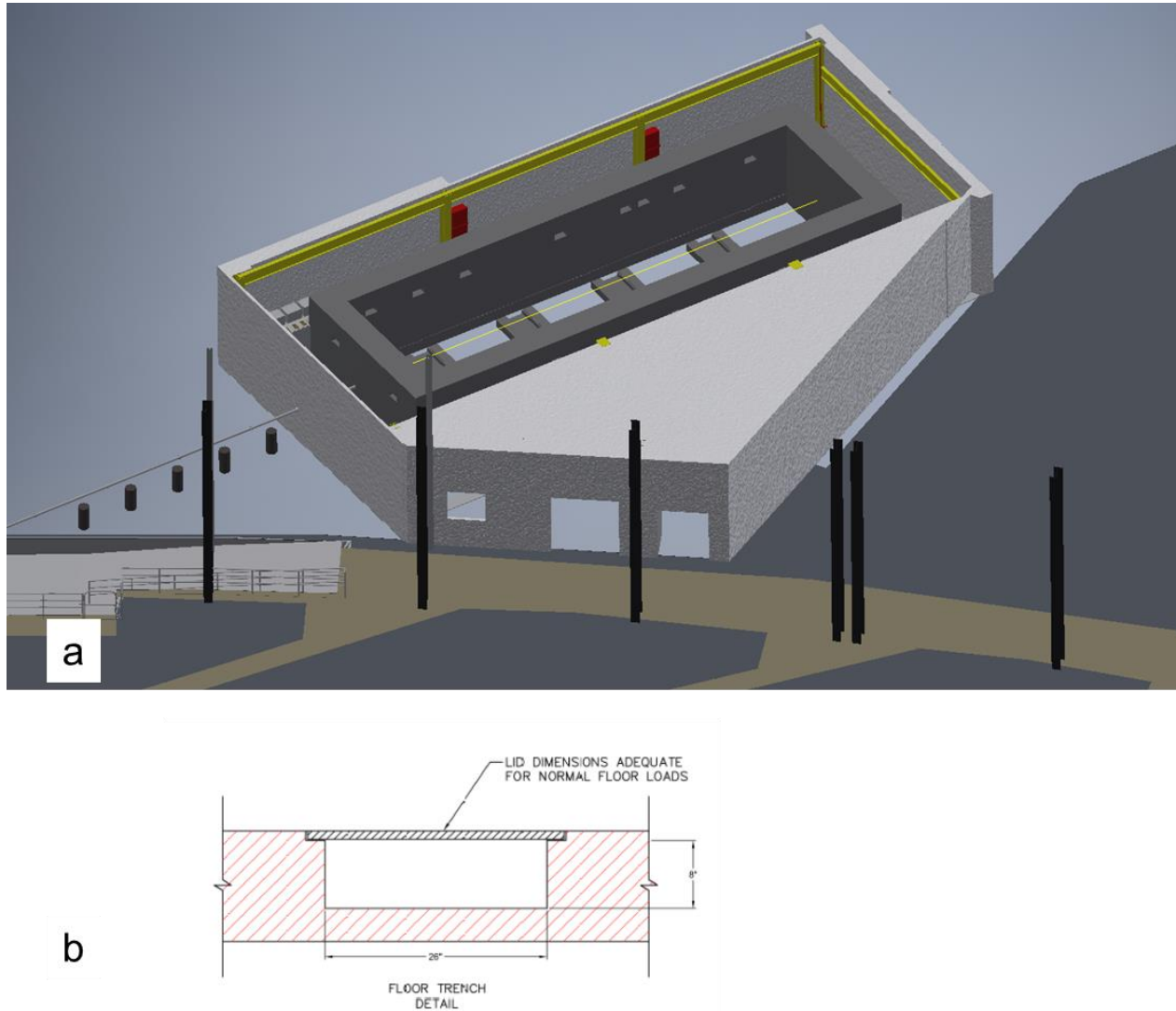


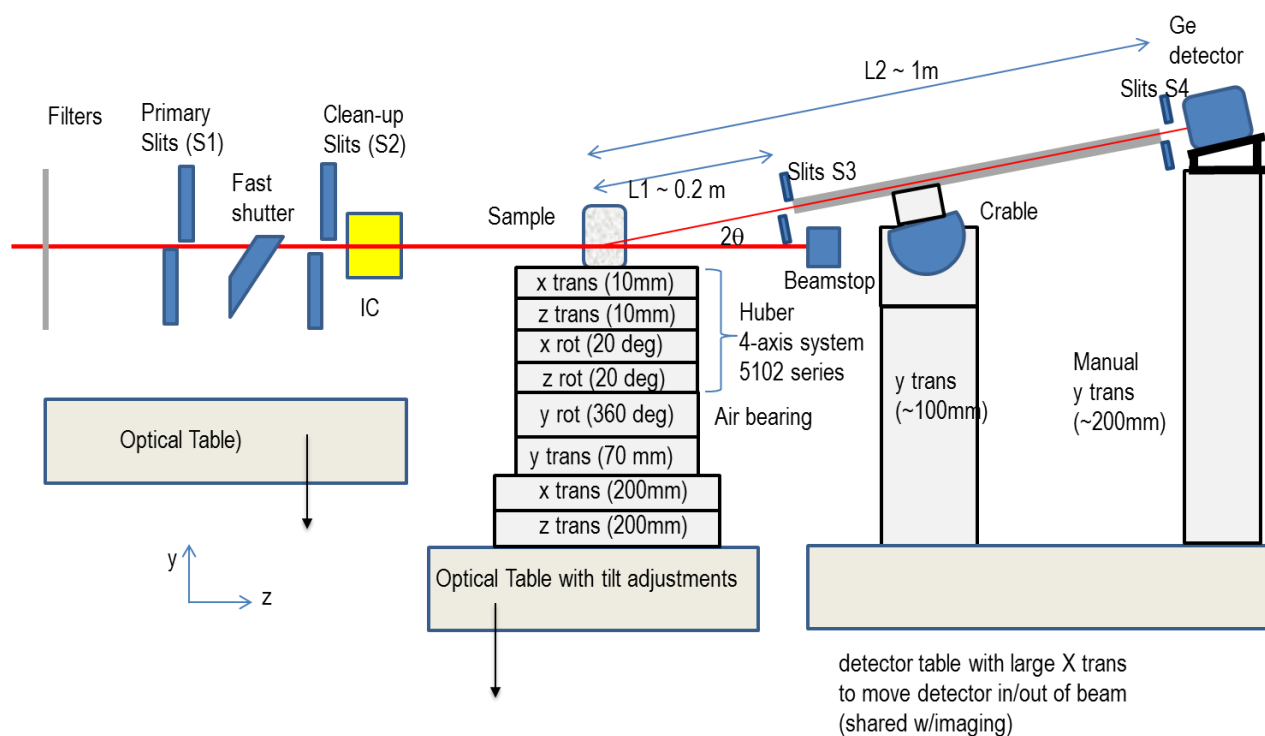
**Fig 5.2:** a) Design of satellite building housing the experimental hutch F. b) Details of floor trenches that are used at the JEEP beamline at the Diamond Light Source.

### Single-detector EDXD system

The single-detector system was decommissioned from the NSLS X17 beamline in late 2014 and 13-April-2018

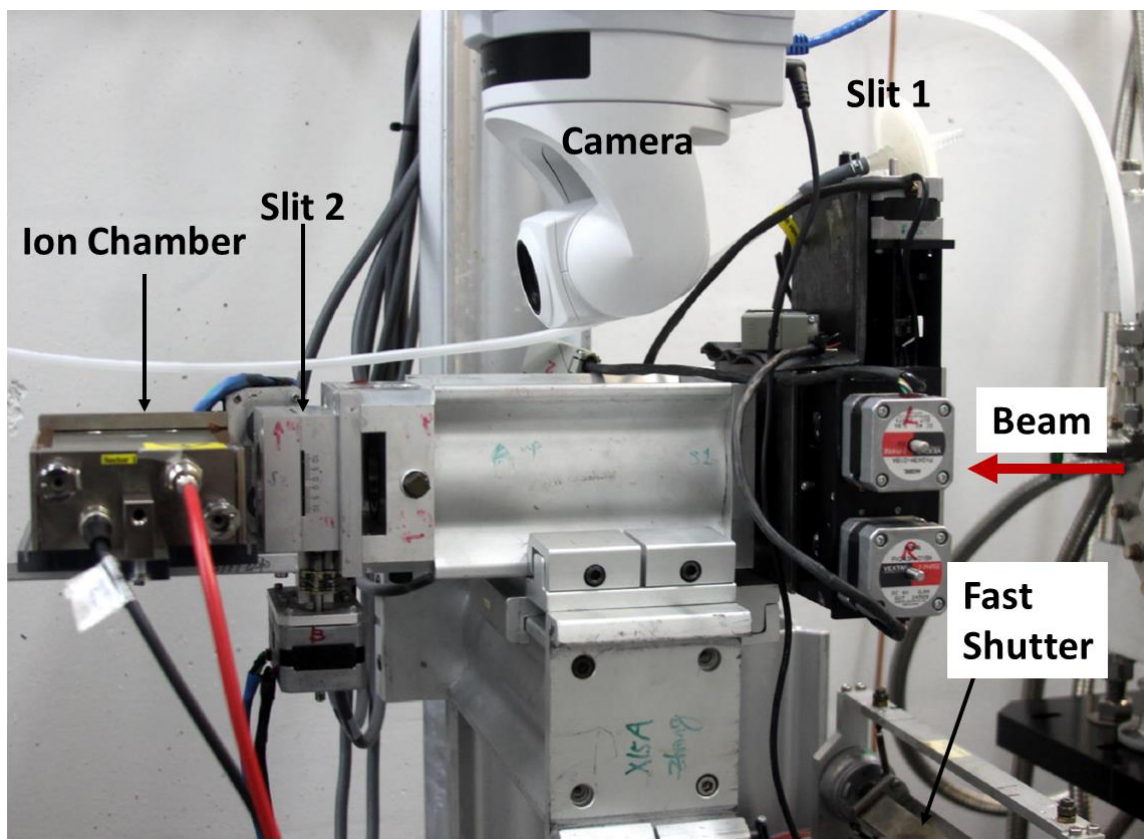
commissioned at the APS 6-BM beamline in mid-2015. The high x-ray energy provided by the APS bending magnet makes in-situ energy dispersive x-ray diffraction (EDXD) possible inside a battery. In contrast to conventional x-ray techniques, where the diffraction angle is varied, in EDXD the incident beam, diffracted beam and sampling volume are fixed (See Figure 5.4 for a schematic of the experimental geometry). The scattering geometry is extremely stable and sample profiling is accomplished by micro positioning of the battery. The long diffracted beam path ( $\sim 1$  m) facilitates a well-collimated diffracted beam to define a small gauge volume inside the battery. The volume is currently as small as 10 microns (x) by 10 microns (y) by 100 microns (z, along the beam direction). This volume is extremely small compared to the battery's length scale of 50 mm by 50 mm by 200 mm. The sample is micro-swept through this gauge volume while the EDXD spectra are collected by a high-resolution energy-dispersive-Ge detector.

Fig. 5.3 shows schematically the single-detector EDXD system with adjustable two-theta, incident and diffracted beam slits.



**Fig 5.3:** Configuration of the single-detector EDXD system with adjustable two-theta.

Fig. 5.4 shows a picture of the beam-conditioning components such as the fast-shutter, beam-defining slits (slit 1), clean-up slits (slit2), and ion chamber, currently in use at the 6-BM. The beam-transport tube is fabricated with X95 hardware with Lead shielding insert in the bore.



**Fig 5.4:** Picture of the fast-shutter, beam-defining slits (slit 1), clean-up slits (slit2), an ion chamber.

Figure 5.5 shows the sample stage and the two-theta arm. Note that the bore of the 1-m long X95 for the two-theta arm is also shielded to minimize noise in the detector.



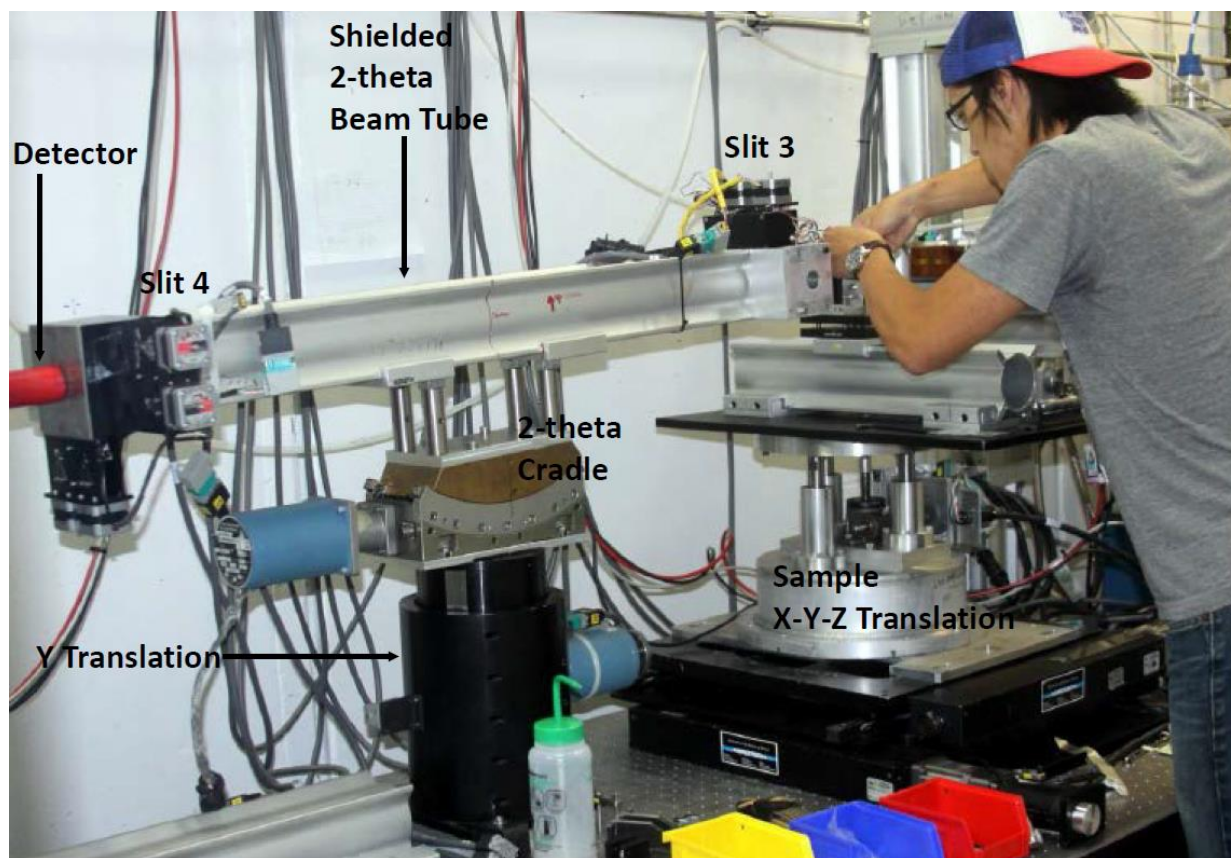


**Fig 5.5:** Picture of the sample XYZ translation, two-theta arm with slits 3 and 4.

The current system is based on a general purpose two-theta arm with 1-meter length and a vertical scattering geometry. While it offers the most flexibility for proof of principle experiment, the size of the sample, sample heating, and charging equipment is severely limited. The most important flexibility offered by the current system is the ability to change the two-theta angle. Changing the two-theta angle changes the energy of the diffracted beam for the same sample reflection. We experimented with different two-theta angles of 3, 4, 6 and 12 degrees for various battery systems, and found that a four-degree two-theta allows a good balance between the sample attenuation, gauge volume and achievable d-spacing.

A new endstation is planned. With the experience we have gained on the current system, we plan to design and construct the new system based on three optical tables. The beam defining slit, the sample x-y-z stage, and the diffracted beam slit will be located different tables. The detector, its motorized positioning system and its shielding will be supported separately from the two-theta arm to achieve better stability of the two-theta angle.

The individual components are discussed below in the order of the beam travel:

#### **a. Incident beam slit and beam-conditioning system**

A new optical table will be acquired. The table will feature a support stand with adjustable height. This optical table is located at the front of the experimental station. It is used to support the incident beam slit and beam-conditioning system.

The incident beam slit defines a well-collimated white beam. The current system uses an incident beam slit consisting of two slits. Each slit has four jaws of 10 mm thick Tungsten. The first slit is used to define the beam, while the second one, 200 mm downstream of the first one, is set to be slightly larger than the first one to reject the scattering by the first slit. We will specify a similar incident beam slits, but with vacuum compatibility to avoid ozone corrosion damage to the mechanisms.

The incident beam slit, along with filters and ion chambers, form the beam condition system as shown in Fig. 5.3. Note that the beam conditioning system is designed to accommodate EDXD, ADXD, and imaging. Thus the maximum aperture sizes for slits and ion chambers are specified to accommodate the imaging beam.

The specification for the beam conditioning system is shown in table 5.1. The reason for the specification of the micro-focusing optics is discussed later in ADXD system.

Component	Specification	Notes
Filter Assembly	SiC, 1, 2, 4 mm, Copper 0.1, 0.2, 0.4 mm Vacuum compatible	Water-cooling required
4-jaw Slits <sup>1</sup> & 2	0-25 mm (V) x 0-120 mm (H) 1 micron resolution 10 mm Tungsten blade Slit 1 is vacuum compatible	Water-cooling required
Ion Chamber 1 & 2	0-25 mm (V) x 0-120 mm (H) area 60 mm sensitive depth Thin (~50 microns) Aluminum window	IC (with air) response is 0.54 nA for $10^9$ ph/s @ 80 Kev
Fast Shutter	25 mm (V) x 120 mm (H) 10 ms response time	
Micro-focusing optics	K-B mirrors (0.5 m length for each mirror) or saw-tooth optics 30-~100 keV, 2m focal length, 1 micro-radians slope error	Desirable to have horizontal line focus



	Removable from the beam N2 or vacuum compatible	
Beam conditioning table	1 m width x 3 m length, at 1 m nominal height 0-100 mm vertical adjustment to switch between monochromatic beam and white beam, 1 micron resolution 200 kg load	

**Table 5.1:** The specification of the beam conditioning system.**b. Sample stage**

A new sample stage, on its own optical table, with motorized XYZ motion and removable rotation on the XYZ will be acquired. It will be designed to position a sample environment as large as the GE NaMx battery. The sample environment will include heating and charging capability, and the capability of housing at least two batteries so that the other battery can be charged while one is being studied in the beam. Since batteries may spend most of the time being charged and discharged, the ability to switch between the batteries improves efficiency. In addition to the minimum required XYZ motions for EDXD, the sample stack has an air bearing for performing CT and XZ translation and rotation for alignment and centering of the sample on the CT rotation axis. The specification of the sample stack is shown in table 5.2.

Component	Specification	Notes
X-Z Translation on X-Z Cradle	+/-10 mm translation range with 1 micron resolution +/- 20 degrees rotation with 0.001 deg. resolution 50 kg load	Reference Huber 5102
360 deg. goniometer for CT	360 deg. rotation range with 0.001 deg. resolution 10 rev./s maximum rotation speed 75 kg load	Reference ESRF ID-19 or APS 2-BM CT rotation air bearing
Y translation	70 mm range, 1 micron resolution 100 kg load	Reference NSLS elephant foot
X-Z Translation	200 mm range, 1 micron solution	

	150 kg load	
Sample table	0.5 m width x 0.5 m length, at 0.75 m nominal height 0-100 mm vertical adjustment to switch between monochromatic beam and white beam Tilt adjustment +/- 1 deg. with 0.001 deg. resolution, needed for alignment of CT rotation axis 200 kg load	Tilt adjustment can be achieved through kinematic mount of 3 vertical jacks

**Table 5.2:** The specification of the sample stack.

### c. Diffracted beam slit

Two motorized four-jaw slits connected by X95 tube, similar to the current incident beam slit, will be acquired. Vertical motion and rotation will be provided to this slit assembly. The combined vertical translation and rotation motion is essential for changing the two-theta angle.

The detector, having a sensitive area of 20 mm diameter (large compared to 0.1-0.4 mm by 10 mm active area), is located in the experimental station that has intense white x-ray beam. Thus, it is important to shield the detector so that the detector only sees the x-rays diffracted from the sample that are transmitted through the diffracted beam slits. Our current system utilizes a ¼ inch lead-shielded beam pipe, custom fabricated by Radiation Shielding Inc., between the collimating slits. We plan to design a collimator using ¼ inch lead thickness that fits inside the bore of X95 tube.

### d. Detector

A large vertical translation stage, with a cradle above, will be used to support the detector. The translation stage will share the same optical table as the diffracted beam slit.

Two new Ge x-ray detectors and HV supply and pre-amp electronics will be acquired. the MCA and data acquisition system will also be acquired. The specification of the EDXD detector system is shown in table 5.3.

Component	Specification	Notes
4-jaw Slits3 &4	0-10 mm (V) x 0-10 mm (H) 1 micron resolution 10 mm Tungsten blade	In-air
X95 link between slits 3&4	Constructed of X95 of 800 mm length End machined to mount slits Bore hole (~50 mm diameter) lined with 5mm thick lead	
Y translation	100 mm range, 1 micron resolution 50 kg load 1 micro-radians angular stability	Prefer design with center jack and large (>100 mm) footprint to promote angular stability
Cradle for 2-theta arm	+20 deg. range, 0.001 deg. resolution 30 kg load	
Detector jack	200 mm range, 10 micron resolution 30 kg load	manual adjustment OK
Detector angle tilt	+/-10 deg. tilt adjustment 20 kg load	Kinematic mount or cradle, manual adjustment OK
Ge detector 2 units	15 mm diameter sensitive area, 5 mm Ge thickness 20- 200 keV	Reference Canberra x-ray detector and XIA MCA
EDXD + Imaging table	1 m width x 3 m length, at 1 m nominal height Large (0-2m) x Translation to move detector in/out of the beam. 200 kg load	Height adjustment is desirable

**Table 5.3:** The specification of the EDXD detector system.

As a scope contingency, the current end station at the APS 6-BM beamline can be moved to NSLS-II. The hardware and software will be updated. In particular, the white-beam slits should be replaced by vacuum-compatible slits to eliminate corrosion by ozone.

Further in the future, at the mature scope stage, this single-detector system will be installed permanently in the experimental hutch D using beam from the white-beam branch, and serve as the work-horse for EDXD. It will be replaced by a multi-detector EDXD system discussed in Sec. 5.4.

At the HEX BAT meeting, the possibility of EDXD with two orthogonal (horizontal and vertical) two-theta arms was discussed. Having two arms is beneficial to strain mapping research, with limited benefit to the battery research. The disadvantage is some loss of adjustability for the first set of slits close to the sample. We will consider this design as a separate development project once the HEX beamline is operational and user demand data for strain mapping is available.

## Imaging capability

The work-horse instrument will consist of a very simple and typical micron-resolution tomography set-up. Figure 5.6 shows the preliminary design for the imaging endstation.

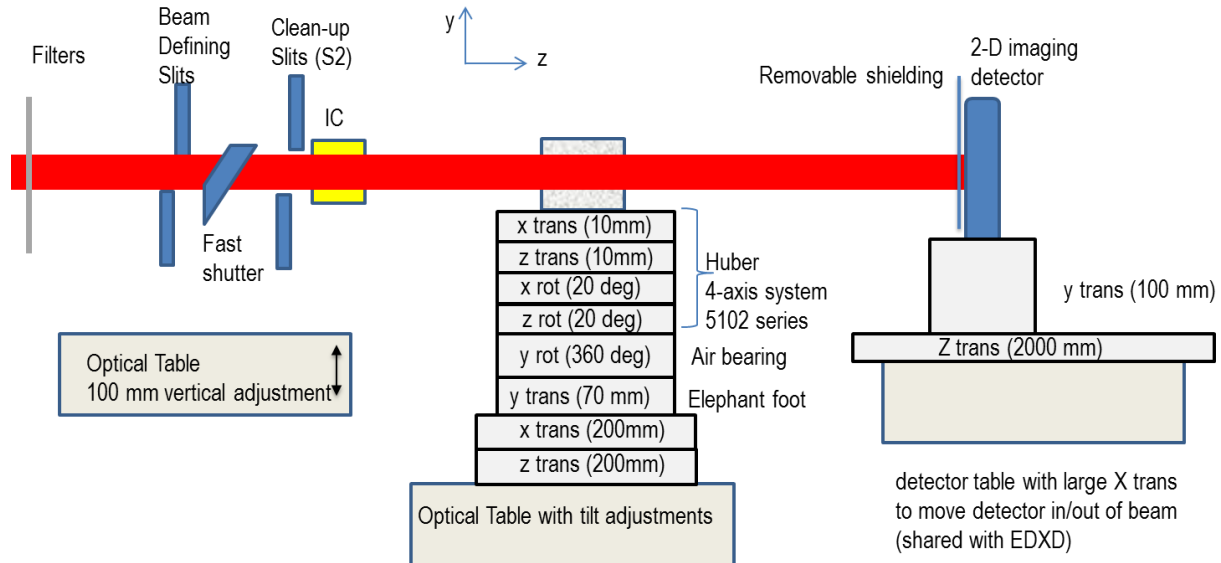


**Fig 5.6:** Design of the HEX imaging system

The imaging system will enable both absorption- (by moving the detector close to sample at about 100 mm) and propagation-based phase contrast imaging (by moving the detector away from the sample to a distance of greater than 0.1 m using the z translation under the detector).

Fig.5.7 shows schematically a typical imaging system consisting of x-ray source, a sample, and an area detector.

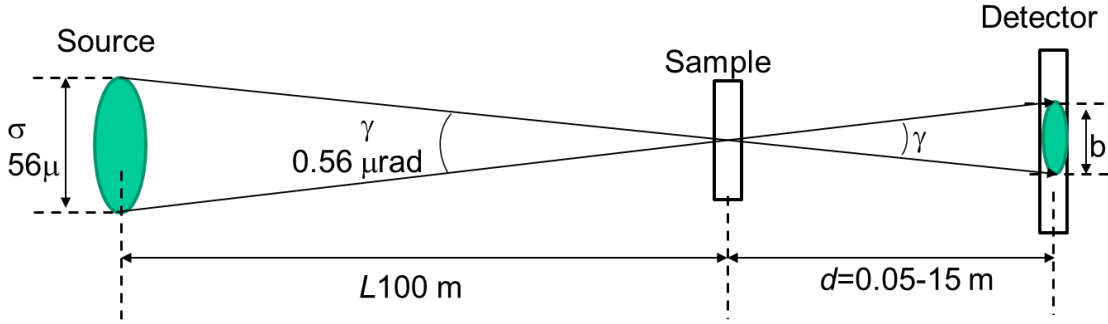


**Fig 5.7:** An x-ray imaging system to produce propagation-based phase contrast.

For weak phase object, the contrast due to propagation-based phase contrast is

$$I(x) \gg 1 + \frac{\lambda d}{2\pi} \phi''(x) \quad 5.1$$

where  $\phi''(x)$  is the phase of transmitted beam wavefront. The phase contrast increases with sample-detector distance  $d$ .

The on-axis Penumbral angle is defined as

$$\gamma = \sigma/L \quad 5.2$$

where  $\sigma$  is the source size and  $L$  is the source-to-sample distance. The penumbral angle characterizes the phase-contrast sensitivity of a beamline.

Image blurring due to source size is

$$b = d\sigma/L \quad 5.3$$

Eqs. 5.1 and 5.3 show that to maximize phase contrast, a large sample-to-detector is necessary. Thus, to minimize the blurring, a large source-to-sample distance  $L$  is desirable.

For the HEX imaging system in the satellite station,  $L=100$  m. The penumbral angle ( $\gamma$ ) is then  $0.56 \mu\text{rad}$  RMS, and  $1.3 \mu\text{rad}$  FWHM. Using Eq. 5.2, the blurring  $b$  is between  $0.07 \mu$  and  $20 \mu$  FWHM corresponding to a sample-to-detector distance between  $0.05$  m and  $15$  m (with the detector at the downstream end of the experimental station F). Note detector resolution is limited to about  $1 \mu$ .

Table 5.4 summarizes the phase-contrast performance, in terms of beam intensity, penumbral angle, field of view and energy range, for HEX and a few existing well-known imaging beamlines.

Beamline	Flux density (ph/s/mm <sup>2</sup> /0.1 %bw @ 60 keV)	FWHM horizontal penumbral angle ( $\sigma/L*2.35$ )	Beam Size H X V (mm)	Energy Range (keV)
HEX	$1.3 \times 10^{11}$	1.3 $\mu$ rad	100 x 20	30-150
ESRF ID19 W	$2 \times 10^{11}$	0.9 $\mu$ rad (on-axis)	45 x 6	20-100
SPRING8 BL20XU@245 m	$3 \times 10^{11}$	2.9 $\mu$ rad	4 x 2	10-60
APS 32-ID @70 m (RHB)	$1.6 \times 10^{11}$	4 $\mu$ rad	13 x 2.5	10-60
APS BM @70 m	$4.5 \times 10^9$	2.7 $\mu$ rad	(70) x 8	10-60

**Table 5.4:** Performance of HEX imaging compared to imaging beamlines at ESRF, Spring8, and APS.

A sample to detector distance of 0.05 m – 2 m d satisfy needs for most experiments according to experience at ESRF19ID and APS 2BM. For example, cracks and voids are usually imaged at  $d$  less than 0.5 m, insects and solid-fluid interface were successfully imaged at  $d$  of about 1 m. Thus, we specify a motorized range of 0.05-2 m for the detector longitudinal position ( $z$ ). For samples requiring larger  $z$ , a separate detector positioned near the downstream wall of the experimental station can be used.

#### a. Incident beam slit

An optical table with height adjustment supports the beam-defining slit, fast shutter and ion chamber to measure the flux of the imaging beam. This optical table is located at the front of the imaging station. The imaging slits and shutters should have large horizontal and vertical apertures to accommodate the 20 mm (V) by 100 mm (H) beam.

#### b. Sample stage

The sample stage for CT will be positioned on an optical table (see Fig.5.6). The base of the sample stage consists of motorized XYZ motion to position the center of rotation in the beam. A large vertical 360 degrees air bearing allows CT imaging of the sample. A small sample xz stage, and optional tilt adjustments, position the sample at the center of rotation.

#### d. Detector

Camera systems of different field of view and resolution will be purchased: the CCD-based camera will be used for high spatial but lower temporal resolution work, and CMOS-based camera will be used for very high frame rate data acquisition. A vertical translation stage will be used to support the detectors, allowing rapid changing between imaging detectors of different

resolutions. A long 2 meter z translation stage changes the sample-to-detector distance.

Table 5.4 lists the specification of the imaging endstation.

Component	Specification	Notes
2-D Imaging detectors (large area)	20 mm (V) x 100 (H) sensitive area 30 keV – 150 keV 5 micron – 250 micron resolution	Reference ESRF 19-ID and IMBL modular imaging detector
2-D Imaging detector (high resolution)	20 mm (V) x 20 mm (H) sensitive area 30 keV-100 keV 1-5 micron resolution	Reference ESRF 19-ID and IMBL modular imaging detector
Y translation	70 mm range, 1 micron resolution 20 kg load	
Z translation	2m range, 10 micron resolution 30 kg load	
Table for far detector	0.5 m width x 1 m length, at 1 m nominal height 200 mm vertical translation to move detector in/out of beam	Optional
Table shared with EDXD	1 m width x 3 m length, at 1 m nominal height Large (0-2m) x Translation to inboard move detector in/out of the beam. 200 kg load	Height adjustment is desirable

**Table 5.4.** Specification of the HEX imaging system

In collaboration with the team at ESRF ID19, we plan to test the SiC and diamond windows/filters for possible wave-front distortion. The windows for the ion-chamber and K-B mirror chamber should also be tested.

### ADXD Capability

The ADXD capability was not included in the scope of the CDR due to budget constraints. The ADXD system envisioned in the CDR is served by a sagittal-focusing monochromator and vertical focusing mirror similar to those used at the XPD beamline. At the advice of the HEX

BAT at the first BAT meeting in September 2017, we are adding the ADXD experimental system to the F experimental hutch. Instead of using dedicated ADXD optics, the ADXD will use the imaging monochromator and have an energy range of 30 to 150 keV. The beam used for ADXD will be apertured from the imaging beam to a size of approximately 0.5 mm by 0.5 mm. Alternatively, also at the urging of the BAT, the beam can be focused by K-B mirror, compound refractive lens or saw-tooth lens to a spot with a diameter of a few microns. The justification for adding the ADXD system is that the experimental system and micro-focusing optics are relatively inexpensive compared with dedicated focusing monochromator and mirror. The ADXD system will share the same beam-conditioning slits, ion-chambers and sample stage as that of the EDXD system. The beam-conditioning system will need to be raised by 25 mm to be at the correct position for EDXD when moving from ADXD mode to EDXD (i.e., from white beam to monochromatic beam). Fig.5.8 shows schematically the design of the ADXD endstation.

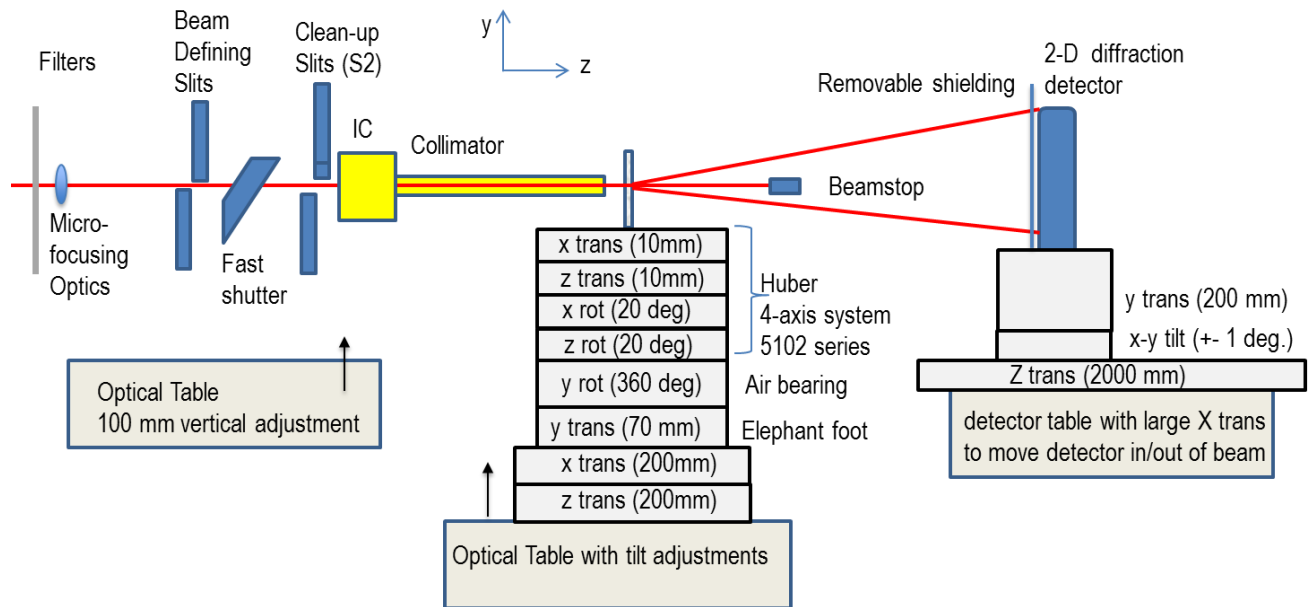


**Fig.5.8.** Preliminary design of the ADXD endstation.

Options for micro-focusing include: K-B mirror, saw tooth as used at APS-1ID, Kinoform lens pioneered by Ken Evans-Lutterodt, and a compound refractive lens (CRL). The characteristics of the focusing options are summarized in table 5.5.

	Aperture	Focal spot size	Line-focus	Energy tunability	Price	In-line
K-B mirror	0.5 mm x 0.5 mm *	1 micron	Yes	Easy	\$400k	No
Saw-tooth	1 mm x 1	1 micron	Yes	Relatively	\$100k,	Yes



	mm			easy	R&D	
Kinoform	0.3 mm x 0.1 mm	0.2 micron	No	Difficult	\$100k, R&D	Yes
CRL	0.3 mm	1 micron	No	Relatively difficult	\$100k	Yes

**Table 5.5** Comparison of different focusing schemes. \*The K-B mirror aperture assumes 0.5 m long mirrors at 1 mrad incident angle.

The requirements for micro-focusing are:

1. Spot size smaller than 10 microns
2. Option for line focusing is desirable
3. Focal distance of about 2 m. The source distance is 100 m.

Based on our discussions with micro-focusing experts Evans-Lutterodt, Chu, and Shi, we are proposing the K-B mirror as the first option due to its commercial availability. We will consider saw-tooth as the second option due to its excellent performance at APS 1-ID.

To estimate the smallest possible focal spot, the following source parameters were used to simulate the source size for SCW70:

energy: 3.0 GeV

poles: 29

period: 7.0 cm

sigmax: .041 mm, Sigma X Assumes low-B straight

sigmay: .0030 mm, Sigma Y

field: 4.3 T , Magnetic field

This results in a peak-to-peak horizontal electron excursion of 0.107 mm. The RMS source size due to excursion  $\sigma_{X\_excursion}$  can then be calculated assuming that the excursion is a sine wave.

$$\sigma_{X\_excursion} = (\text{peak-to-peak excursion})/2.8 = 0.038 \text{ mm}$$

The convolution of this with the RMS of current NSLS-II electron beam ( $\sigma_{X\_beam} = 0.041 \text{ mm}$ ) results in a horizontal source RMS size of 56 microns, or a FWHM 132 microns. Assuming a demagnification ratio of 50:1, the contribution of source size to focal spot size (sigma) is estimated to be 1.1 microns with a FWHM of 2.6 microns.

Fig.5.9 shows the design of the focusing optics, demonstrating the effect of the source size and

length on the focal spot size for an ideal focusing optic.

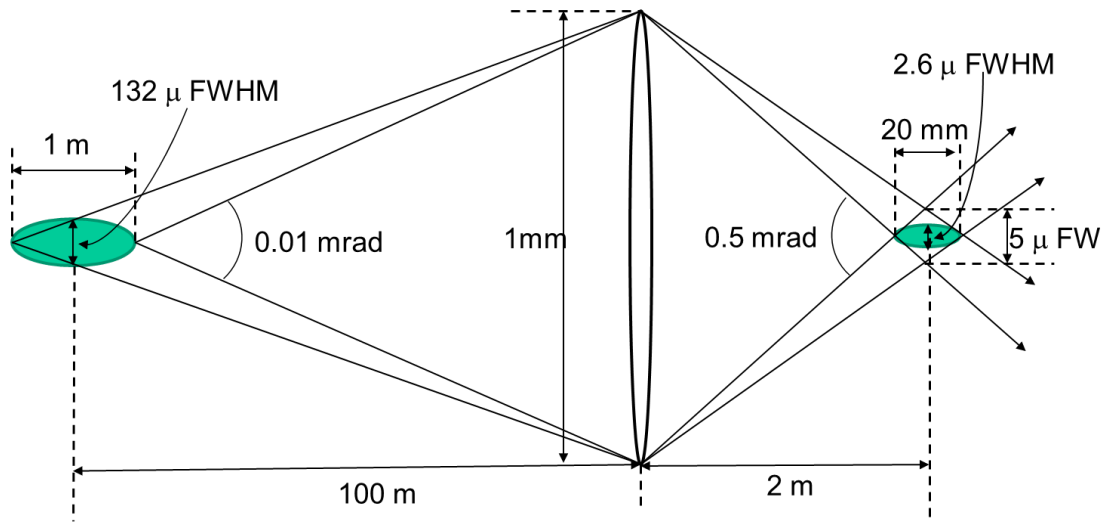


**Fig. 5.9** Effect of source length on focal spot size.

The 1 m length of the wiggler at a divergence of 0.01 mrad contributes to an additional horizontal FWHM of  $100 \text{ mm} \times 0.5 \times 10^{-3} \text{ rad}/2 = 0.0025 \text{ mm}$ . Convolution of this with the focal spot size from source size results in an estimation of the smallest possible focal spot FWHM of 3.6 microns (H) by 2.5 microns (V). Thus we will specify the figure errors of the focusing optics to not contribute to more than 2 microns in focal spot size. This, when combined with a working distance of 2 m, results in a slope-error specification of 1 micro-radians.

The specification for the ADXD endstation is summarized in table 5.6.

Component	Specification	Notes
ADXD flat panel detector	400 mm×400 mm active area, CsI phosphor coating 0.2mm pixel	Reference XPD & PDF detectors
Collimator	XPD & PDF design	
Beam stop with embedded photo-diode	~ 2 mm diameter 5 mm Tungsten depth Remote control of +/- 3 mm in x-y position	Reference PDF beam-stop design

Y translation	200 mm range, 1 micron resolution 40 kg load	Prefer design with center jack
Detector angle tilt	Around x (H) and y(V) axis +/-1 deg. tilt adjustment, 0.001 deg. resolution 50 kg load	For alignment  Facilitates changing between the apertured beam and the K-B focused beam
Z translation	2m range, 10 micron resolution 30 kg load	
ADX table	0.5 m width x 2 m length, at 0.75 m nominal height Large (0-1.5m) x Translation outboard 200 kg load	Height and tilt adjustment is optional

**Table 5.6.** Specification of the ADXD endstation.

Although commercial flat-panel detectors are successfully used at various facilities, the implementation of photon-counting CdTe 2D detectors should be considered for future upgrades. The technical advantages are noise free and fast (few 100 Hz) acquisition, allowing the study of high-temperature minority phases (during quench), surface layers, and intermediate phases.

### Data acquisition and analysis

The present data collection/analysis system at 6-BM involves three computers: the detector computer; beamline control Computer; and the data analysis computer. The detector computer controls the energy dispersive diffraction spectra collection with a Canberra supplied system. The Beamline control computer controls the settings of the beam-defining slits, diffracted beam slits, and the sample x-y-z position via stepper motors. It issues the TTL logic pulse to the detector computer when a new data collection position is reached in the sample. The macro for the experiment runs on a SPEC general purpose diffraction program. A separate program written in IDL is then used to generate the 2-D intensity map of the energy-position in order to visualize the phase change as a function of sample position.

We will develop software to incorporate these processes into a single user-friendly package. An online display of the preliminary phase analysis based on known position of Bragg line and phase map during data collection will be developed. In addition, a more sophisticated set of

software will be developed for any user wishing to perform more detailed analysis. This software will allow much more detailed analysis using refinement of the diffraction pattern, and produce 2-D and 3-D maps of a particular phase.

### 5.3 Multi-detector EDXD system (not in scope)

The experimental system for EDXD, currently installed at the APS 6-BM beamline, was designed and built at the NSLS over the past two decades for the purpose of strain-mapping of engineering materials. As such, it is not optimized for battery research. Among the drawbacks are:

1. It is time-consuming, thus only a line profile can be measured. For battery research, a 2-d or 3-d map is necessary for characterizing the reaction front.
2. The gauge volume is too large due to time constraints.
3. The software was written for strain mapping. It is cumbersome to use and unreliable for battery research.

In the future, the HEX beamline will include a new, novel system to allow parallel data collection. Figure 5.10 shows the new system proposed. Comparing Figure 5.8 with figure 5.4 shows that they are essentially the same with one key difference: the single-element Ge detector in the current system is replaced by a one-dimensional array of Ge detectors. Currently, the Ge detector of about 20 mm sensitive area is behind a 0.1-0.4 mm (in the diffraction plane) by 10 mm (perpendicular to the diffraction plane) slit. The slit size in the diffraction plane (vertical) needs to be small in the diffraction plane to define a small two-theta range so that the energy resolution of the measured spectra is not dominated by the divergence of the diffracted beam. Thus, a tiny fraction of the diffracted beam signal and the available detector area is used for the measurement. To profile along the beam direction, the sample is scanned along the beam and measurement is made sequentially at every point. With each measurement taking approximately one minute, the scan time is about two hours for a profile along a line with 100 data points. As such, it is impossible to conduct a two-dimensional scan with 100 x 100 points.

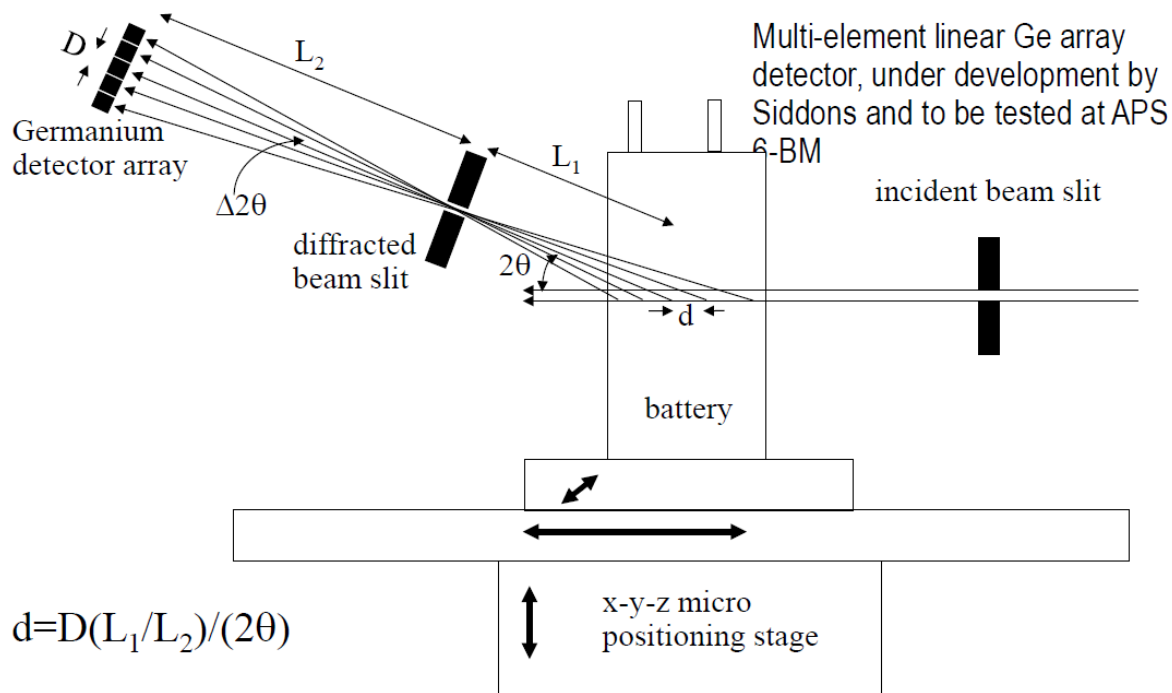


**Fig 5.10:** Planned multi-element linear Ge array detector system.

About 10 years ago, a collaboration between GE and BNL proposed a new idea of using an array of Ge detectors, each having a dimension of 0.2 mm by 10 mm for the experiment. Figure 5.9 shows that each detector element acts as the detector in the current setup and measures the diffraction signal from a part of the sample along the beam direction. By using an array, the whole length of the battery along the beam direction is measured simultaneously. Since the measurement at each point is the same as current setup, we can estimate that the measurement time of 1 minute per line is sufficient. Thus, it would take approximately 2 hours to have a two-dimensional profile of the battery by scanning the sample perpendicular to the beam and measuring at each point for one minute.

Figure 5.11 shows plots the incident x-ray flux provided by the wiggler after filtering by 4 mm of aluminum to attenuate the low energy x-rays. Low energy x-rays are filtered before reaching the sample since they do not have the penetrating power to go through the sample, and will only contribute to sample damage and detector noise. The x-ray flux decreases with x-ray energy. The transmission of x-rays through the battery increases with x-ray energy. Using the battery composition data (120 g Ni, 98 g NaCl, 3.8 g NaF, 0.51 g NaI, 3.8 g FeS, and 115 g NaAlCl<sub>4</sub> occupying a volume of 2.8x2.8x20 cm<sup>3</sup>), the transmission through the diagonal direction of the sample which represents the most attenuation is calculated and shown in figure 5.10. The diffracted x-rays originating inside the sample need to go through the sample in order to reach the detector. Due to the small two-theta angle, the x-ray intensity diffracted by the sample is proportional to the incident x-ray flux multiplied by the sample transmission. The result, shown in figure 5.10, shows that the most useful part of the x-ray spectra is from 70 to 150 keV, which covers a d-spacing range from 0.12 to 0.26 nm for a two-theta angle of 4 degrees. This range conveniently covers the d-spacing of NaCl 220 and 222, Ni 200, and Mcl2 113 reflections of most

interest in battery chemistry. The design will have the flexibility to change between a two-theta of 2 degrees to 6 degrees by translating and rotating the diffracted beam slit and the detector.

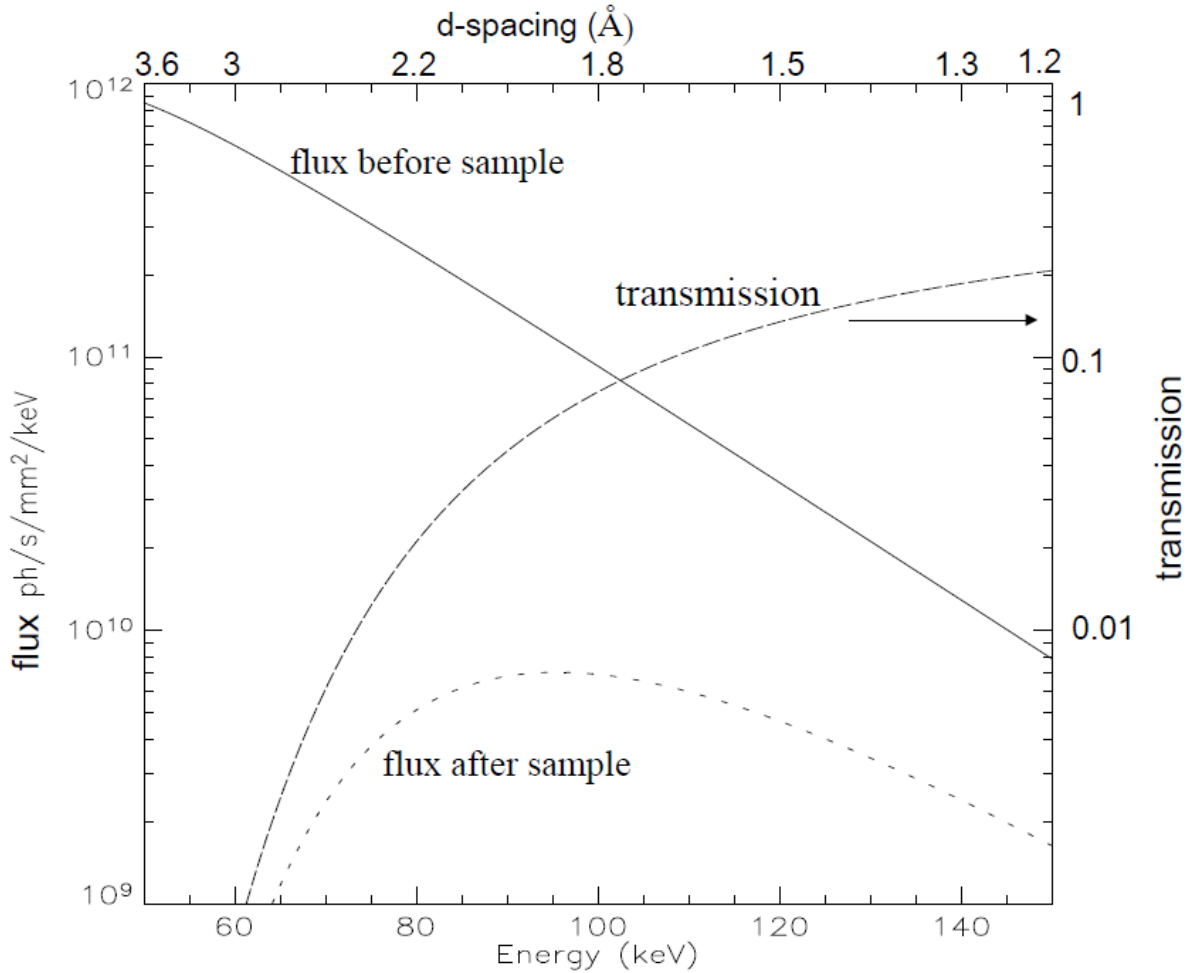


**Fig 5.11** Simulated flux before and after GE NaMx battery, and transmission through the sample as a function of x-ray energy.

Figure 5.11 also shows that the flux through the sample has weak energy dependence in the x-ray energy range between 80 and 120 keV. We plan to construct a standard sample with the same composition as the battery to achieve the same absorption characteristics, but with the phases distributed uniformly through out the standard. Using data acquired with the standard sample, a calibration curve can be developed for different phases, thus allowing quantitative phase analysis. This algorithm can be incorporated into the data analysis software.

While the new idea of parallel data acquisition speeds up the data acquisition by orders of magnitude compared with the current setup, one noticeable drawback is that different detectors use different two-theta angles. The difference in two-theta between the detector elements,  $\Delta 2\theta/2\theta$ , needs to be small enough (within 20%) so that the energy difference for the same reflection,  $\Delta E/E$ ,

stays in the flat region in Figure 5.11. From the figure, we have

$$\Delta E/E = \Delta 2\theta/2\theta = nD/(L_2 2\theta) \quad \text{Eq. 5.4}$$

where  $n$  is the number of detector elements, and  $D$  is the pixel size of the detector.

The gauge volume covered by each detector element is

$$d = DL_1/(L_2 2\theta) \quad \text{Eq. 5.5}$$

The length of the gauge volume that can be covered is

$$nd = nDL_1/(L_2 2\theta) \quad \text{Eq. 5.6}$$

From Eq. 1 and 3, we have

$$\Delta E/E = (nd)/L_1$$

Requiring that  $\Delta E/E < 0.2$  and  $nd = 40$  mm to cover the whole battery, we have

$$L_1 > 40/0.2 = 200 \text{ mm} \quad \text{Eq. 5.7}$$

For the purpose of design, we choose the minimum required distance between the sample and diffraction slit  $L_1$  of 200 mm. We also impose the condition that the gauge volume along the beam direction ( $d$ ) to be 0.25 mm, or 5% of battery length along the beam direction. The number of detector elements is then 160 to provide complete coverage of the 40 mm sample length. Using Eq. 5.5,

$$D/L_2 = d 2\theta/L_1 = 0.25 * (4./57.3)/200. = 8.7 \times 10^{-5} \quad \text{Eq. 5.8}$$

Eq. 5.8 gives the ratio between the detector resolution and the detector to diffraction slit distance. By using a detector in-plane size of 0.25 mm, slightly less than the detector slit size we currently use (0.4 mm), we have  $L_2 = 0.25/8.7 \times 10^{-5} = 2800$  mm, or 2.8 m. This distance, though large compared to the current detector distance, is conveniently achievable within the limitation of the experimental station size. The detector size of 0.25 mm in the diffraction plane is also convenient for fabrication. For the out-of-plane detector size, we choose a size similar to the detector slit size out of plane that we currently use, 10 mm.

Table 5.7 provides a summary of the design parameters based on the above discussion.

design parameter	Quantity	notes
------------------	----------	-------

d-spacing coverage	1.2 – 3.6 Å	
x-ray energy (E)	50 – 250 keV	60-150 energy range with flux above $10^9$ ph/s/mm <sup>2</sup> /keV
Two-theta angle ( $2\theta$ )	4 degrees	Variable between 2 and 6 degrees to allow other d-spacing coverage
Two-theta variation between detector elements ( $\Delta 2\theta/2\theta$ )	< 20%	
Sample to diffraction slit ( $L_1$ )	0.2 m	
Sample to detector ( $L_1+L_2$ )	3 m	
Energy variation between detector elements for the same d-spacing ( $\Delta E/E$ )	< 20%	
Detector pixel size	Minimum 0.25 mm (D) in plane, 10 mm out of plane	Smaller in-plane detector pixel size results in higher Z resolution along the x-ray beam
Number of detector elements (n)	160	
Detector size (D)	40 mm in place, 10 mm out of plane	
Sample coverage along beam direction (nd)	40 mm	
Resolution along beam (d)	0.25 mm	
resolution perpendicular to the beam	1-50 microns	Defined by the incident beam slit. Can be very small subject to counting time limitations

**Table 5.7** Preliminary specification of the multi-element detector EDXD system.

The proposed Ge strip detector is not commercially available. Since 2010, the NSLS detector group led by Peter Siddons has been working on a prototype Ge strip detector. The first successful proof-of-principle test was conducted at the NSLS X7A beamline using white-beam from the NSLS bending magnet. A next-generation Ge strip detector was tested in late 2017 on the EDXD system at the APS-6-BM beamline, demonstrating the system's capability for diffraction imaging.

As discussed earlier, each detector element uses different two-theta angle around 4 degrees, and thus uses a slightly different part of the incident x-ray spectra. Thus, two-theta angle calibration for each individual detector is necessary to allow absolute d-spacing measurement, and intensity calibration is necessary for quantitative measurement. Since the attenuation of the sample modifies

13-April-2018



the spectra of the diffracted beam, we plan to construct a calibration sample of the same size as the battery, and with the same attenuation energy dependence. The calibration sample will be constructed with NaCl micro-crystals uniformly dispersed in an amorphous BN or plastic matrix and will be fitted inside the same steel case as our batteries. By acquiring diffraction data from this standard sample, we will be able to calibrate the two-theta angle for each detector element, and normalize the intensity across detector elements.

## 5.4 White Beam Branch (Not in Scope)

The C branch provides energy-dispersive x-ray diffraction (EDXD) at high x-ray energies up to 200 keV. Spatial resolution is 5 microns in the transverse direction and 50 microns in the longitudinal direction.

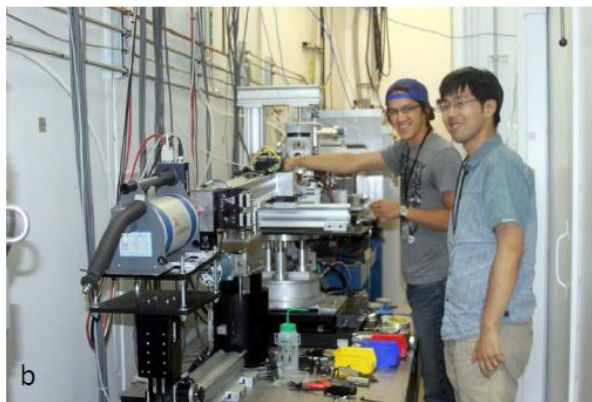
The white-beam branch will feature the following:

- K-B mirror in the hutch for micro-focusing of white beam
- Workhorse instrument for EDXD with 2 orthogonal detectors (up and outboard)
- Adjustable two-theta
- Could re-use mostly endstation being upgraded at 6-BM of APS
- Compatible with a diamond-anvil cell with white beam

Figure 5.12b shows an example of the energy-dispersive diffractometer to be installed in the C branch.



Angle-Dispersive Diffractometer



Energy-Dispersive Diffractometer currently at APS

**Figure 5.12:** Examples of diffractometers to be installed as part of the HEX experimental system.

## 5.5 Experimental Station B side Branch (Not in Scope)

The experimental station B will be dedicated for high-energy x-ray scattering with monochromatic beam. The endstation will be largely similar to that at the PDF beamline, currently being constructed for operation in 2018. Thus the design and specification of HEX station B can benefit from experience gained at the PDF beamline. The HEX program and the PDF program belong to the same Diffraction and In-Situ Scattering (DISC) division of the NSLS-II. This arrangement facilitates exchange of expertise.

Figure 5.12a shows an angle-dispersive diffractometer, currently installed at the XPD beamline of the NSLS-II, as an example of HEX diffractometer for the side branch.

## 5.6 Beamline Utilities

The utility systems for HEX beamline comprise the following services in a standardized (but tailored) “utility pack”:

- Mains electrical distribution: 30 kVA total, for the experimental floor only. Additional power for the power hungry equipment in satellite building will come from LOB2.
- Chilled water for electrical racks and user equipment
- De-ionized (DI) water for beamline optical components
- Compressed air, experimental gases, gaseous nitrogen, and liquid nitrogen
- PPS wiring and conduits
- Utility bridges between hutches, or pylons, for pipes and cable trays

The endstations will have the standard suite of utilities including electrical power, liquid nitrogen, DI water and process cooled water, compressed air, and exhaust ventilation.

The design approach includes the supply of air and water in modules (stainless steel for water, copper for air) utilizing purchased standard manifolds. Flow measuring or flow alarms will be used on the water return circuits where required.

Water pipes are located high enough on the wall to accommodate the flow sensors vertically below the tap-off points.

Typically each hutch will be provided with two GN2 taps for venting of vacuum equipment and other uses. Figures 5.13 and 5.14 show a typical layout.

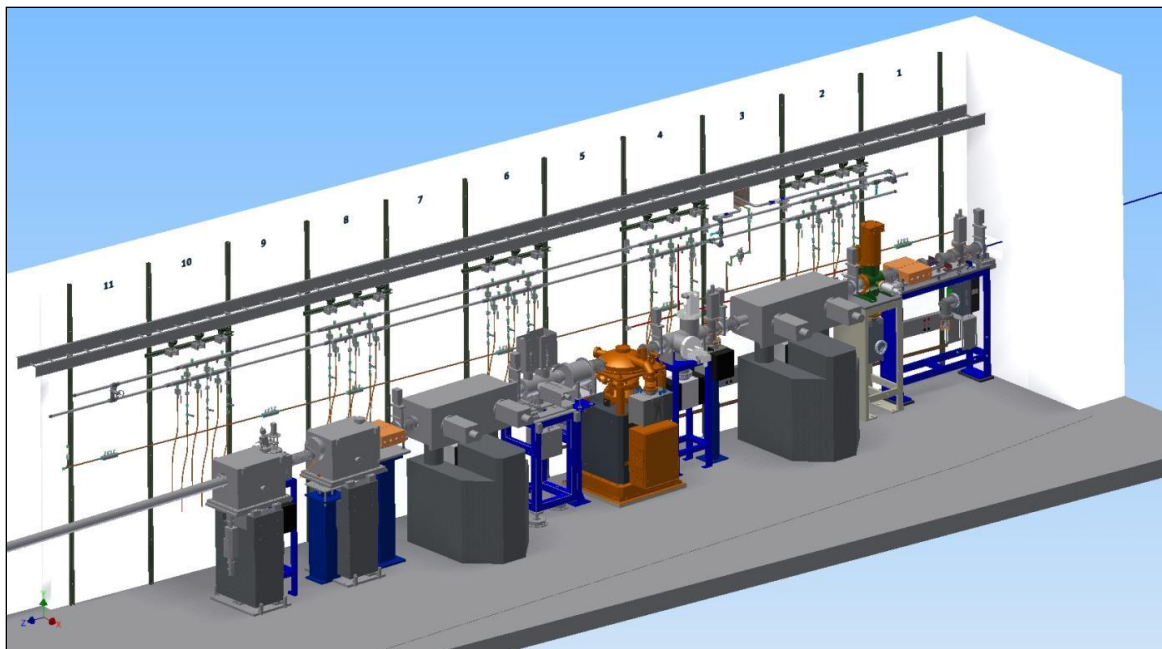


**Figure 5.13** Typical layout of utilities within an FOE; from top: cable tray, flow transducer heads, DI water flow/return, compressed air.

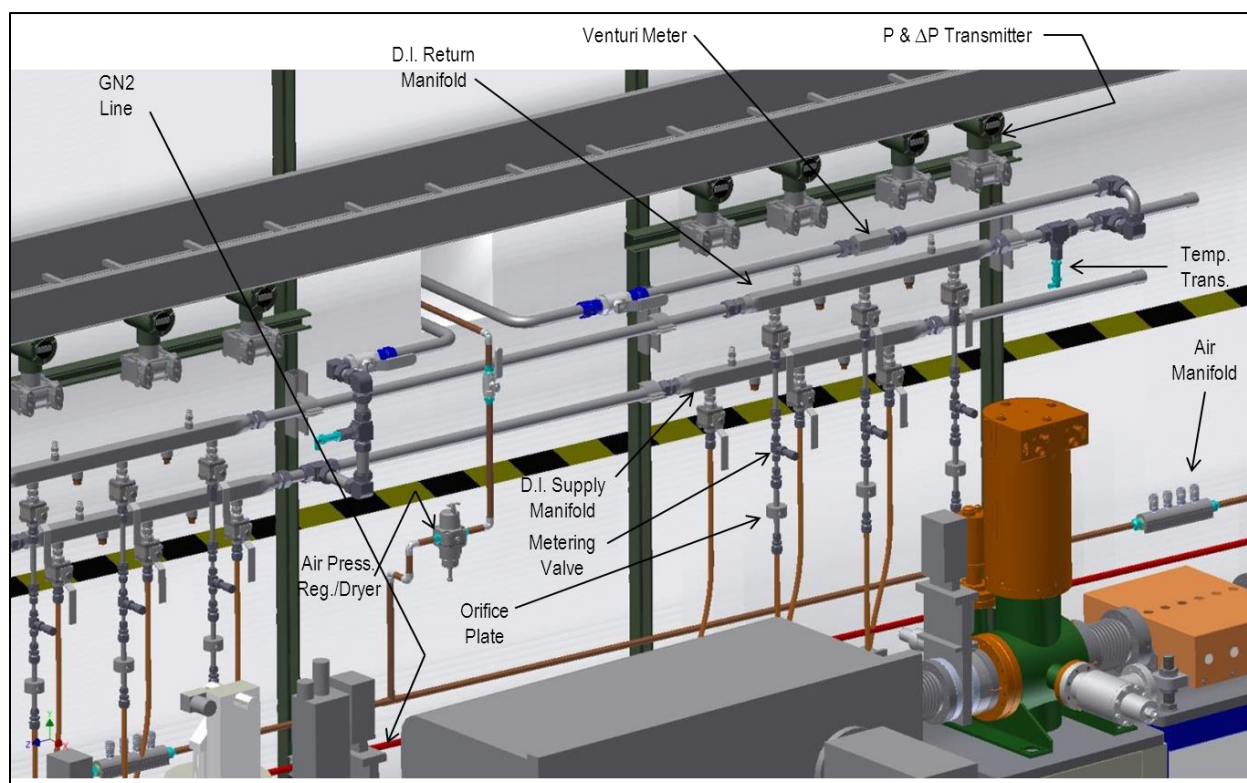


**Figure 5.14** Closer view of a utility layout in a typical hutch, showing the DI water and compressed air

passing through the ratchet wall into the FOE, and the onward pipework distribution.

The AC power sockets and the water connections will be located in alternating 1m “bays” for improved electrical safety. The two supply transformers provide power for sensitive and non-sensitive applications. Outlets inside the enclosure are supported within a Wiremold product designed for such applications. Figure 5.15 shows a typical layout for the electric mains.

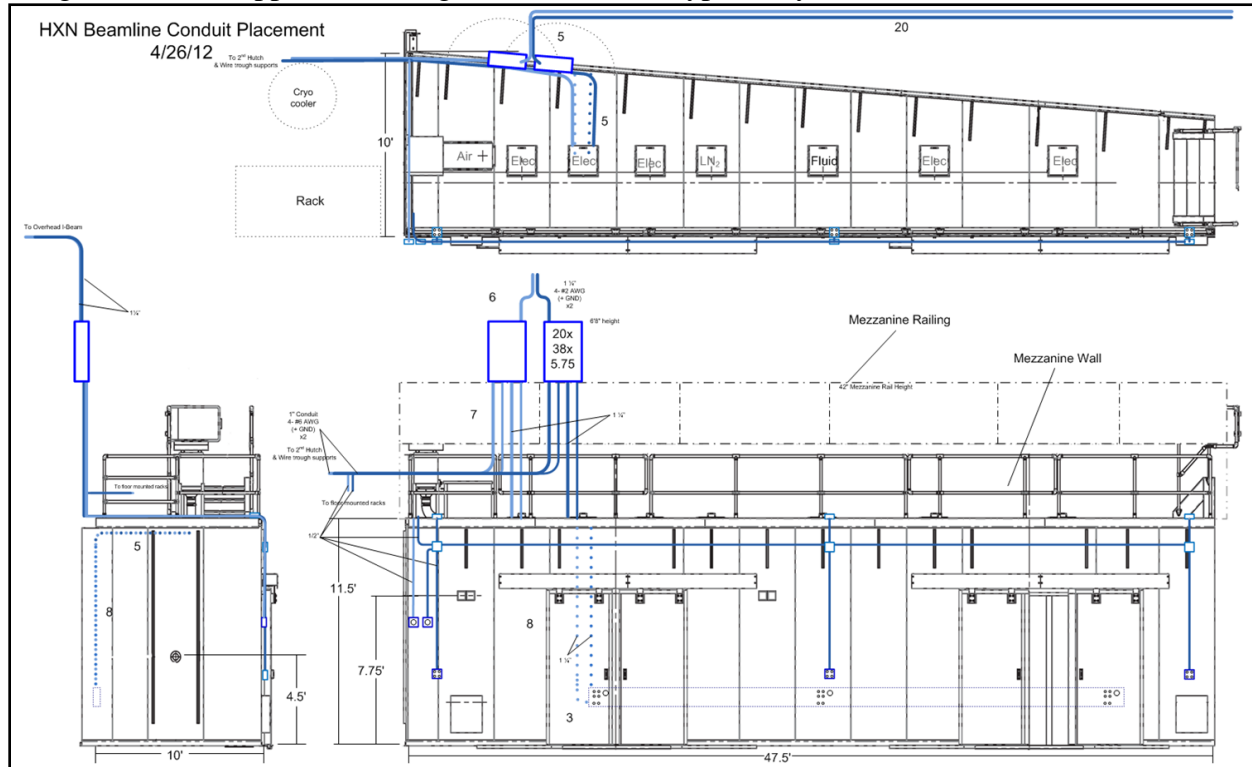


**Figure 5.15** A typical layout for the electrical mains distribution.

Mark up of the utilities for the HEX beamline was produced and given to the utility engineers for budget estimates. The markup is shown in Fig. 5.16.

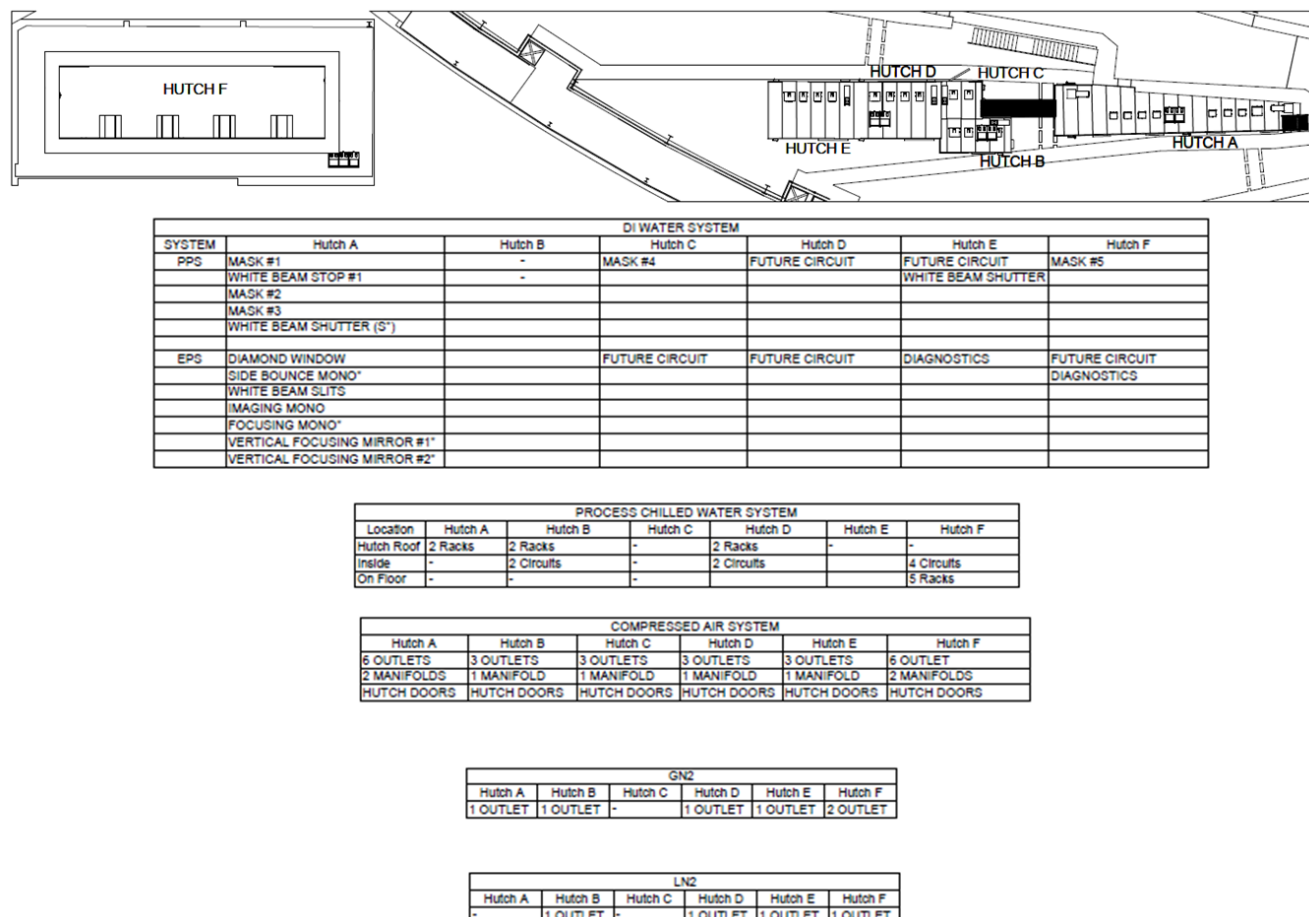


**Figure 5.16:** Preliminary utilities design for HEX beamline.

## 5.7 Equipment Protection System

HEX is expected to handle x-ray beams with very high power and power densities. Therefore, care must be taken to design the beamline with components that can handle these power loads. Any component that has to handle these high levels of power has to be monitored. The beamline Equipment Protection System provides a means of monitoring the components which, when jeopardized, can cause component failure. The EPS has the responsibility to act on alarm conditions by mitigating the situation that has caused the alarms.

The HEX EPS will monitor and interlock the devices in the front end and the beamline. HEX frontend is designed to have two safety shutters, one photon shutter, and a few masks. In addition, the front end will also have vacuum inline valves to provide vacuum isolation. The front end is also expected to have a fast valve to provide a conductance limitation during a vacuum accident. Due to the large power loads, all components in the front end that intercept the beam will have water cooling. These components are typically the fixed mask and photon shutter. The water flow will be monitored by flow meters and the signals will be fed to the EPS. All vacuum valves will be pneumatically operated. All vacuum valves will be operated by the EPS and have their positions monitored. HEX will have beam conditioning optics upstream of



the monochromator. The beam conditioning optics will see the large power of the beam and as such will be interlocked by the EPS. Fig. 5.17 shows preliminary markup of HEX EPS system.

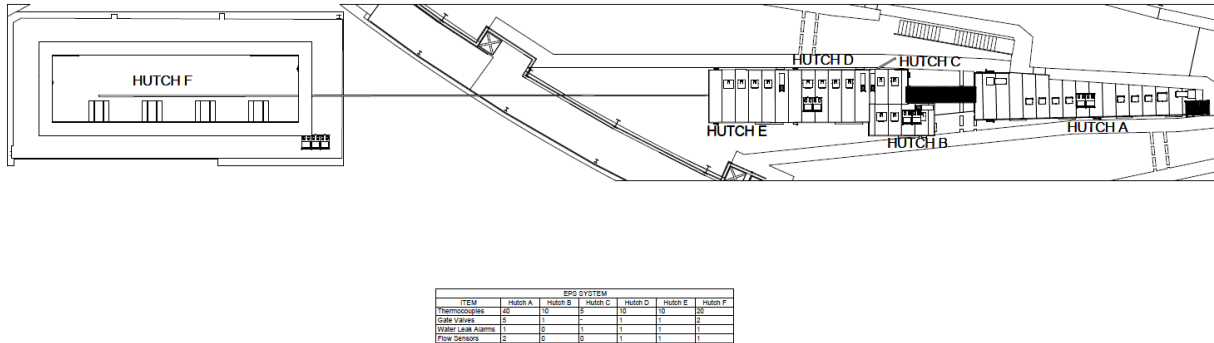


**Fig 5.17:** Markup showing locations of EPS components.

## 5.8 Personnel Protection System

HEX will produce intense hard x-rays with multiple stations along the beamline. These stations are expected to work in parallel or sequentially. The PPS is an engineered system that provides a means to ensure that personnel is not exposed to the radiation in the beamline. At NSLS-II, the role of the PPS is specifically to protect personnel from radiation that is present only when there are stored electrons in the storage ring. The PPS will be designed to monitor the various devices installed in the beamline for personnel safety and to provide emergency shutdown in case of any breach of the interlock. The PPS system, along with the required shielding in the beamlines, will be designed to provide complete personnel safety during routine operation of the facility and provide protection during abnormal conditions. The following figure shows a typical system configuration, in this case for an FOE and two experimental stations, although this is designed to be easily configured to the required number of stations and beamline operating modes.

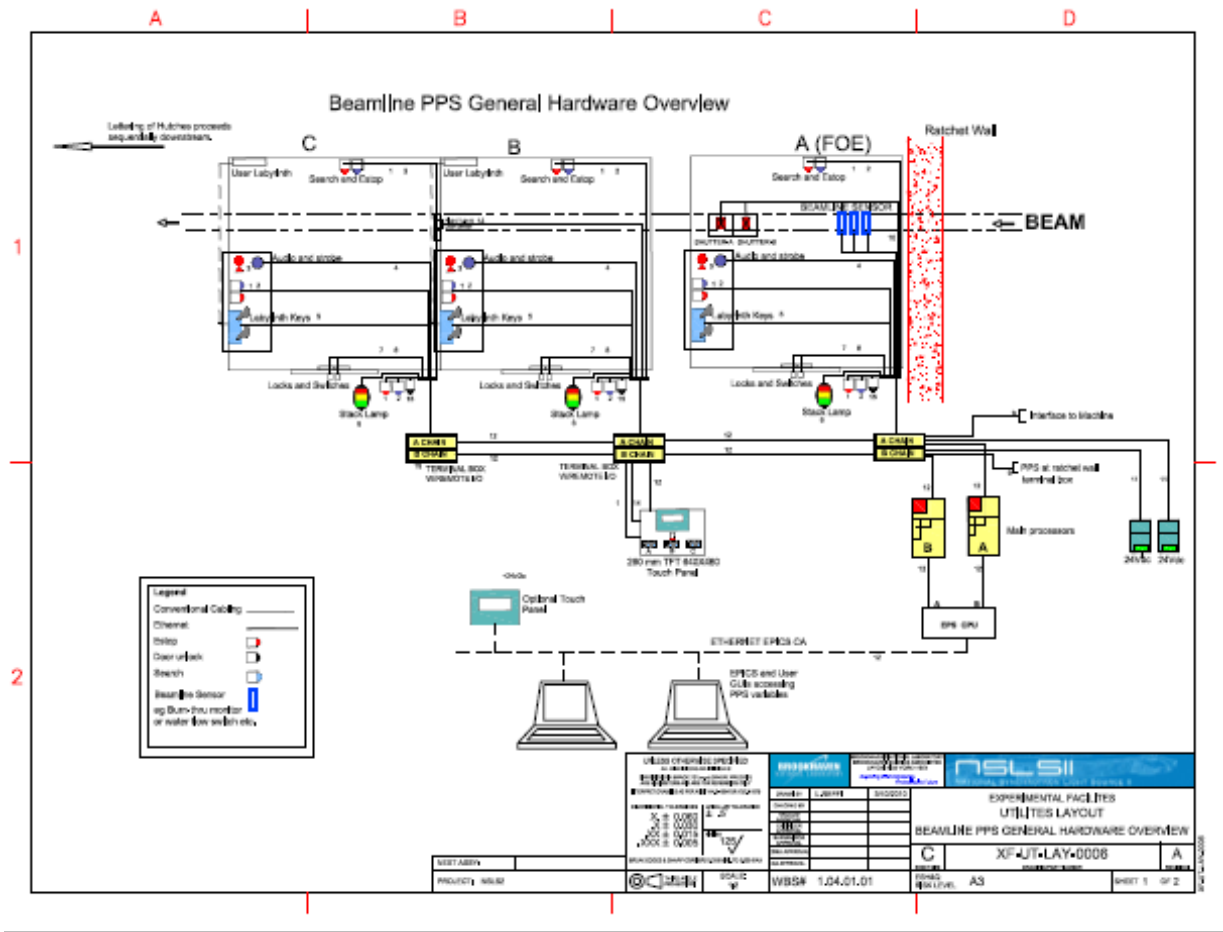


**Figure 5.18** Typical system configuration for an FOE and two experimental stations.

Fig.5.19 shows the locations for the PPS components. The HEX PPS includes a set of redundant sensors and interlocks for the cooling water of the white beam components.

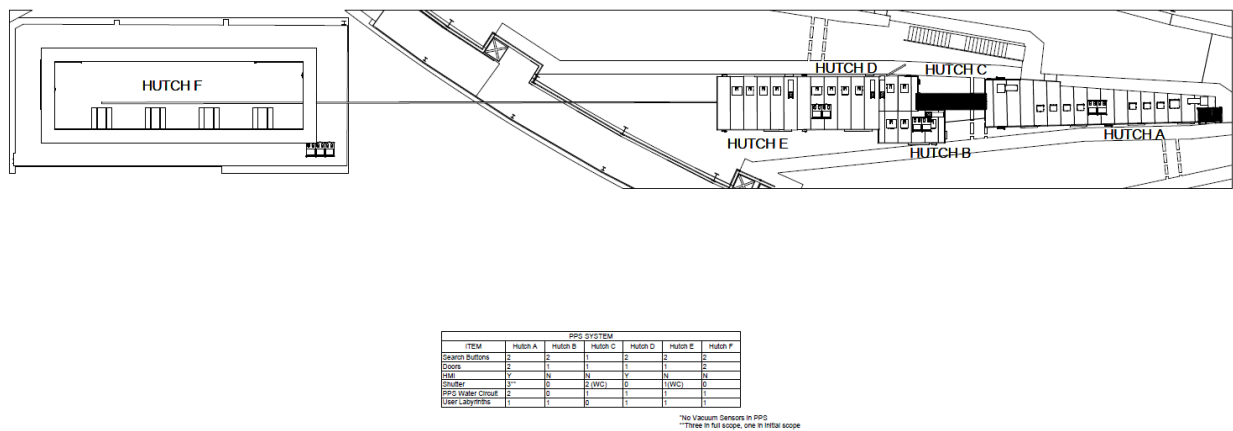


**Fig 5.19:** Markup showing locations of PPS components at HEX.

## 6 MAJOR TECHNICAL RISK ITEMS

The requirements on the optics are achievable today. No new technical advances are required for delivering the proposed capabilities. The EDXD endstation was in use until the NSLS shutdown in September 2014 and is anticipated to be in continuous operation and receive updates at the APS until 2021. We anticipate the following technical risks:

### **Complexity of the beamline**

HEX will be designed to accommodate three independent branches. However, due to funding constraints, only the center branch will be constructed and fitted with endstations in the current scope. The design of the beamline will have to anticipate future addition of two independent beamlines. Thus there is a risk of missing important interfaces. The risk is highlighted by the fact that many of these interfaces will be to hardware which will not be physically fabricated or in place at the completion of HEX. The strategy will be to ensure that the design of all components is completed at the design stage and that the design is feasible and optimized.

### **Impact on Storage Ring**

The superconducting wiggler is expected to have minimal impact on the performance of the storage ring. Preliminary analysis by Weiming Guo shows that the impacts on both emittance and momentum spread are acceptable. This needs to be further verified by accelerator physicists once the detailed design and specification of the wiggler, its location, and front-end design are available.

### **Superconducting Wiggler**

Due to its uniqueness and limited number of suppliers, the purchase or design/manufacture of the superconducting wiggler poses potential technical risk. In the event of problems, a temporary alternative would be to use a permanent magnet wiggler. Such wiggler could be available from the Australian Light Source. The downside is the lower critical energy, however it was used successfully at the imaging beamline IMBL for a few years before an SCW could be purchased.

### **Unique front-end will accommodate a large horizontal fan**

The HEX front-end needs to accommodate a large horizontal fan of about 7 mrad. We realized the potential technical risk about a year ago in 2016 and asked the front-end group headed by Sushil Sharma to study the technical risk. Over the past year, the front-end group iterated with the HEX team to come up with a wiggler specification (SCW70) and a three beam-lets design that is acceptable for front-end design and requires minimum modification of standard front-end design. This technical risk will be mitigated early on at the HEX project by performing detailed front-end design.

### **Unique New Design of Fixed Masks**

13-April-2018



The fixed masks will use a new design as described in Sec.3.2. This new design has never been experimentally tested. We will monitor the performance of the fixed mask at the SST beamline, which uses the same design, when the beamline is expected to be operational in 2018.

### **Heat load**

The heat-load for the diamond windows, filters and monochromator crystal is high due to the high power density and large horizontal fan of the white beam. The associated risks include deformation or breakage resulting from the applied heat load on the various components.

### **White Beam Transport Tube through Experimental Station D**

A preliminary study by NSLS-II radiation physicist PK Job shows that shielding the transport pipe through the experimental station D with about 10 mm of lead is adequate for allowing personnel access to station D while the center branch is taking beam. If a new radiation study reveals that much thicker lead is required, the transport tube through the experimental station D poses a technical risk of reducing the sample space for the white-beam station. We will mitigate this risk by commissioning the radiation shielding study, especially for the transport tube, early on in the HEX design stage.

### **Unique (to NSLS-II) White-beam Shutter**

The standard NSLS-II safety shutter is designed for monochromatic or pink beam, and does not provide adequate shielding for Bremsstrahlung radiation. The white-beam for the center-branch and side branch both require a non-standard shutter that is compatible with white-beam. We plan to adapt the front-end photon and safety shutter combination for this purpose.

### **Relocation and Re-use of Endstations from APS 6-BM**

If the budget does not allow for purchasing new endstation equipment for the EDXD system, some components will need to be transferred from the EDXD system currently operational at the APS 6-BM beamline. There is a possibility of damage during equipment transfer of the endstations. The transferred endstations may not be compatible with NSLS-II standards in terms of safety, regulations, and software integration. When the EDXD equipment was transferred to APS in early 2015, the motor connectors were converted to the APS standard. These motor connectors will need to be converted to the new NSLS-II standard.

It would be good to look into any desired upgrades of the re-used endstation hardware during the implementation phase, not later. Such upgrades may be relatively inexpensive and pay back immediately with improved performance and/or added longevity. Also, there is a risk that some aspects of the “old” endstation hardware are not compatible with NSLS-II standards and/or with the HEX design.

## **7. SAFETY**

In addition to safety precautions related to the synchrotron source, the HEX beamline will provide proper emergency egress routes and capability to handle samples and associated chemicals and gases appropriately. The experimental station in the satellite building is located in a relatively enclosed area, thus care must be taken to guarantee adequate egress routes in case of emergency. Two egress routes will be provided.

The PDR document will include a detailed safety section.

## 8. REFERENCES

- [1] “GE Uses DOE Advanced Light Sources to Develop Revolutionary Battery Technology” DOE Stories of Discovery & Innovation <https://science.energy.gov/news/featured-articles/2011/127017/>
- [2] Diamond Light Source, Joint Engineering, Environmental and Processing (JEEP) I12 Beamline <http://www.diamond.ac.uk/Home/Beamlines/I12.html>
- [3] HEX May 2011 Workshop JEERP-Diamond Presentation, M. Drakopoulos “The New High Energy Beamline for Engineering, Material Science and Processing at the Diamond Light Source”
- [4] See <http://www.esrf.eu/home/UsersAndScience/Experiments/StructMaterials/ID15A.html>
- [5] HEX May 2011 Workshop ESRF Presentation link [http://www.physics.rutgers.edu/~croft/BDP11/HEX-WS-presentations/NSLS2\\_workshop\\_Buslaps.pdf](http://www.physics.rutgers.edu/~croft/BDP11/HEX-WS-presentations/NSLS2_workshop_Buslaps.pdf)
- [6] ESRF ID-19. <http://www.esrf.eu/home/UsersAndScience/Experiments/StructMaterials/ID19.html>
- [7] HASYLAB PETRA-III High Energy Materials Science Beamline [http://photon-science.desy.de/facilities/petra\\_iii/beamlines/p07\\_high\\_energy\\_materials\\_science/index\\_eng.html](http://photon-science.desy.de/facilities/petra_iii/beamlines/p07_high_energy_materials_science/index_eng.html)
- [9] see J. Almer “High Energy X-ray Studies of Engineering Materials at the APS 1-ID-C-E Beamline” presented at HEX Workshop [http://www.physics.rutgers.edu/~croft/BDP11/HEX-WS-presentations/Almer\\_NSLs\\_Workshop\\_May11.pdf](http://www.physics.rutgers.edu/~croft/BDP11/HEX-WS-presentations/Almer_NSLs_Workshop_May11.pdf)
- [10] see M. Rivers “Geoscience Applications of High-Energy Synchrotron Computed Microtomography” HEX May 2011 Workshop [http://www.physics.rutgers.edu/~croft/BDP11/HEX-WS-presentations/Rivers\\_HighEnergyWorkshop.pdf](http://www.physics.rutgers.edu/~croft/BDP11/HEX-WS-presentations/Rivers_HighEnergyWorkshop.pdf)
- [11] HEX May 2011 Workshop Program link <http://www.bnl.gov/nsls2/workshops/BeamlineDevelopment/HEX.asp>
- [12] HEX May 2011 Workshop Presentations link <http://www.physics.rutgers.edu/~croft/BDP11/HEX-WS-presentations/>
- [13] see “3.D. Engineering Diffraction” by J. Ilavsky, G. Long, M. Miller, C. Noyan, P. Peterson, B. Toby in the Computational Scattering Science 2010 Workshop Report <http://www.physics.rutgers.edu/~croft/BDP/Computational%20Scattering%20Science%202010.pdf>
- [14] Department of Energy’s Basic Energy Sciences’ report on Basic Research Needs for Electrical Energy Storage. [https://science.energy.gov/~media/bes/pdf/reports/files/ees\\_rpt\\_print.pdf](https://science.energy.gov/~media/bes/pdf/reports/files/ees_rpt_print.pdf)
- [15] J. Rijssenbeek, Y. Gao, Z. Zhong, N. Jisrawi, I. Ignatov, M. Croft (extended abstract) “In-situ Spatial and Temporal Studies of Electrochemistry in Advanced High Temperature Batteries Under Operating Conditions” Micro. and Microanalysis, 15 (Suppl. 2) , pp 1394-1395 (2009)
- [16] J. Rijssenbeek, Y. Gao, Z. Zhong, M. Croft, N. Jisrawi, I. Ignatov, T. Tsakalakos, “In situ x-ray diffraction of prototype sodium metal halide cells: time and space electrochemical profiling” Journal of Power Sources, 196, 2332-2339 (2011)
- [17] Harry KJ, Parkinson DY, Balsara NP. Failure Analysis of Batteries Using Synchrotron-based Hard X-ray Microtomography. *Journal of Visualized Experiments : JoVE*. 2015;(102):53021. doi:10.3791/53021.
- [18] “Three-dimensional characterization of electrodeposited lithium microstructures using

synchrotron X-ray phase contrast imaging”, D. Eastwood et al, Chem. Commun. 2015 (51) 266. DOI: 101039/c4cc03187c.

- [19] “Application of Synchrotron EDXD Strain Profiling in Shot Peened Materials”, I. Zakharchenko, Y. Gulak, Z. Zhong, M. Croft, and T. Tsakalakos, *Advances in X-ray Analysis*, Vol. 46, 338-345 (2003)
- [20] “Strain Profiling of Fatigue Crack Overload Effects Using Energy Dispersive X-Ray Diffraction” M. Croft, Z. Zhong, N. Jisrawi, I. Zakharchenko, R.L. Holtz, Y. Gulak, J. Skaritka, T. Fast, K. Sadananda, M. Lakshmipathy, and T. Tsakalakos. *Int. J. Fatigue* 27, 1409 (2005)
- [21] “Fatigue history and in-situ loading studies of the overload effect using high resolution x-ray strain profiling”, M. Croft, N. M. Jisrawi, Z. Zhong, R. Holtz, K. Sadananda, J. Skaritka, and T. Tsakalakos, *International Journal of Fatigue* 29 (issues 9-11) 1726-1736 (2007)
- [22] “Stress Gradient Induced Strain Localization in Metals: High Resolution Strain Cross Sectioning via Synchrotron X-Ray Diffraction” M. Croft, N. Jisrawi, Z. Zhong, R. Holtz, M. Shepard, M. Lakshmipathy, K. Sadananda, J. Skaritka, V. Sukla, R. Sadangi and T. Tsakalakos, *Engineering Materials and Technology*, 130, 021005 (2008)
- [23] “Mapping and load response of overload strain fields: synchrotron x-ray measurements”, M. Croft, V. Shukla, N. M. Jisrawi, Z. Zhong, R. K. Sadangi, R. L. Holtz, P. Pao, K. Horvath, K. Sadananda, A. Ignatov, J. Skaritka, and T. Tsakalakos, *Int J. of Fatigue* 31, 1669-1677 (2009)
- [24] Korsunsky, A., Collins, S., Owen, R., Daymond, M., Achtioui, S., and James, K., 2002, “Fast Residual Stress Mapping Using Energy-Dispersive Synchrotron X-Ray Diffraction on Station 16.3 at the SRS,” *J. Synchrotron Radiat.*, 9, pp. 77–81.
- [25] James, M., Hattingh, D., Hughes, D., Wei, L.-W., Patterson, E., Quinta Da Fonseca, J., 2004, “Synchrotron Diffraction Investigation of the Distribution and Influence of Residual Stresses in Fatigue,” *Fatigue Fract. Eng. Mater. Struct.*, 27, pp. 609–622.
- [26] Steuwer, A., Santistebban, J., Turski, M., Withers, P., and Buslap, T., 2004, “High-Resolution Strain Mapping in Bulk Samples Using Full-Profile Analysis of Energy-Dispersive Synchrotron X-Ray Diffraction Data,” *J. Appl. Crystallogr.*, 37, pp. 883–889.
- [27] Steuwer, A., Santisteban, J., Turski, M., Withers, P., and Buslaps, T., 2005, “High-Resolution Strain Mapping in Bulk Samples Using Full-Profile Analysis of Energy Dispersive Synchrotron X-Ray Diffraction Data,” *Nucl. Instrum. Methods Phys. Res. B*, 238\_1–4\_, pp. 200–204.
- [28] “The evolution of crack-tip stresses during a fatigue overload event” A. Steuwer, M. Rahman, A. Shterenlikht, M.E. Fitzpatrick, L. Edwards, *Acta Materialia* 58 (2010) 4039–4052
- [29] Jones, J., Motahari, S., Varlioglu, M., Lienert, U., Bernier, J., Hoffman, M., and Ustundag, E., 2007, “Crack Tip Process Zone Domain Switching in a Soft Lead Zirconate Titanate Ceramic,” *Acta Mater.*, 55, pp. 5538–5548.
- [30] Martins, R., Lienert, U., Margulies, L., and Pyzalla, A., 2005, “Determination of the Radial Crystallite Microstrain Distribution Within an AlMg<sub>3</sub> Torsion Sample Using Monochromatic Synchrotron Radiation,” *Mater. Sci. Eng., A*, 402, pp. 278–287.
- [31] “NSLS-II strategic planning workshop”. <https://www.bnl.gov/nsls2spw/>
- [32] “High-energy x-ray micro-mapping of materials: engineering applications”. M. Croft, V. Shukla, R. K. Sadangi, T. Tsakalakos.
- [33] “Evaluation of the overload effect on fatigue crack growth with the help of synchrotron XRD strain mapping” J. Belnoue, T-S Jun, F. Hofmann, B. Abbey, A. M.. Korsunsky, *Engineering*

Fracture Mechanics 77 (2010) 3216–3226

## 9. REFERENCE DOCUMENTS

Hyperlinks only work within the BNL firewall. Copies of documents are available on request.

Reference Document	Document number (Sharepoint)
<a href="#">Project Management Plan</a>	HEX00
<a href="#">NYSERDA Contract</a>	HEX01
RSI document for satellite building	HEX05
<a href="#">RSI document for SCW/FE</a>	HEX06
Monthly P6 Poster	HEX11
<a href="#">HEX Beamline Development Proposal (BDP)</a>	HEX26
<a href="#">Link to the HEX Scientific Kick-Off Meeting</a>	N/A